

Institut für Festkörperphysik

FRIEDRICH-SCHILLER-UNIVERSITÄT JENA



 <p>Tieftemperaturphysik Prof. Dr. P. Seidel apl. Prof. Dr. F. Schmidl Dr. R. Nawrodt</p>	 <p>Oberflächenphysik Prof. Dr. T. Fritz Dr. R. Forker Dr. B. Schröter</p>
 <p>Physik nanoskaliger Festkörper Prof. Dr. C. Ronning</p>	 <p>Ionenstrahlphysik apl. Prof. Dr. E. Wendler</p>
 <p>Photovoltaik Prof. Dr. C. Ronning PD Dr. C.S. Schnoher Dr. U. Reislöhner</p>	 <p>Laborastrophysik und Clusterphysik Dr. C. Jäger</p>

Annual Report 2016

Institut für Festkörperphysik

Friedrich-Schiller-Universität Jena

Annual Report 2016



Editor: Prof. Dr. Carsten Ronning & Cindy Büchner

**Institut für Festkörperphysik
Friedrich-Schiller-Universität Jena
Helmholtzweg 3/5
D-07743 JENA**

home page: <http://www.ifk.uni-jena.de/>

Prof. Dr. Torsten Fritz Tel.: +49 (0) 3641 / 947400, 947411
 Fax: +49 (0) 3641 / 947412
 e-mail: torsten.fritz@uni-jena.de
 home page: <http://www.organics.uni-jena.de>

Prof. Dr. Carsten Ronning Tel.: +49 (0) 3641 / 947300, 947301
(director) Fax: +49 (0) 3641 / 947302
 e-mail: carsten.ronning@uni-jena.de
 home page: <http://www.nano.uni-jena.de>
 <http://www.photovoltaik.uni-jena.de>

Prof. Dr. Paul Seidel Tel.: +49 (0) 3641 / 947410, 947411
 Fax: +49 (0) 3641 / 947412
 e-mail: paul.seidel@uni-jena.de
 home page: <http://www.tieftemperaturphysik.uni-jena.de/>

apl. Prof. Dr. Frank Schmidl Tel.: +49 (0) 3641 / 947429, 947411
 Fax: +49 (0) 3641 / 947412
 e-mail: frank.schmidl@uni-jena.de
 home page: <http://www.tieftemperaturphysik.uni-jena.de/>

apl. Prof. Dr. Elke Wendler Tel.: +49 (0) 3641 / 947333
 Fax: +49 (0) 3641 / 947302
 e-mail: elke.wendler@uni-jena.de
 home page: <http://www.ionenstrahlphysik.uni-jena.de/>

Dr. Cornelia Jäger Tel.: +49 (0) 3641 / 947354
 Fax: +49 (0) 3641 / 947308
 e-mail: cornelia.jaeger@uni-jena.de
 home page: <http://www.astrolab.uni-jena.de/>

Preface

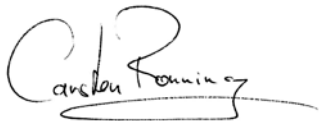
I am pleased to introduce this Annual Report, because 2016 was one of the most successful years of the Institute of Solid State Physics (IFK) at the Friedrich-Schiller-University Jena. Most remarkable is the fact that next to many finished Bachelor and Master theses in the past year, in total ten persons out of the IFK received their PhD degrees, and on top, Dr. Claudia Schnohr finished her Habilitation in 2016. This strongly underlines the high efficiency and performance of our small institute. Furthermore, a significant amount of these highly educated persons left our institute and accepted new challenging jobs in industry and academia around the world. We are very proud on our alumni, which spent one of the most important time spans of their career with us, and now hold important positions and functions in our society.

We consider the education of young people at all levels as our most important duty and task, but we are also extremely proud on our research output produced in 2016. Even though our human recourses are continuously decreasing in the past years, the quality and quantity of scientific achievements is rather high and still increasing. Some outstanding examples are documented in the following pages of this report.

Furthermore, we like to take this annual report as an opportunity to thank a lot of people, funding agencies, and organizations for their manifold support for our research. We also like to thank all our colleagues at other universities and institutes all over the world, which were or are still collaborating with us, but where the collaborative work has not been presented in the research articles of this report.

Last but not least, we are very grateful for the work of our very motivated secretaries, technicians, and the people in the mechanical and electrical workshops. All of them have contributed to our research in an outstanding way and, thus, to this report.

Let's altogether keep up the excellent work in 2017 and beyond!

A handwritten signature in black ink, appearing to read 'Carsten Ronning', with a stylized flourish underneath.

Prof. Dr. Carsten Ronning

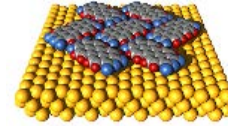
Content

1. Scientific Groups of the Institute (Portraits)	11
1.1 Applied Physics / Solid State Physics [Prof. Fritz]	12
1.2 Experimental Physics / Solid State Physics [Prof. Ronning]	13
1.3 Low Temperature Physics [Prof. Seidel]	14
1.4 Ion Beam Physics [Prof. Wendler]	15
1.4 Laboratory Astrophysics / Cluster Physics [Dr. Jäger]	16
2. Current Research Projects	17
2.1 Research Areas and Important Results	17
2.2 Third Party Grants	20
3. Publications, Invited Talks, and Theses	22
3.1 Publications in Scientific Journals	22
3.2 Invited Talks at Conferences and Colloquia	27
3.3 Theses	28
4. Cooperations, Visiting Scientists, and Colloquia at the IFK	31
4.1 Cooperations	31
4.2 Visiting Scientists	32
4.3 Colloquia at the Institute of Solid State Physics	33
5. Personnel	34
6. Technical Reports and Equipment	36
6.1 Operation of the Ion-Accelerator JULIA and the Ion-Implanter ROMEO	36
6.2 Cryogenic Services (TTS)	38
6.3 Equipment	39
7. Scientific Reports	42
High temperature limit of CdS semiconductor nanowire lasers	42
Inherently flat metasurfaces enabled by spatially selective ion irradiation	44
Discrepancy between integral and local composition in off-stoichiometric Cu ₂ ZnSnSe ₄ kesterites: A pitfall for classification	46
Bond strength inversion in (In,Ga)As	48
Secondary phases in Cu ₂ ZnSnSe ₄ studied by X-ray absorption spectroscopy	50
Ultra-low temperature chemistry of (³ C ₀) atoms	52
Cosmic dust analogues – Simultaneous formation of silicate and carbon condensates at cryogenic temperatures	54

Investigation of LiNbO_3 by combined RBS and NRA in channelling configuration	56
Ion beam modification of single crystalline BiVO_4	58
The lattice expansion and anisotropic refractive index of KTiOPO_4 waveguides formed by ion implantation	60
Insight into the unit cell: Structure of picene thin films on $\text{Ag}(100)$ revealed with complementary surface science methods	62
Naphthalene's six shades on graphite: A surprisingly rich polymorphism	64
Estimation of silicon suspension thermal noise in thermal non-equilibrium	66
Precise optical bulk and surface absorption measurements in high purity silicon	68
Angular dependence of $\text{Nd}(\text{O},\text{F})\text{FeAs}$ thin film grain boundary junctions	70
Modes of collective excitations in two inductively coupled long Josephson junctions	72
LC-shunted HTS Josephson junctions	74
Investigation of flux-trapping in superconducting thin-film structures during cool-down	76
Single artificial atom lasing by a dressed flux qubit	78
Verifiable quantum superpositions in superconducting interconnects	80
Induction measurements at the Lambda point	82
Precision induction measurements of flux concentrators	84
Development of an applicable test facility for lowest permeation values and investigation of samples, which are suitable for the non-magnetic cryostats	86
Developing processes and devices for abrasive blasting with cryogenic water ice	88
Comparative analysis of current transport on small angle grain boundaries on thin YBCO films using x-ray microscopy and magneto-optical imaging	90

1. Scientific Groups of the Institute (Portraits)

Applied Physics / Solid State Physics



Prof. Dr. Torsten Fritz

- Preparation of highly ordered thin films of organic molecules by UHV-deposition (OMBE)
- Chemical vapor deposition and characterization of carbon nanotubes
- Epitaxial graphene
- Organic-organic heteroepitaxy
- K-doped organic semiconductors and superconductors
- *In situ* optical spectroscopy (DRS and PL) on ultrathin molecular layers
- Analyses of surfaces, layers and nanostructures using AES, UPS, ARUPS, XPS, LEED, RHEED, XPD, STM, AFM, and SEM

The group *Applied Physics / Solid State Physics* at the Institute of Solid State Physics is engaged in the research on nanostructures, solid surfaces and thin films of both organic and inorganic semiconductor materials.

Our main research interest lays in the discovery of structure-property-relations of structurally well defined ultrathin epitaxial layers, organic quantum wells, K-doped organic super conductors, and carbon nanotubes. The main target of our research is the development of basic principles for the use of nano materials in prospective devices.

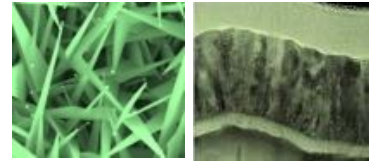
For the analyses of the chemical composition and bonding at surfaces and in thin films, we use surface analysis methods like photoelectron spectroscopy with X-rays (XPS) and with ultraviolet photons (UPS), the latter with angle-resolved measurements (ARUPS). The crystalline structure of the films is determined by us using distortion-corrected electron diffraction (LEED). Scanning tunneling microscopy (STM) and atomic force microscopy (AFM), at temperatures down to 1.1 K, are used for high-resolution imaging of nanostructures and surfaces. Electronic states are accessible to us globally via UPS, ARUPS and locally via scanning tunneling spectroscopy (STS).

Our *in situ* optical spectroscopy, namely differential reflectance spectroscopy (DRS), is used to study organic (sub-)monolayers and heterostructures in terms of absorption spectroscopy to analyze the optical interaction between either the molecules itself, organic adsorbates and inorganic substrates, or molecules and dopants.

Our *in situ* optical spectroscopy, namely differential reflectance spectroscopy (DRS) is used to study organic (sub-)monolayers and heterostructures in terms of absorption spectroscopy to analyse the optical interaction between either the molecules itself, organic adsorbates and inorganic substrates, or molecules and dopants.

Experimental Physics / Solid State Physics

Prof. Dr. Carsten Ronning



- Synthesis, doping and functionization of semiconductor nanowires
- Photovoltaics
- Atomic structure and band-gap of complex semiconductors
- Modification and functionaization of phase change materials
- Growth and functionalization of diamond-like materials
- Semiconductor physics: doping using ion beams
- Ion beam synthesis of nanostructures

Recent work of the research group *Experimental Physics / Solid State Physics* in the field of semiconductor nanowires focuses both on the growth of desired nanostructures as well as on the modification of semiconductor nanowires using ion beams for the use as photonic and electronic devices. This includes the realization of light-emitting diodes, single photon emitters, sensors for bio and chemical applications, and the observation of laser oscillations within single nanowires. Another scientific area of the group is the investigation and manipulation of phase change materials and devices using ion beams in order to create novel metamaterials and meta-surfaces. Furthermore, the group works on the basic mechanism of ion–nanostructure–interactions: here, the different accelerator systems are used for detailed investigations of the sputter yield of nanoparticles and nanowires, as well as their dynamic changes on morphology and stoichiometry upon high ion fluence irradiations.

The research on photovoltaics is mainly directed to the synthesis and analysis of $\text{Cu}(\text{In,Ga})(\text{Se,S})_2$ based thin film solar cells (CIGS). The research aims at a better understanding of the materials science of the CIGS chalcopyrite semiconductors and the improvement of existing cell concepts. To this end, a complete baseline on a form factor of $10 \times 10 \text{ cm}^2$ is available at the institute. Most important, we developed a high expertise in a comprehensive characterization of the structural, electrical and optical properties of CIGS solar cells. Besides standard tools, such as XRD, PL, CL, IV, we also use sophisticated synchrotron based characterization methods (EXAFS, XRF) or advanced electrical instruments (TAS, DLTS, etc.).

Low Temperature Physics

Prof. Dr. Paul Seidel



- Superconductivity within thin layers and layer systems
- Josephson effects, proximity effect, and tunnel effects in superconducting devices and heterojunctions
- DC-SQUID's and their application in measurements, e.g. CCC, MRX
- cryogenic measurements of mechanical quality factor and optical properties
- Dynamics of superconducting intrinsic Josephson arrays
- cryogenic engineering (cryocoolers, cryogenic storage, cryostates)

The *Low Temperature Physics* group works on the following fields:

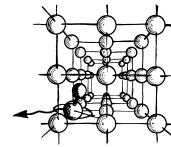
- preparation, characterization, modelling and application of Josephson junctions and SQUIDs (high precision and magneto-relaxation measurements with LTS SQUIDs, development of HTS SQUIDs, intrinsic Josephson junctions and Josephson junctions with iron based superconductors)
- low temperature physics and cryogenic engineering (development of new kinds of pulse tube cryocoolers, low loss cryostats and cryogenic storage, cryogenic current comparator CCC for particle accelerator beam analysis)
- experimental work on cryogenic measurements of the Q-factor and of optical properties of components for future gravitational wave detectors like the Einstein Telescope
- thin film technologies for insulators and other materials
- alternative preparation and properties of crystalline gold nanoclusters

The research is carried out in cooperation with other research groups in Thuringia (TU Ilmenau, Leibniz Institute IPHT Jena, SUPRACON Jena, Innovent e.V. Jena, Helmholtz Institute Jena). Within common activities the group works together with the Gesellschaft für Schwerionenforschung (GSI) Darmstadt, DESY Hamburg, MPI Heidelberg, IFW Dresden and the DLR Bremen.

Several research activities exist with industrial partners e.g. with the TransMIT center for adaptive cryotechniques Gießen. A long tradition of cooperation with the Universities of Moscow and Dubna (Russia), Bratislava (Slovak Republic), Kharkov and Donetsk (Ukraine), Glasgow (U.K.), Poznan (Poland), Padua, Torino and Florence (Italy), and the Universities of Osaka, Tokyo and Nagoya (Japan) is also remarkable.

Ion Beam Physics

Prof. Dr. Elke Wendler



- Modification of solids by ion implantation and subsequent processes
- Ion beam analysis (RBS, PIXE, ERD, NRA)
- Ion beam synthesis of buried nanostructures
- Investigation of damage formation and amorphisation of covalent-ionic materials

The *Ion Beam Physics* group deals with modification of solids and synthesis of buried nanostructures using ion beams and combined secondary processes. The studies cover fundamental processes of ion-beam induced structural modification in semiconductors and insulators being relevant for future electronic, optoelectronic and photonic device technologies.

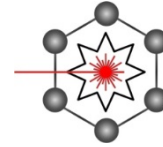
Currently, there is an increasing interest in oxidic semiconductor materials. They are important for application in photovoltaic, electronic and optical devices because of their wide band gap and high transparency in the visible region of light. As ion implantation is a common technology in device fabrication, radiation resistance and damage formation in this group of materials became an important field of our work.

Classical group IV and III-V semiconductors are in the focus of our studies, too. Combining different ion beam analysis techniques with in-situ curvature measurements and ex-situ XRD reveals a deeper inside in type and concentration of defects produced by ion implantation. The damage formation is related to the primary energies deposited in electronic and nuclear processes, which finally will allow to predict damage to be expected for given irradiation conditions. This knowledge is prerequisite for modelling thermal effects and dopand behaviour.

Our research on new materials and new research topics is connected with a continuous development of ion beam analysis. This comprises both the experimental technique and the extended and combined use of the various ion beam analysis methods.

Laboratory Astrophysics / Cluster Physics

Dr. Cornelia Jäger



- Electronic spectroscopy of neutral and ionized polycyclic aromatic hydrocarbons (PAHs) in supersonic jets and cryogenic matrices
- Study of astrochemically relevant reactions in liquid helium nanodroplets
- Condensation and growth of cosmic dust at low temperature and pressure
- Gas-phase condensation processes of cosmic dust nanoparticles at high temperatures in circumstellar environments
- Study of chemical and structural processing of cosmic dust grains and astrophysically relevant molecules by UV photons and ion bombardment
- Chemical reactions and processing at the interface between dust and molecular ices

The *Laboratory Astrophysics and Cluster Physics Group* at the Institute of Solid State Physics results from a cooperation between the Max Planck Institute for Astronomy, Heidelberg, and the Friedrich Schiller University, Jena. Inaugurated in February 2003, it is now conducted by Prof. Dr. Thomas Henning and Dr. Cornelia Jäger.

The research of our group is devoted to fundamental astrophysical questions that can be answered by laboratory experiments, with particular emphasis on spectroscopy. The electromagnetic radiation reaching us from stellar objects is modified in a characteristic manner by interstellar molecules and dust particles. Many of these “fingerprints” are still far from being understood. In order to determine the species causing the modification of the electromagnetic signals detected by telescopes and satellites, and to understand global cosmic processes, comprehensive laboratory studies are urgently needed.

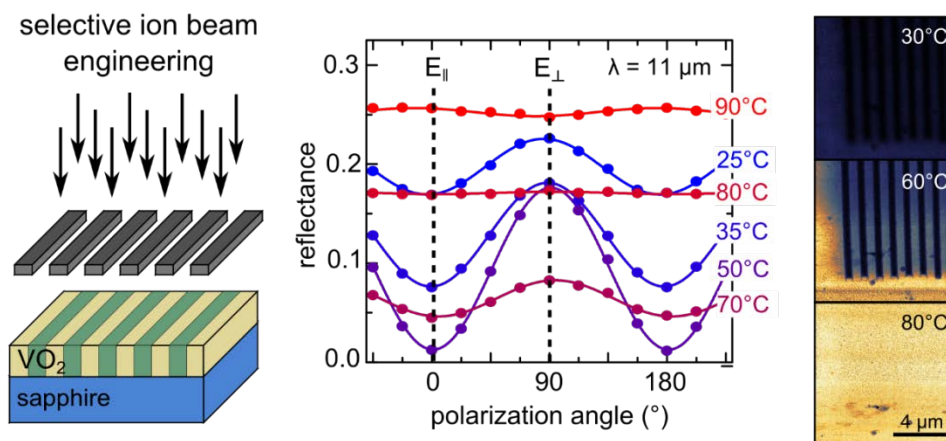
In our laboratory, we study the condensation, processing, and spectral properties of carbonaceous and siliceous dust grains and astrophysically relevant molecules that may play a role as progenitors of grain formation. Laboratory astrophysics is an interdisciplinary field whose research profits from sophisticated experimental facilities. We are able to simulate astrophysically relevant processes such as gas-phase condensation of grains and molecules by laser-induced pyrolysis of hydrocarbons or laser ablation of solids in the laboratory. Interesting molecules, clusters, and nanoparticles are prepared in vacuum chambers under conditions coming close to those in interstellar or circumstellar environments (low pressures and definite temperature ranges from around 10 K up to more than 2000 K). Sophisticated analytical tools comprising optical and IR spectroscopy, mass spectrometry, chromatography, and electron microscopy help us to characterise the composition and structure of the laboratory analogs of dust and complex molecules.

2. Current Research Projects

2.1 Important Results

Important results of the research group of **Prof. Dr. Carsten Ronning** obtained in 2016 included:

- Realization of active optical metasurfaces based on defect-engineered phase-transition materials
- Observation of dielectrically confined excitons in ultrathin GaN nanowires up to room temperature
- Shape manipulation of ion irradiated Ag nanoparticles embedded in lithium niobate
- Shaping and compositional modification of zinc oxide nanowires under energetic manganese ion irradiation
- Mode switching and filtering in nanowire lasers
- Synthesis, morphological and electro-optical characterizations of metal/semiconductor nanowire heterostructures

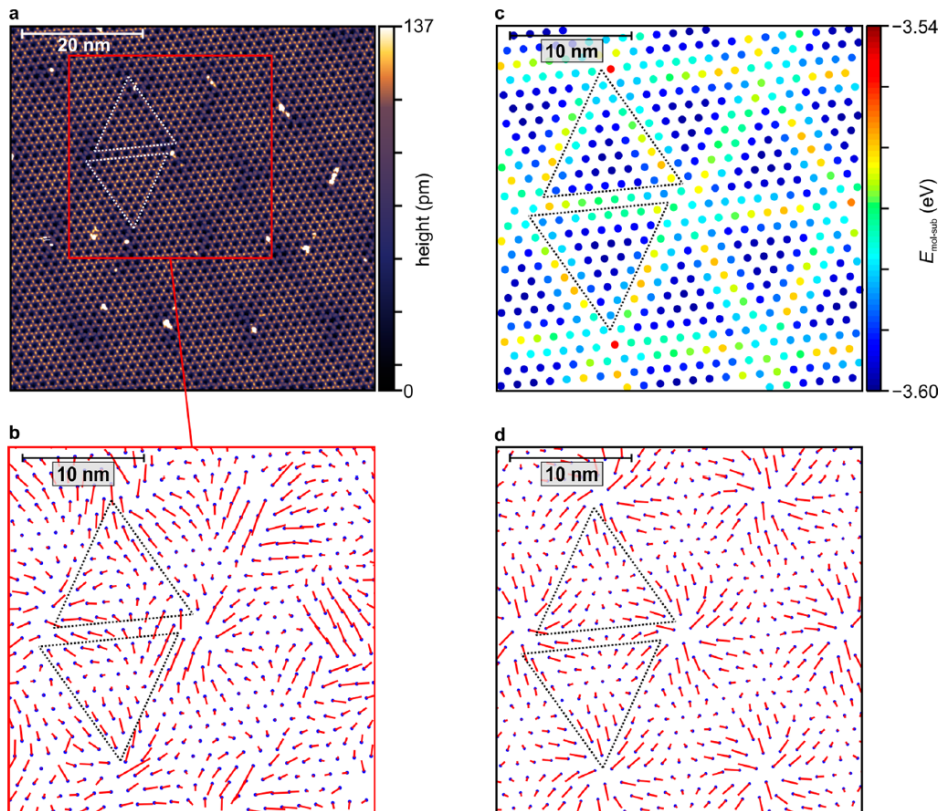


Active optical metasurfaces based on defect-engineered phase-transition materials. Active, widely tunable optical materials have enabled rapid advances in photonics and optoelectronics, especially in the emerging field of meta-devices. We demonstrated that spatially selective defect engineering on the nanometer scale can transform phase-transition materials into optical metasurfaces. Using ion irradiation through nanometer-scale masks, we selectively defect-engineered the insulator-metal transition of vanadium dioxide, a prototypical correlated phase-transition material whose optical properties change dramatically depending on its state. Using this robust technique, we demonstrated several optical metasurfaces, including tunable absorbers with artificially induced phase coexistence and tunable polarizers based on thermally triggered dichroism. Spatially selective nanoscale defect engineering represents a new paradigm for active photonic structures and devices.

Important results of the research of the group of **Prof. Dr. Torsten Fritz** obtained in 2016 included:

- first direct observation of Static Distortion Waves (SDWs) and theoretical elucidation of their stabilizing effect on 2D crystals of polycyclic aromatic hydrocarbons (see below)
- discovery of the self-assembly of tetraphenyldibenzoperiflanthene (DBP) films on Ag(111) in the monolayer regime
- detailed investigation of the beneficial impact a molecular wetting layer (here: PTCDA) has on the structural ordering of SnPc multilayers adsorbed on top

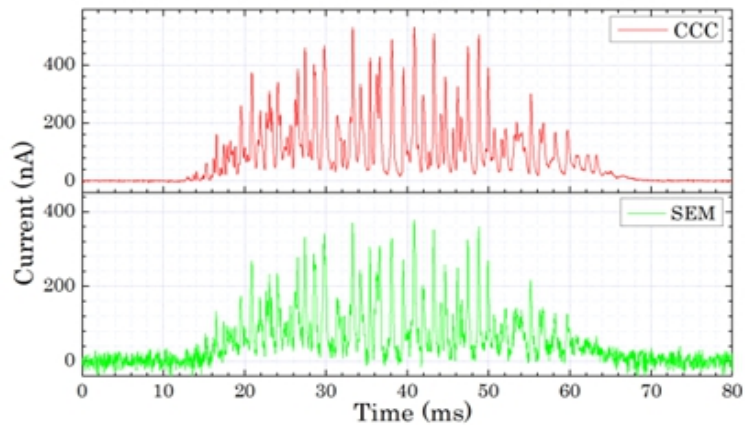
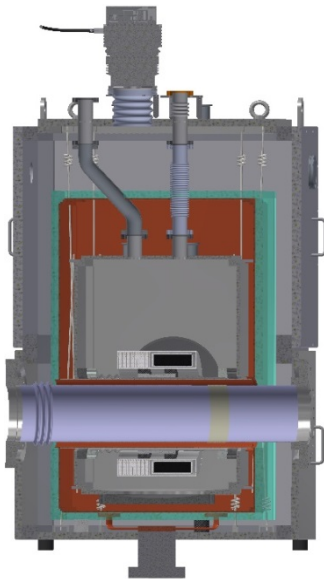
- discovery of a wealth of different phases of naphthalene on graphite (see short report by Sojka *et al.*)
- discovery of the unit cell content of picene on Ag(100) by complementary methods including orbital tomography (photoelectron momentum maps) (see short report by Huempfer *et al.*)



Standing Distortion Waves (SDWs) in a monolayer of the organic molecule HBC on graphite. (a) STM image of 1 ML of HBC on a natural graphite single crystal, at 1.2 K with a sample bias of +3 V and a set point of 2 pA, corrected only for plane tilt, with a color scale adapted to enhance the subtle Moiré pattern, marked by dotted triangles as guides to the eye. (b) Rigid reference lattice (blue dots) corresponding to the low temperature structure and molecular displacements (red lines) determined experimentally from panel a, magnified by a factor of 15. (c) Molecular positions and calculated Moiré pattern in the molecule–substrate energy after relaxation. The non-periodic energy distribution is a direct result of the lack of any lattice match between adsorbate and substrate lattice. (d) Molecular starting positions and calculated displacements, magnified by a factor of 15 as well. Images b–d have the same lateral scale.

Important results of the research group of **Prof. Dr. Paul Seidel** obtained in 2016 included:

- Measurements with a SQUID-based advanced cryogenic current comparator (CCC) to analyze particle beams in accelerators and storage rings
- Different kinds of Josephson junctions with pnictide electrodes in thin film technology as well as using pnictide single crystals
- Modification of structural and superconducting / optical properties of thin high- T_c / STO films with selforganised grown Au-nanoparticles



Advanced CCC for charged particle beam measurements:

Right: Measured spill structure of a slowly extracted Ni²⁶⁺ ion beam from SIS18 accelerator ring at GSI Darmstadt at 600MeV extracted over 120 ms comparing CCC and SEM signal.

Left: Schematic view of the CCC cryostat for CRYRING@ESR (GSI)

[T. Sieber et al., Proceedings of IBIC2016, Barcelona, Spain, ISBN 978-3-95450-177-9]

Important results of the research group of **Prof. Dr. Elke Wendler** obtained in 2016 included:

- Characterization of single crystals and ion implanted single crystals by angular resolved Rutherford backscattering spectrometry (RBS)
- Combination of RBS and Nuclear Reaction Analysis (NRA) for analysis of both Nb and Li sublattice in single crystalline and ion implanted LiNbO₃
- Demonstration of phase transformation of β -Ga₂O₃ to γ -Ga₂O₃ by ion implantation

Important results of the research group of **Dr. Cornelia Jäger** obtained in 2016 included:

- The reformation of cosmic dust at temperatures of about 10 K and very low densities was studied experimentally for complex silicates, carbonaceous dust, and mixed systems. Structural analyses proved the formation of fullerene-like carbon grains and various fullerenes at 10K in carbonaceous materials pointing to a formation pathway via carbon chains.
- The interaction of 10 keV protons with MgFeSiO₄ and Mg₂SiO₄ nanometer-sized grains, two major components of cosmic dust in circumstellar shells, the interstellar medium and planetary systems, causes a selective sputtering of oxygen and the reduction of ferric, ferrous, and Si⁴⁺ ions to Fe⁰ and Si⁰ at temperatures of 10-20 K and the formation of metallic inclusion of iron and Si. This has a strong influence on the spectral properties of the dust in the NIR, FIR and submm range.
- Fullerenes react with C atoms in extremely cold environments. Experiments performed in helium droplets at 0.37 K doped with C₆₀ molecules and C atoms revealed the formation of carbenes of the type C₆₀(C)_n with up to 6 C atoms and of dumbbell C₆₀=C=C₆₀ structures. Density functional theory calculations were performed that elucidated the carbene character of the C₆₀(C)_n species and their structures.

2.2 Third Party Grants

DFG projects

Dotierte aromatische Dünnschichten mit supraleitenden Eigenschaften

(FO 770/2-1)

Time span: 09/14 – 08/17

Research unit FOR1616: Dynamics and Interactions of Semiconductor Nanowires for Optoelectronics (second period of FOR1616)

Time span: 08/15 – 08/18

Projekt P4 of FOR1616: Light-matter interaction in optically doped nanowire LEDs and nano lasers (Ro1198/14-2, 2. Period of FOR1616)

Time span: 08/15 – 08/18

Josephson effects at iron pnictides - phase-sensitive experiments (SE 664/15-2)

Time span: 10/13 – 09/16

Experimental studies of the low-temperature condensation of cosmic dust in the interstellar medium (JA 2107/2-2, second Period of the SPP 1378)

Time span: 10/14 – 09/17

Optical properties and photostability of ice-silicate-carbon mixtures in stellar UV fields (JA 2107/3-1, first period of FOR2285)

Time span: 12/15 – 12/18

Experimental studies on the diamond formation in astrophysical environments (JA 2107/4-1)

Time span: 11/15 – 10/18

Atomic-scale structure of kesterites (SCHN 1283/2-1)

Time span: 03/16 – 02/19

BMBF-, BMU- and BMWi-projects

Verbundvorhaben: Grenzflächen und Defekte – Rechnerunterstützte Optimierung des Wirkungsgrades von CIGS Dünnschichtsolarzellen in der industriellen Umsetzung

Teilvorhaben: Ermittlung von Struktur-Eigenschaftsbeziehungen und ihre Beeinflussung durch Variation der Prozessparameter

Time span: 09/12 – 02/16

Verbundvorhaben: speedCIGS: CIGS-Depositionsgeschwindigkeit und K-Einbau - Rechnerunterstützte Optimierung des CIGS-Depositionsprozesses in der industriellen Umsetzung

Time span: 10/16 – 10/20

In-operando Röntgenanalyse von funktionalen, nanoskaligen Bauelementen (nano@work)

Time span: 07/16 – 06/19

Neuartige Verbundmaterialien u. Fertigungstechnologien für Kryostate zur see- u. luftgestützten Rohstoff- und Umwelterkundung (MAKSEL)

Time span: 09/14 – 09/16

ET R&D – Networking and R&D for the Einstein Telescope (3rd common ASPERA call)

Time span: 03/13 – 02/16

*Entwicklung von Verfahren und Vorrichtung zum Stahlreinigen mittels Wassereis (stream);
Entwicklung der Verfahrensparameter für Strahlmittel und Treibmittel*

Time Span: 06/16 – 5/18

*Staircase structures in the single and coupled Josephson junctions under external radiation
(Heisenberg-Landau Programm)*

Time span: 01/16 – 12/16

*Verbundprojekt 05P2015 - R&D Beschleuniger (CCC): Entwicklung, Sensoroptimierungen
und Tests von Kryogenen Stromkomparatoren zum Einsatz an neuartigen Ionenquellen,
Beschleunigeranlagen und Speicherringen*

Time span 07/15 - 06/18

Anfertigung eines CCC (Optimierung des Gerätes)

Time span: 09/15 – 08/16

*Komplexe Metalloxide als effiziente und stabile Komponenten für die Solare
Wasserstoffherzeugung*

Verbundprojekt „Metalloxid-4-Hydrogen“

Time span: 09/14 – 08/17

Other projects

Virtuelles Institut „MEMRIOX“ (HZDR Dresden-Rossendorf)

Memory Effects in Resistive Ion-beam Modified Oxides

Time span: 10/11 – 09/16

Materials nanostructuring by ion irradiation (DAAD/PPP Serbien)

Time span: 01/16 – 12/17

FP7-PEOPLE-IRSES Scientist Exchange Program „ELiTES“

Time span: 03/12 – 02/17

3. Publications, Invited Talks, and Theses

3.1 Publications in Scientific Journals

Sensitivity of ^{57}Fe Emission Mössbauer Spectroscopy to Ar and C induced defects in ZnO
K. Bharuth-Ram, T.E. Mølholt, G. Langouche, S. Geburt, T. B. Doyle, H. P. Gunnlaugsson, K. Johnston, R. Mantovan, H. Masenda, D. Naidoo, M. Ncube, H. Gislason, S. Ólafsson, C. Ronning, G. Weyer
Hyperfine Interactions **237**, 81 (2016)

Emission Mössbauer Spectroscopy study of fluence dependence of paramagnetic relaxation in Mn/Fe implanted ZnO
H. Masenda, S. Geburt, K. Bharuth-Ram, D. Naidoo, H. P. Gunnlaugsson, K. Johnston, R. Mantovan, T. E. Mølholt, M. Ncube, S. Shayestehaminzadeh, H. P. Gislason, G. Langouche, S. Ólafsson, C. Ronning
Hyperfine Interactions **237**, 40 (2016)

FAST/SPS sintering of nanocrystalline zinc oxide - Part I: Enhanced densification and formation of hydrogen-related defects in presence of adsorbed water
B. Dargatz, J. Gonzalez-Julian, M. Bram, P. Jakes, A. Besmehn, L. Schade, R. Röder, C. Ronning, O. Guillon
Journal of the European Ceramic Society **36**, 1207 (2016)

Observation of dielectrically confined excitons in ultrathin GaN nanowires up to room temperature
J. Zettler, P. Corfdir, C. Hauswald, E. Luna, U. Jahn, T. Flissikowski, E. Schmidt, C. Ronning, A. Trampert, L. Geelhaar, H. Grahn, O. Brandt, S. Fernandez-Garrido
Nano Letters **16**, 973 (2016)

Active optical metasurfaces based on defect-engineered phase-transition materials
J. Rensberg, S. Zhang, Y. Zhou, A.S. McLeod, C. Schwarz, M. Goldflam, M. Liu, J. Kerbusch, R. Nawrodt, S. Ramanathan, D. N. Basov, F. Capasso, C. Ronning, M. Kats
Nano Letters **16**, 1050 (2016)

Non-resonant Raman Spectroscopy of Individual ZnO Nanowires via Au Nanorod Surface Plasmons
A. Pescaglini, E. Secco, A. Martin, D. Cammi, C. Ronning, A. Cantarero, N. Garro, D. Iacopino
Journal of Materials Chemistry C **4**, 1651 (2016)

Shape manipulation of ion irradiated Ag nanoparticles embedded in lithium niobate
S. Wolf, J. Rensberg, A. Johannes, R. Thomae, F. Smit, R. Neveling, M. Moodley, T. Bierschenk, M. Rodriguez, B. Afra, S. Bin Hasan, C. Rockstuhl, M. Ridgway, K. Bharuth-Ram, C. Ronning
Nanotechnology **27**, 145202 (2016)

Shaping and compositional modification of zinc oxide nanowires under energetic manganese ion irradiation
W. Moeller, A. Johannes, C. Ronning
Nanotechnology **27**, 175301 (2016)

CEMS study of defect annealing in Fe implanted AlN

K. Bharuth-Ram, S. Geburt, C. Ronning, H. Masenda, D. Naidoo
Hyperfine Interactions **237**, 32 (2016)

Carrier density driven lasing dynamics in ZnO nanowires

M. Wille, C. Sturm, T. Michalsky, R. Röder, C. Ronning, R. Schmidt-Grund, M. Grundmann
Nanotechnology **27**, 225702 (2016)

Mode switching and filtering in nanowire lasers

R. Röder, T.P.H. Sidiropoulos, R. Buschlinger, M. Riediger, U. Peschel, R.F. Oulton, C. Ronning
Nano Letters **16**, 2878 (2016)

High-level damage saturation below amorphisation in ion implanted β -Ga₂O₃

E. Wendler, E. Treiber, J. Baldauf, S. Wolf, C. Ronning
Nuclear Instruments and Methods **B 379**, 85 (2016)

Synthesis, morphological and electro-optical characterizations of metal/semiconductor nanowire heterostructures

M. Glaser, A. Kitzler, A. Johannes, S. Prucnal, H. Potts, S. Conesa-Boj, L. Filipovic, H. Kosina, W. Skorupa, E. Bertagnolli, C. Ronning, A. Fontcuberta i Morral, A. Lugstein
Nano Letters **16**, 3507 (2016)

Compositional and electrical properties of linear and planar defects in Cu(In,Ga)Se₂ thin films for solar cells - a review

D. Abou-Ras, S.S. Schmidt, N. Schäfer, J. Kavalakkatt, T. Rissom, T. Unold, T. Kirchartz, E. Simsek Sanli, P.A. van Aken, Q.M. Ramasse, H.J. Kleebe, D. Azulay, I. Balberg, O. Millo, O. Cojocar-Mirédin, D. Barragan-Yani, K. Albe, J. Haarstrich, C. Ronning
Physica Status Solidi (RRL) **10**, 363 (2016)

Grain-boundary character distribution and correlations with electrical and optoelectronic properties of CuInSe₂ thin films

D. Abou-Ras, N. Schäfer, T. Rissom, M.N. Kelly, J. Haarstrich, C. Ronning, G.S. Rohrer, A.D. Rollett
Acta Materialia **118**, 244 (2016)

Insight into the unit cell: Structure of picene thin films on Ag(100) revealed with complementary methods

T. Huempfner, M. Hafermann, C. Udhardt, F. Otto, R. Forker, and T. Fritz
J. Chem. Phys. **145**, 174706 (2016)

Naphthalene's Six Shades on Graphite: A Detailed Study on the Polymorphism of an Apparently Simple System

F. Sojka, M. Meissner, T. Yamada, T. Munakata, R. Forker, and T. Fritz
J. Phys. Chem. C **120**, 22972 (2016)

Flexible 2D crystals of polycyclic aromatics stabilized by static distortion waves

M. Meissner, F. Sojka, L. Matthes, F. Bechstedt, X. Feng, K. Müllen, S.C.B. Mannsfeld, R. Forker, and T. Fritz
ACS Nano **10**, 6474 (2016)

- Optical transition energies of isolated molecular monomers and weakly interacting two-dimensional aggregates,*
R. Forker, T. Dienel, A. Krause, M. Gruenewald, M. Meissner, T. Kirchhübel, O. Gröning, and T. Fritz,
Phys. Rev. B **93**, 165426 (2016)
- Impact of a molecular wetting layer on the structural and optical properties of tin(II)-phthalocyanine multilayers on Ag(111)*
M. Gruenewald, J. Peuker, M. Meissner, F. Sojka, R. Forker, and T. Fritz
Phys. Rev. B **93**, 115418 (2016)
- Self-Assembly of Ultrathin Tetraphenyl-dibenzoperiflanthene (DBP) Films on Ag(111)*
T. Kirchhübel, M. Gruenewald, F. Sojka, S. Kera, F. Bussolotti, T. Ueba, N. Ueno, G. Rouillé, R. Forker, and T. Fritz
Langmuir **32**, 1981 (2016)
- Optical Observation of Different Conformational Isomers in Rubrene Ultra-Thin Molecular Films on Epitaxial Graphene*
C. Udhardt, R. Forker, M. Gruenewald, Y. Watanabe, T. Yamada, T. Ueba, T. Munakata, and T. Fritz
Thin Solid Films **598**, 271 (2016)
- Complex Stoichiometry Dependent Reordering of 3,4,9,10-Perylene-tetracarboxylic Dianhydride on Ag(111) upon K Intercalation*
C. Zwick, A. Baby, M. Gruenewald, O.T. Hofmann, R. Forker, G. Fratesi, G. P. Brivio, E. Zojer, and T. Fritz
ACS Nano **10**, 2365 (2016)
- Cosmic Dust VIII*
H. Kimura, L. Kolokolova, A. Li, H. Kaneda, C. Jäger, and J.-C. Augereau
Planet. Space Sci. **133**, 1-6 (2016)
- The CO-H₂ van der Waals complex and complex organic molecules in cold molecular clouds: A TMC-1C survey*
A. Potapov, Á. Sánchez-Monge, P. Schilke, U. U. Graf, Th. Möller, and S. Schlemmer
Astron. Astrophys. **594**, A117/1-A117/9 (2016)
- Ion-induced processing of cosmic silicates: A possible formation pathway to GEMS*
C. Jäger, T. Sabri, E. Wendler, and Th. Henning
Astrophys. J. **831**, 66/1-66/8 (2016)
- C₆₀ as a probe for astrophysical environments*
A. C. Brieva, R. Gredel, C. Jäger, F. Huisken, and Th. Henning
Astrophys. J. **826**, 122/1-122/11 (2016)
- Building carbon bridges on and between fullerenes in helium nanodroplets*
S. A. Krasnokutski, M. Kuhn, A. Kaiser, A. Mauracher, M. Renzler, D. K. Bohme, and P. Scheier
J. Phys. Chem. Lett. **7**, 1440-1445 (2016)

Self-assembly of tetraphenyldibenzoperiflanthene (DBP) films on Ag(111) in the monolayer regime

T. Kirchhübel, M. Gruenewald, F. Sojka, S. Kera, F. Bussolotti, T. Ueba, N. Ueno, G. Rouillé, R. Forker, and T. Fritz
Langmuir **32**, 1981-1987 (2016)

Ultra-low-temperature reactions of carbon atoms with hydrogen molecules

S. A. Krasnokutski, M. Kuhn, M. Renzler, C. Jäger, Th. Henning, and P. Scheier
Astrophys. J. Lett. **818**, L31/1-L31/5 (2016)

Cathodoluminescence and Raman spectromicroscopy of forsterite in Tagish Lake meteorite: Implications for astromineralogy

A. Gucsik, I. Gyollai, H. Nishido, K. Ninagawa, M. Izawa, C. Jäger, U. Ott, I. Simonia, S. Bérczi, and M. Kayama
Int. J. Spectrosc. **2016**, 1751730/1-1751730/8 (2016)

Hard X-ray irradiation of cosmic silicate analogs: Structural evolution and astrophysical implications

L. Gavilan, C. Jäger, A. Simionovici, J. L. Lemaire, T. Sabri, E. Foy, S. Yagoubi, T. Henning, D. Salomon, and G. Martinez-Criado
Astron. Astrophys. **587**, A144/1-A144/8 (2016)

Birefringence Measurements on Crystalline Silicon

C. Krueger, D. Heinert, A. Khalaidovski, J. Steinlechner, R. Nawrodt, R. Schnabel, H. Lueck
Class. Quantum Grav. **33**, 015012 (2016)

Internally shunted Josephson junctions: a unified analysis

V. Lacquaniti, C. Cassiago, N. De Leo, M. Fretto, A. Sosso, P. Febvre, V. Shaternik, A. Shapovalov, O. Suvorov, M. Belogolovskii, P. Seidel
IEEE/CSC & ESAS Superconductivity News Forum **35**, ST 494 (2016)

Anomalous inner-gap structure in transport characteristics of superconducting junctions with degraded interfaces

E. Zhitlukhina, I. Devyatov, O. Egorov, M. Belogolovskii, P. Seidel
Nanoscale Research Letters **11**, 58 (2016)

Planar hybrid Josephson junctions based on Ba-122 single crystals

N. Hasan, D. Reifert, S. Döring, S. Schmidt, V. Tympel, F. Schmidl, T. Wolf, P. Seidel
IEEE Trans. Appl. Supercond. **26**, 1100304 (2016)

Internally shunted Josephson junctions: a unified analysis

V. Lacquaniti, C. Cassiago, N. De Leo, M. Fretto, A. Sosso, P. Febvre, V. Shaternik, A. Shapovalov, O. Suvorov, M. Belogolovskii, P. Seidel
IEEE Trans. Appl. Supercond. **26**, 1100505 (2016)

The coherent dynamic state of intrinsic Josephson junctions

A. Grib, P. Seidel
IEEE Trans. Appl. Supercond. **26**, 1801004 (2016)

Mechanical loss of a hydroxide catalysis bond between sapphire substrates and its effect on the sensitivity of future gravitational wave detectors

K. Haughian, D. Chen, L. Cunningham, G. Hofmann, J. Hough, P. G. Murray, R. Nawrodt, S. Rowan, A. A. van Veggel, and K. Yamamoto
Phys. Rev. D **94**, 082003 (2016)

Intrinsic and extrinsic pinning in NdFeAs(O,F): vortex trapping and lock-in by the layered structure

C. Tarantini, K. Iida, J. Hänisch, F. Kurth, J. Jaroszynski, N. Sumiya, M. Chihara, T. Hatano, H. Ikuta, S. Schmidt, P. Seidel, B. Holzapfel, D.C. Larbalestier
Scientific Reports **6**, 36047 (2016)

Ion Beam Modification of Solids

W. Wesch, E. Wendler
Springer Series in Surface Sciences **61** (2016)

Ion-beam induced effects in multi-layered semiconductor systems

E. Wendler, N.A. Sobolev, A. Redondo-Cubero, K. Lorenz
Phys. Status Solidi B **253**, 2099 (2016)

Direction-dependent RBS channelling studies in ion implanted LiNbO₃

E. Wendler, G. Becker, J. Rensberg, E. Schmidt, S. Wolf, W. Wesch
Nucl. Instr. Meth. B **379**, 195 (2016)

Ion-implantation-induced amorphization of In_xGa_{1-x}P alloys as functions of stoichiometry and temperature

Z.S. Hussain, E. Wendler, W. Wesch, C.S. Schnohr, M.C. Ridgway
J. of Appl. Phys. **119**, 195702 (2016)

Mechanisms of Implantation Damage Formation in Al_xGa_{1-x}N Compounds

D.N. Faye, E. Wendler, M. Felizardo, S. Magalhaes, E. Alves, F. Brunner, M. Weyers, K. Lorenz
J. of Physical Chemistry **120**, 7277 (2016)

In-situ RBS studies of strontium implanted glassy carbon

O.S. Odutemowo, J.B. Malherbe, C.C. Theron, E.G. Njoroge, E. Wendler
Vacuum **126**, 101 (2016)

High temperature annealing studies of strontium ion implanted glassy carbon

O.S. Odutemowo, J.B. Malherbe, L. Prinsloo, D.F. Langa, E. Wendler
Nucl. Instr. And Methods B **371**, 332 (2016)

Comparative study of the effect of swift heavy ion irradiation at 500 degrees C and annealing at 500 degrees C on implanted silicon carbide

T.T. Hlatshwayo, J.H. O'Connell, V.A. Skuratov, E. Wendler, E.G. Njoroge, M. Mlambo, J.B. Malherbe
RSC Advances **6**, 68593 (2016)

3.2 Invited Talks at Conferences and Colloquia

T. Fritz:

Incommensurate growth and static distortion waves in 2D crystals of polycyclic aromatics
European Advanced Materials Congress – 2016 (EAMC 2016), Stockholm (Schweden),
23.08.2016

Epitaxy without coincidences – the stabilizing role of static distortion waves
International Conference on Internal Interfaces (ICII-2016), Marburg, 31.05.2016

C. Ronning:

Semiconductor nanowire photonics
Bio-Nano-Quantum Seminar, Universität Hamburg, 13.12.2016

Sputtering and redeposition of ion irradiated Au nanoparticle arrays
MRS fall meeting, session PM1, Boston, USA, 30.11.2016

Ion beam designed metasurfaces
BuildMo Na Thematic module “Metamaterials”, University of Leipzig, 29.09.2016

Ion-Nanostructure Interactions
Physics Colloquium, University of KwaZulu-Natal, Durban, South Africa, 10.08.2016

High resolution investigations of CIGSe solar cells
Physics Colloquium, Durban University of Technology, Durban, South Africa, 10.08.2016

Metasurfaces based on defect-engineered phase transition materials
META'16, 7th International Conference on Metamaterials, Photonic Crystals and Plasmonics,
Malaga, Spain, 28. July 2016

Hochauflösende Untersuchungen an CIGSe-Solarzellen
Seminar of the ISFH Institute, Hameln, 31. Mai 2016

Semiconductor nanowire photonics
Sino-German Workshop on “Nanophotonics”, Tübingen, 5. April 2016

Ion-Solid-Interactions@Jena
Vinca Institute of Nuclear Science, University of Belgrade, Serbien, 29. März 2016

Dynamics and Emission Characteristics of Semiconductor Nanowire Lasers
46th Winter Colloquium on Physics of Quantum Electronics, Snow Bird, USA, 4. Jan. 2016

P. Seidel:

Josephson junctions with iron-based superconductors
MRS Spring Meeting 2016, Phoenix, Arizona, USA, 29.03.2016

Josephson junctions with iron-based superconductors
Plasma+, 10th International Symposium on Intrinsic Josephson Devices and Plasma Oscillations
in High-Tc superconductors, Nanjing, China, 12.10.2016

C.S. Schnohr:

Complex semiconductors: From atomic-scale structure to band gap bowing
Seminar Halbleiterphysik, Universität Leipzig, 9.11.2016

R. Röder:

Semiconductor nanowire photonics

Physics Colloquium, University of KwaZulu-Natal, Durban, South Africa, 08.08.2016

E. Wendler:

Ion-beam induced effects in multi-layered semiconductor systems

E-MRS Spring Meeting, Symposium BB, Lille (France), 04.05.2016

C. Jäger:

Formation routes of cosmic dust

European Conference on Laboratory Astrophysics ECLA2016

"Gas on the Rocks", Madrid, Spain, 21.-25. November 2016

Experimental emergence of carbonaceous molecules; PAHs and fullerenes

International workshop on the 'The past and future of AstroPAH research',

Noordwijk, Netherlands, 30. October – 04. November 2016

G. Rouillé:

Cold synthesis of carbon and silicate dust

International Conference on 'Multiple Faces of Interstellar Dust'

Garching, Germany, 13-16 September 2016

M. Thürk:

Optical Cooling

DKV-Tagung, Kassel, 16.-18. 11. 2016

3.3 Theses

(A) Bachelor Theses and Studienarbeiten

Clemens Anschutz	<i>Elektrische in-situ Untersuchung von ionenbestrahlten Vanadiumdioxid Dünnschichten</i>
Philipp Jagusch	<i>Experimentelle Untersuchungen und Simulationen zum Nukleationsverhalten magnetischer Domänen in polygonalen GMR-Nanodrähten</i>
Robert Kraft	<i>Elektrische und elektrooptische Untersuchung von Kalium-implantierten CIGS-Dünnschichtsolarzellen</i>
Polina Mednikova	<i>Wachstum von ZnO-Nanostrukturen auf amorphen Fasern</i>
Maximilian Schaal	<i>Untersuchung der elektronischen Eigenschaften von 1,2;8,9-Dibenzopentacen auf verschiedenen Metalleinkristallen</i>
Lennart Vorbrink	<i>Untersuchung des Schichtwachstums von Dibenzopentacen auf Ag(111)</i>

(B) Diploma, Master Theses, and State Examination Theses

Nicole Danner	<i>Analyse von elektrischen und optischen Eigenschaften von Halbleitern</i>
Walter Dickmann	<i>Emissionscharakteristik einzelner CdS-Nanodrähte und ZnO-Mikrostäbe</i>
Johannes Dickmann	<i>Optische Absorption von hochreinem Silizium</i>
Elisabeth Golbing	<i>Untersuchung des mechanischen Verlusts von Stimmgabelresonatoren</i>
Martin Hafermann	<i>Wachstum und Dotierung von ultradünnen Picenschichten auf Ag(100)</i>
Leonie Kaczmarek	<i>Elektrische Untersuchungen an SQUID-Strukturen auf der Basis von Mit Au-NP wachstumsmodifizierten YBCO-Korngrenzenkontakten</i>
Felix Küster	<i>Electron Correlations in and Temperature Dependent Physical Properties of Axially Substituted Metal-Phthalocyanines</i>
Torsten Lindemann	<i>Nachweis von optischen Resonanzen in Halbleiter-Nanodrähten mittels eines Rasterlumineszenzmikroskops und deren Modifizierung</i>
Shiva Mohammadzadeh	<i>Design and realization of a terahertz line-scanner</i>
Kevin Murray	<i>Thermische Eigenschaften und Spannungsminimierung in La/B-basierten EUV-Multilayersystemen</i>
Sebastian Oehler	<i>Untersuchungen zur Wechselwirkung von NP auf das Wachstum von mittels PLD abgeschiedenen YBCO Schichten</i>
Konrad Ritter	<i>Kernreaktionsanalyse an Lithiumniobat</i>
Lisa Schade	<i>Optische Eigenschaften von funktionalisierten Halbleiternanodrähten</i>
Lukas Trefflich	<i>Untersuchungen von Nanodraht-basierten kohärenten Lichtquellen</i>
Enrico Treiber	<i>Ionenimplantation von β-Ga₂O₃</i>
Florian Wittkämper	<i>Untersuchungen zur Schichtdickenabhängigkeit bei YBCO Schichten mit Au – NP</i>
Maximilian Zapf	<i>Emission tuning of CdS nanowires by temperature and strain</i>
Anton Zimare	<i>Entwicklung und Charakterisierung einer gepulsten Speicherionenquelle</i>

(C) PhD Theses

Davide Cammi	<i>Photoconductivity and gas sensing properties of ZnO nanowire devices</i>
Noor Hasan	<i>Preparation and characterization of planar hybrid Josephson junctions based on Ba-122 Prictide single crystals</i>
Gerd Hofmann	<i>Untersuchungen an Bulkmaterialien für rauscharme, kryogene Interferometer</i>

Henry Holland-Moritz	<i>Ion-nanostructure interaction: Comparing simulation and experiment towards surface structuring using nanoparticles</i>
Julius Komma	<i>Optische Eigenschaften von Substratmaterialien für zukünftige kryogene Gravitationswellendetektoren</i>
Matthias Meißner	<i>Non-Commensurate Epitaxy of Organic Layers</i>
Gregor Oelsner	<i>Lasing eines einzelnen, künstlichen Atoms realisiert durch ein getriebenes Flussqubit</i>
Robert Röder	<i>Semiconductor nanowire based coherent light sources: temporal dynamics and tunability</i>
Sven Schönherr	<i>Elektro - optische Untersuchungen von CIGSe – Dünnschicht-solarzellen</i>
Florian Talkenberg	<i>Halbleiter-Isolator-Halbleiter-Heteroübergang mit Atomlagenabscheidung als Schottky-Tunnel-Solarzelle auf nanostrukturiertem Silizium</i>
(D) Habilitation	
Dr. Claudia S. Schnohr	<i>Complex semiconductors: From atomic-scale structure to band gap bowing</i>

4. Cooperations, Visiting Scientists, and Colloquia at the IFK

4.1 Cooperations

The Institute of Solid State Physics collaborates with a large number of Institutes and Universities in Germany and around the world and has also close connections with several companies. In the framework of these wide spread contacts a large number of scientists from various countries visited our Institute in 2015 to perform experiments, discuss scientific results obtained within joint projects and to give talks in the colloquium of the Institute of Solid State Physics.

The Surface Science group of **Prof. Dr. T. Fritz** strengthened their international cooperations in 2016. The ongoing collaboration with Japan was continued and extended to the Institute of Molecular Science, Okazaki, group of Prof. Dr. S. Kera. In the USA we cooperate with the groups of Prof. Dr. O. Monti and Prof. Dr. N.R. Armstrong (University of Arizona). Within Europe we have intensive collaborations with the theory groups of Prof. Dr. E. Zojer (Graz University of Technology) and Prof. Dr. G.-P. Brivio (Universita di Milano-Bicocca). In Germany our collaborations include the group of Prof. Dr. C. Kumpf (Forschungszentrum Jülich GmbH), Prof. Dr. J. Kröger (TU Ilmenau), and the University Würzburg (Profs. F. Reinert and A. Schöll).

The group of **Prof. Dr. C. Ronning** collaborated in 2016 with various international groups. Special situations have been established with the groups of Prof. Dr. F. Capasso (U Harvard), Prof. Dr. M. Kats (U Wisconsin), Prof. A. Lugstein (TU Vienna), Prof. A. Fontcuberta i Moral (EPF Lausanne), and Prof. K. Bharuth-Ram (iThemba Labs, South Africa), which have been founded either by the DAAD or AvH. Further collaborations have been conducted with the groups at the Australian National University Canberra (Australia, Dr. P. Kluth), University of Southern California (USA, Prof. J.G. Lu), University of Florence (Italy, Dr. F. di Benedetto), University of the Basque Country (Spain, Prof. A. Rubio), ERSF Grenoble (France, Dr. G. Martinez-Criado, Dr. M. Burghammer & Dr. F. d'Acapito), Vinca Nuclear Institute in Belgrade (Prof. Z. Rakocevic), and Imperial College (UK, Dr. R. Oulton & Prof. O. Hess). National collaborations involve partners from Bremen, Duisburg, Mainz, Leipzig, Braunschweig, and Erlangen within the frame of the DFG research unit FOR1616. In the field of photovoltaics, ongoing collaborations include groups at the HZ Berlin, FHI Berlin, Manz AG, and ZSW Stuttgart.

The Low Temperature Physics group of **Prof. Dr. Paul Seidel** is collaborating with Thuringian research institutions (TU Ilmenau, IPHT Jena, SUPRACON Jena, Innovent e.V. Jena, Helmholtzinstitut Jena). Within funded research projects joint research is carried out with the IFW Dresden, the GSI Darmstadt, the DESY Hamburg, the MPI Heidelberg and the CERN Genf. Long-term collaborations exist to the Karlsruhe Institute of Technology KIT and the research groups at the universities in Erlangen-Nürnberg, Hannover, Dresden, Gießen, Heidelberg, Tübingen as well as the Universities of Applied Science in Aalen and Jena. Scientific results have been obtained in close collaboration with national (Hannover, Tübingen, Golm, Garching) as well as international partners, such as the universities of Glasgow, Padova, Lyon, Tokyo, Pisa, Salerno, Roma, Moscow and others. Additional international partners in the field of superconducting materials and its application are the universities of Bratislava, Poznan,

Twente, Donetsk, Kharkov, Osaka, Nagoya and Tokyo.

The ion beam physics group of **Prof. Dr. Elke Wendler** cooperated in 2016 with Prof. Dr. Fadei F. Komarov (BGU Minsk), Prof. Dr. Maria Katsikini (U Thessaloniki), Dr. Katharina Lorenz (IST, U Lissabon), Prof. Dr. Johan B. Malberbe (U Pretoria), Dr. Alexander Yu. Azarov (U Oslo). National cooperations exist with Dr. Klaus Ellmer (HZ Berlin).

The laboratory astrophysics and cluster physics group of **Dr. Cornelia Jäger** collaborated with Prof. Dr. S. Price, University College London, Dr. Lisseth Gavilan from Institut d'Astrophysique Spatiale (CNRS, Paris), Prof. P. Scheier, University of Innsbruck, and Prof. E. Kovacevic (GREMI, Université d'Orléans). Strong collaborations with German groups exist with Prof. Dr. P. Caselli (MPI for Extraterrestrial Astrophysics, Munich), Dr. S. Zhukovska (MPI for Astrophysics, Munich), Prof. Gerhard Wurm (University of Duisburg), Prof. Dr. S. Schlemmer (Cologne Laboratory Astrophysics Group), Prof. T. Giesen (Laboratory Astrophysics Group at the University Kassel), and Dr. Holger Kreckel (Max Planck Institute for Nuclear Physics, Heidelberg).

4.2 Visiting Scientists

Dr. K. Yonezawa	Okazaki (Japan)
MSc. T. Yamaguchi	Okazaki (Japan)
MSc. Calley Eads	Tucson (Arizona)
Prof. Dr. Krish Bharuth-Ram	Durban University of Technology (South Africa)
Vusumuzi Masondo	Durban University of Technology (South Africa)
Prof. Dr. Mikhail Kats	University of Wisconsin @ Madison (USA)
Dr. Svitlana Zhukovska	Max-Planck-Institut für Astrophysik Garching
Dr. Alexander Yu. Azarov	University of Oslo (Norway)
MSc. Maksim Makhavikou	Belorussian State University, Minsk (Belarus)
MSc Opeyemi Odutemovo	University of Pretoria (South Africa)
Dr. L. Ulasukova	Belorussian State University (Belarus)
Prof. Dr. Liang-Ling Wang	Shandong University, Jinan (China)
Dr. Milos Nenadovic	Vinča Institute of Nuclear Sciences, Belgrade (Serbia)
Dr. Maja Popovic	Vinča Institute of Nuclear Sciences, Belgrade (Serbia)
Dr. Mirjana Novakovic	Vinča Institute of Nuclear Sciences, Belgrade (Serbia)
Danilo Kisic	Vinča Institute of Nuclear Sciences, Belgrade (Serbia)
Dr. Mikhail Belogolovskii	Donetsk Physical and Technical Institute, National Academy of Sciences of Ukraine (Ukraine)
Dr. Olena Zhytlukhina	Donetsk Physical and Technical Institute, National Academy of Sciences of Ukraine (Ukraine)
Prof. Dr. Kentaro Somiya	Tokyo Technical University, Japan

4.3 Colloquia at the Institute of Solid State Physics

PD Dr. Heidemarie Schmidt (TU Chemnitz), 8. Jan. 2016

Magneto-optical properties of metals, half-metals, and garnets

Prof. Dr. Wolf Widdra (Martin Luther Universität Halle-Wittenberg), 22. Jan. 2016

From Perovskite Interfaces to aperiodic 2D oxide quasicrystals

Dr. Christian Kaufmann (HZ Berlin), 29. April 2016

Current topics in CIGS photovoltaic research at the PVcomB

Prof. Dr. Thomas Schäpers (FZ Jülich), 13. Mai 2016

Phase-coherent and ballistic transport in InAs-based nanowires

Prof. Dr. Enrico Gnecco (FSU Jena, OSIM), 27. Mai 2016

Controlled scanning probe manipulation and lithography: What can be learned on nanoscale friction and abrasive wear

Prof. Dr. Gerhard Wurm (Universität Duisburg-Essen), 10. Juni 2015

From Planet Formation to Dust Devils on Mars: Some Physics of (Cohesive) Granular Matter in Radiation Fields at Low Ambient Pressure

Prof. Dr. Michael Gottfried (Philipps Universität Marburg), 24. Juni 2016

Surface Science of Porphyrins, Phthalocyanines, and Corroles

Jun.-Prof. Dr. Benjamin Stadtmüller (Technische Universität Kaiserslautern), 8. Juli 2016

A momentum space view on electronic states and electron dynamics of molecular adsorbate systems

Prof. Dr. Susan Schorr (HZ Berlin & FU Berlin), 11. Nov. 2016

A structural perception about intrinsic point defects in kesterite type compound semiconductors

Dr. Kay Potzger (Helmholtz-Zentrum Dresden-Rossendorf), 9. Dez. 2016

Magnetic properties tuned by defects - the role of ion beam techniques

5. Personnel

Professors

Prof. Dr. habil. Torsten Fritz
Prof. Dr. habil. Carsten Ronning
apl. Prof. Dr. habil. Frank Schmidl
Prof. Dr. habil. Paul Seidel
apl. Prof. Dr. habil. Elke Wendler

Scientific Staff

Dr. Abel Brieva	Dr. Alexey Potapov
Dr. Roman Forker	Dr. Udo Reislöhner
Dr. Ernst Glaser	Dr. Gael Rouillé
Dr. Cornelia Jäger	Dr. Bernd Schröter
Dr. Andreas Johannes	PD Dr. Claudia Schnohr
Dr. Sergiy Krasnokutski	Dr. Sven Schönherr
Dr. Ronny Nawrodt	Dr. Volker Tympel

PhD Students

Davide Cammi	Konrad Ritter
Stefanie Eckner	Robert Röder
Rene Glaser	Philip Seeber
Martin Gnauck	Emanuel Schmidt
Marco Grünewald	Stefan Schmidt
Martin Hafermann	Philipp Schöppe
Yaser Haj-Hmeidi	Falko Sojka
Henry Holland-Moritz	Jura Rensberg
Tobias Hümpfner	Christian Udhardt
Tino Kirchhübel	Hagen Walter
Felix Otto	Maximilian Zapf
Ali Hasan Noor	Christian Zwick

Extern PhD Students

Constantin Csato	FH Jena
Florian Krippendorf	FH Jena
Gregor Oeslner	IPHT Jena
Stephan Ruoff	MPI Stuttgart
Matthias Rost	Bosch Solar EnergySolarworld, Arnstadt
Thomas Schönau	IPHT Jena
Charlotte Weiss	Fraunhofer ISE, Freiberg

Diploma and Master Students

Walter Dickmann
Johannes Dickmann
Paul Gerlach
Leonie Kaczmarek
Sascha Kreutzburg
Paul Kutza
Felix Küster

Torsten Lindemann
Marie Mende
Sebastian Oehler
Lisa Schade
Enrico Treiber
Lukas Trefflich
Florian Wittkämper

External Diploma and Master Students

Shiva Mohammadzadeh (Fraunhofer KL)
Kevin Murray (Fraunhofer Jena)
Anton Zimare (Vacom)

Technical Staff

Ulrich Barth
Cindy Büchner
Uwe Eberhardt
Tobias Eißmann
Lutz Föllmer
Silke Frunzke
Kristina Garlipp
Frank Jehn
Patrick Hoffmann

Holger Mühlig
Anja Mittelstädt
Ralf Neubert
Stefan Prass
Helga Rudolph
Sylvia Stender
Matthias Thürk
Carmen Voigt

6. Technical Reports and Equipment

6.1 Operation of the Ion-Accelerator JULIA and the Ion-Implanter ROMEO

U. Barth, P. Hoffmann, F. Jehn, C. Ronning

The 3 MV high current tandetron accelerator JULIA (Jena University Laboratory for Ion Acceleration) went in operation end of 1996. Since the beginning of the routine-operation in 1997 it has been used for different types of experiments requiring a broad spectrum of ion-beams. With the exception of helium, where the duoplasmatron ion-source followed by a lithium exchange channel was used, all ions were extracted from a sputter-type ion-source. The beam-on-target-time of 1300 h was a little bit higher than in 2015.

The 400 kV ion-accelerator ROMEO is in routine operation since 1998, here the beam-on-target-time of 1300 h was also 10 % higher as in the preceding years. Both accelerators can be operated separately or in combination. The ion-beams produced until 2016 are summarized in table 1. The ion-beam currents quoted are typical values of the ion source currents used for the experiments.

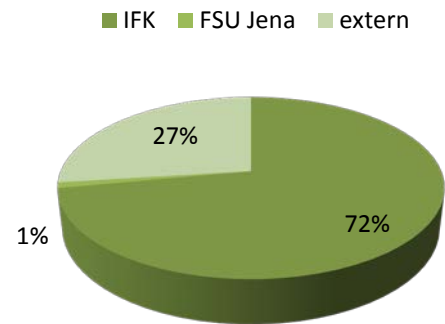
Period	Element	Julia	Romeo	Period	Element	Julia	Romeo	
1	Hydrogen (H)	1 μ A	4 μ A	4	Germanium (Ge)	1,6 μ A	4 μ A	
	Helium (He)	0,1 μ A	4 μ A		Arsenic (As)	0,4 μ A	1 μ A	
2	Lithium (Li)	2 μ A	-		Selenium (Se)	0,5 μ A	1,5 μ A	
	Boron (B)	0,1 μ A	5 μ A		Krypton (Kr)	-	10 μ A	
	Carbon (C)	3 μ A	1 μ A	5	Strontium (Sr)	-	3 μ A	
	Nitrogen (N)	0,4 μ A	4 μ A		Yttrium (Y)	-	4 μ A	
	Oxygen (O)	2 μ A	2 μ A		Rhodium (Rh)	0,2 μ A	-	
	Flourine (F)	-	2 μ A		Palladium (Pd)	0,09 μ A	1 μ A	
	Neon (Ne)	-	5 μ A		Silver (Ag)	1,6 μ A	10 μ A	
	3	Sodium (Na)	-		6 μ A	Cadmium (Cd)	-	0,8 μ A
		Magnesium (Mg)	-		5 μ A	Indium (In)	0,5 μ A	8 μ A
Aluminium (Al)		-	4 μ A		Tin (Sn)	1,0 μ A	3 μ A	
Silicon (Si)		2 μ A	4 μ A		Iodine (I)	3 μ A	-	
Phosphorus (P)		1 μ A	4 μ A	Xenon (Xe)	-	10 μ A		
Sulfur (S)		1 μ A	-	6	Caesium (Cs)	-	4 μ A	
Chlorine (Cl)		-	2 μ A		Samarium (Sm)	0,01 μ A	1,5 μ A	
Argon (Ar)		-	20 μ A		Europium (Eu)	0,03 μ A	2 μ A	
4	Potassium (K)	-	3 μ A		Erbium (Er)	0,04 μ A	2 μ A	
	Manganese (Mn)	0,02 μ A	5 μ A		Thulium (Tm)	-	1 μ A	
	Iron (56 Fe)	0,8 μ A	2 μ A		Tungsten (W)	0,3 μ A	0,01 μ A	
	Iron (57 Fe)	-	0,015 μ A		Osmium (Os)	0,05 μ A	-	
	Copper (Cu)	0,5 μ A	1 μ A		Platinum (Pt)	0,2 μ A	-	
	Zinc (Zn)	0,05 μ A	6 μ A	Gold (Au)	2,8 μ A	20 μ A		
	Gallium (Ga)	-	3 μ A	Lead (Pb)	0,03 μ A	15 μ A		

Table 1: Ion-beams accelerated until 2016. The currents given were measured at the Q-Snout-Faraday-cup after the low-energy mass separator (JULIA) and at the target position (ROMEO), respectively.

As in the preceding years the ion-beam facility was used by external research groups:

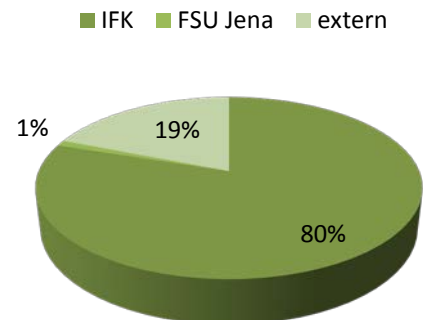
3 MV-Tandetron „JULIA”

- Belarusian State University, Minsk, Belarus
Prof. F.F. Komarov, Dr. L. Ulasukova,
MSc. M. Makhavikou
- Oak Ridge National Laboratory, Oak Ridge, USA
Prof. Y. Zhang, Dr. G. Velisa
- Shandong University, Jinan, China
Prof. L.-L. Wang
- University of Belgrade
Vinča Institute of Nuclear Sciences
- IPHT Jena
Dr. Diegel



400kV Implanter „ROMEO“

- Knoxville, USA
Oak Ridge National Laboratory
- Durban University of Technology, Pretoria
Krish Bharuth-Ram
- Belarusian State University, Minsk, Belarus
Prof. F.F. Komarov, Dr. L. Ulasukova,
MSc. M. Makhavikou
- Institut für angewandte Physik, FSU
- Institut für Optik und Quantenelektronik, FSU



6.2 Cryogenic Services (TTS)

M. Thürk

All in-house customers of cryogenic liquids, which are all faculties of natural sciences, the university medical division including several hospitals, and other external scientific institutes (e.g. Institute for Photonic Technology Jena, Leibniz Institute Hans-Knöll Jena) as well as some private customers like the Innovent e.V. Jena and some medical practices, were provided with liquid helium (LHe), with high purity gases (He, N₂), and with cryogenic gases like liquid nitrogen (LN₂) and liquid argon (LAr) by the Cryogenic Services. Roughly 119,000 litres of LN₂ were delivered by the cryogenic services in 2015. The total delivery has been levelled out over the last years due to the by now stabilized demands of inert gas in the IAAC-institute and the new installed ZAF site.

As illustrated in Figure 1, the output of liquid helium (LHe) has decreased in 2015. Roughly 33,000 litres of LHe were delivered which calls for an annual gross refrigeration value of just 40,600 litres which corresponds to an annual all round price of €0.45 million. Last three years we had to face a worldwide shortage in helium supplies which leads generally to increased costs with persistent fierce fluctuations of the competitive market price over the year. On the crest of the wave the costs for short term LHe-orders have increased by a fivefold. Therefore the financial weakness and supply shortfall have caused a strong reduction in LHe-use since

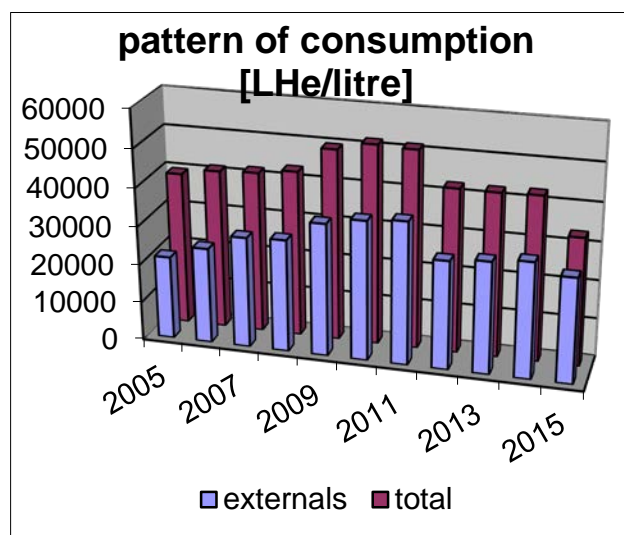


Figure 1 Liquid helium output.

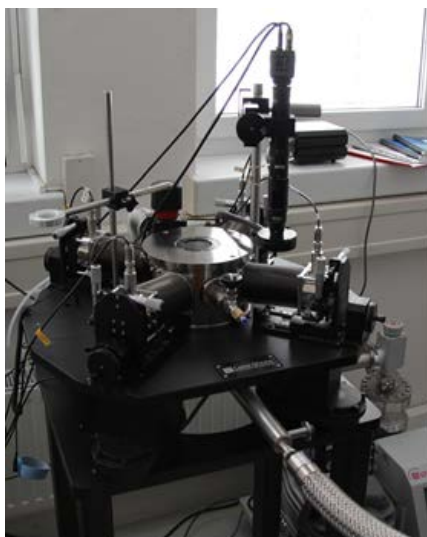


Figure 2: Lake Shore TTPX probe station.

2012. Fortunately the relation between the produced amount of LHe to the bought quantity was a good deal bigger than the years before 2012 to 2013. In spite of the lower production rate the rising market prices increased the gross financial benefits of the internal helium liquefaction for all users noticeably. Mentoring of scientists using new standard cryogenic equipment has become more important over the previous periods. Last year the TTS staff has carried out advisory services to implement proper cryogenic procedures on various new acquired scientific installations. Some of the finest examples are a new NMR-instrument, a cryo-vacuum pump, a He-3 refrigerator and a low temperature probe station which is presented in Fig. 2. The project “helium-recovery” for the Max-Wien-Platz 1 site is under way.

6.3 Equipment

Preparation of Thin Films and Devices

- HV evaporation facilities for thermal and electron beam evaporation
- UHV evaporation facilities, including electron gun and in situ RHEED system
- Equipment for laser deposition of thin crystalline films and material systems, especially high temperature superconductors (KrF excimer laser, $\lambda = 248$ nm)
- Molecular Beam Epitaxy (MBE) facilities: MBE for silicon carbide (RIBER EVA 32 R&D)
- Organic Molecular Beam Epitaxy (OMBE) facilities including surface analysis techniques (MCP-LEED, UHV STM/AFM, RHEED) and *in situ* optical spectroscopy (PL and DRS)
- dc and rf sputtering systems for metallic (Au, Ti) and oxidic (SiO_2 , Ta_2O_5) thin films and multilayers
- Ion beam etching with Ar ions at sample temperatures down to 80 K in vacuum
- Chamber for ion- and reactive etching up to 4" wafer
- Reactive ion beam etching with sample diameters up to 6 cm
- Ultrasonic wire bonder
- Equipment for photolithographic patterning
- MBE system NEBULA for $\text{Cu}(\text{In,Ga})\text{S}_2$ layers on 4" substrates including RHEED setup
- Two HV systems for closed-space sublimation (CSS) for deposition of CdTe layers
- RF reactive sputtering system for transparent conducting oxides (TCO's) and molybdenum
- DC sputtering system for copper and indium
- UHV system ULS400 for $\text{Cu}(\text{In,Ga})(\text{Se,S})_2$ on (100x100) mm² substrates
- Wet chemical processing and chemical bath deposition of photoactive layers

Surface Analysis Systems

- LT-STM/AFM (1.1 K) with 3 Tesla magnet, QMS (1000 amu), MCP-LEED, DRS
- Surface analysis systems SPECS and UNISPEC with XPS, UPS, AES, LEED, STM
- AUGER electron spectrometer
- Atomic force microscopes (AFM and Microstructure Measuring Device VERITEKT 3 with needle sensor)
- Surface profilometer DEKTAK 100
- Scanning electron microscopes
- Several UHV-scanning probe devices (STM, AFM)

Electrical Measurement Techniques

- Electrical transport measurements (resistance, critical current density, point contact and tunneling spectroscopy)
- Hall-effect and Four-point probe equipment
- Current-voltage characteristics ($2 \text{ K} < T < 300 \text{ K}$, $B \leq 5 \text{ T}$)
- Current-voltage characteristics by microwave irradiation ($2 \text{ GHz} < f < 300 \text{ GHz}$)
- Noise measurements (frequency range 60 μHz - 100 kHz) at low temperatures
- LTS-SQUID characterization at 4.2 K (current-voltage, flux-voltage, noise, screening properties)
- HTS-SQUID characterization up to 100 K (current-voltage, flux-voltage, noise)
- 2 Deep level transient fourier spectrometers (temperature range 80 K - 690 K, 30 K - 330 K)
- 3 Admittance spectrometers (frequency range 40 Hz - 100 kHz, 20 Hz - 2 MHz and 75 kHz - 30 MHz, temperature range 30 K - 690 K)

- Microwave signal generator (frequency range 1 - 20 GHz, resolution: 1 kHz)
- Electrical and optical characterization of high power diode laser arrays

Equipment for Optical Characterization

- UV-VIS spectrometer
- FTIR spectrometer
- Cathodoluminescence at SEM, equipped for IR - UV
- Micro-Photoluminescence, IR-UV, time-resolution ~ 1ns
- Photoluminescence excitation (PLE)
- Optical cryostats (2...300 K) for optical absorption, photoluminescence and Raman spectroscopy
- Excitation lasers in a wide range from 405-1550 nm (fiber, gas, solid state and diode lasers)
- Optical microscopes
- Magnetrelaxation of ferrofluids (MORFF) for characterization of magnetic nanoparticles

Equipment for Electro-Optical (Solar) Characterization

- Solar simulator (AM 1.5) with Current-Voltage measurement
- Illuminated Current-Voltage measurements for 10 K to RT
- Quantum efficiency (EQE) measurements of solar cells

Equipment for Thermal Treatment

- Furnace for conventional thermal treatment in inert gas atmosphere or vacuum (temperatures up to 2050 K)
- RTA apparatus (double graphite strip heater) for short time annealing (annealing time in the order of seconds, temperature range 1000 K to 1950 K, temperature rise rate 100 K s⁻¹)

Electron Microscopy

- Scanning electron microscope JEOL JSM-6490 with LaB₆-cathode
- FEI field-emission electron microscope connected with FIB system

Ion Beam Techniques

3 MV Tandetron accelerator "JULIA", equipped with

- Sputter ion source and Duoplasmatron source
- Universal beam line for ion implantation and ion beam analysis
- Second beam line for ion beam analysis, combined with implantation chamber of 400 kV implanter
- Irradiation chamber with cooled and heated sample holder and four axis goniometer

Application:

- Ion implantation: energy range 500 keV - 12 MeV, temperature range 15 K - 1500 K
- Ion beam analysis: RBS and PIXE in combination with channeling, ERDA, NRA

400 kV implanter "ROMEO", equipped with

- Hot filament, hollow cathode ion source
- Irradiation chamber with cooled and heated sample holder and four axis goniometer, combined with beam line of 3 MV Tandatron accelerator

Application:

- Ion implantation: energy range 20 keV - 400 keV, temperature range 15 K - 1500 K
- Ion implantation at low temperatures and subsequent RBS analysis using H- or He-ions from 3 MV Tandatron accelerator

Low Energy implanter "LEILA", equipped with

- Colutron Ion source 100-Q
- Colutron Ion Gun System G-2-D
- Irradiation chamber with heated sample holder

Application:

- Irradiation of surfaces: energy range sub-keV, temperature range 300 K - 750 K

Low Energy implanter "Mr. JIM Stringer", equipped with

- Hot filament, hollow cathode ion source
- Irradiation and deposition chamber

Application:

- Deposition of diamond-like thin films: energy range 100eV – 30 keV, RT

Focused Ion Beam system FEI NanoLab Helios 600i

- Liquid ion source, E = 500 eV – 30 keV
- Electron microscope, E = 350 eV – 30 keV

Application:

- TEM-lamella preparation, etc.

Low Temperature Measuring Equipment

- LT STM/AFM down to 1.1 K. 3 Tesla magnet available
- He-4 cryostats for temperatures down to 4.2 K
- He-4 refrigerator for the temperature range 1.3 K - 4.2 K
- [Cryostat](#) for temperatures range 4,2K - 300 mK with superconducting magnet to 2 T
- He-3/He-4 dilution refrigerator for temperatures range 4,2 K - 6 mK with superconducting magnet to 10 T
- He-3/He-4 dilution refrigerator with a base temperature of 35 mK
- Electronic equipment for characterization of cryoelectronic devices
- SQUID sensor systems for magnetic measurements under unshielded conditions
- SQUID sensor system for spatially resolved magnetorelaxometry
- Cryostats (2 K < T < 300 K; optical window; magnetic field)
- Cryocoolers (Gifford-McMahon and Stirling)
- Pulse tube refrigerators (for sensor cooling)

7. Scientific Reports

High temperature limit of CdS semiconductor nanowire lasers

Maximilian Zapf, Carsten Ronning, and Robert Röder

Coherent light sources on the nanoscale are strongly sought-after devices for novel, visionary concepts in nanospectroscopy, optical nanosensing [1, 2], or ultrafast all-optical modulators [3]. In particular, semiconductor nanowires (NWs) have gained a lot of interest for these devices, as they inherently provide the requirements for laser emission, such as optical gain and a resonator structure. However, a severe issue for future NW laser applications is the devices' ability to provide stable laser oscillations, especially at harsh conditions such as elevated temperatures.

In order to avoid destructive processes, a fundamental understanding about these mechanisms in nano laser devices is indispensable for maintaining reliable devices. The material degradation in optically pumped NW lasers is associated with a dramatic decrease of the output intensity of the nano laser with increasing pump intensity. Figure 1 depicts the luminescence intensity as a function of pumping power of a single CdS NW laser at room temperature in a log-log plot. Four different working regimes, which are separated by three threshold values, can be identified. The linear slope of the spontaneous emission below ~ 70 kW/cm² changes into a superlinear increase, indicating amplified spontaneous emission (ASE), at the ASE threshold, TH_{ASE} . At the lasing threshold, TH_{Lasing} , the power dependence returns into a linear regime (above ~ 120 kW/cm²); this reveals stable laser oscillations in the individual CdS NW. Additionally, a multimode laser model [4] clearly fits the experimental data up to a pump power of ~ 140

kW/cm². However, if the pump power exceeds values of ~ 150 kW/cm², an immediate drop of the NW laser emission becomes apparent (see figure 1); this point is defined as the degradation threshold, $TH_{deg.}$

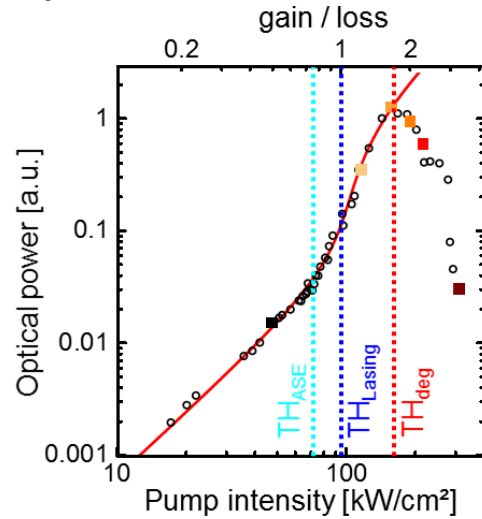


Fig. 1: Double logarithmic power dependence of the optical output power emitted from a CdS nanowire at room temperature as a function of the pump intensity indicating the typical lasing behavior up to pump intensities of ~ 150 kW/cm². The intensity drop for higher intensities indicates a degradation of the active laser material. The power dependence below unambiguously fits a multimode laser model (red line) [4]. The vertical lines indicate the transitions from spontaneous emission to amplified spontaneous emission (ASE) (cyan), the laser threshold (blue) and the threshold for a degradation of the active laser material (red).

The luminescence emission intensity drops by almost two orders of magnitude, when the pump power is increased from 150 kW/cm² to 300 kW/cm². This irreversible reduction of the output power results from a degradation of the active material. In order to estimate an upper temperature

limit for lasing, temperature dependent measurements were performed by placing the CdS NW sample in a helium flow cryo-state. Additionally, better statistics and further insights into the nature of these threshold parameters are achieved by investigating a number of CdS NW laser devices. The three threshold values for 35 NWs – 5 NWs for each of the 7 temperature steps – were determined from 4 to 300 K. The respective mean values are depicted as a function of temperature in figure 2, including the standard deviation as error bars.

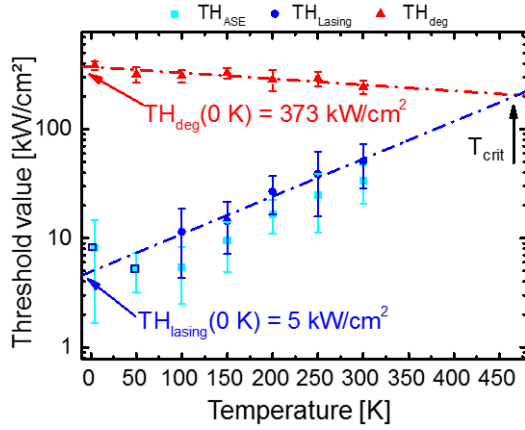


Fig. 2: Mean threshold values as a function of the temperature. The errors bars depict the standard deviation of the five nano lasers measured for each temperature. The lasing (blue) and degradation threshold (red) follow an exponential function, as indicated by the dash-dot lines. The extrapolated threshold values for 0 K are given in the graph as well as the extrapolated crossing point T_{crit} at ~ 470 K, at which the lasing threshold should approximately exceed the degradation threshold. Thus, stable laser oscillations are only accessible for $T < T_{crit}$.

Obviously, the laser threshold of the CdS NWs increases exponentially, following $TH_{Lasing}(T) = TH_{Lasing}^0 \exp(T/T_{Lasing})$ with $TH_{Lasing}^0 = (5 \pm 1)$ kW/cm² and $T_{Lasing} = (125 \pm 14)$ K, which is a well-known feature of laser systems [5,6]. Thus, CdS NWs exhibit a rather high temperature stability. In contrast, the degradation threshold also exhibits an exponential relation

with $TH_{deg}^0 = (373 \pm 16)$ kW/cm², though with a negative T_{deg} of (-800 ± 100) K. Hence, the damage mechanism is unambiguously a temperature dependent effect.

Consequently, CdS NWs provide a stable nanoscale laser system for various applications and temperatures, as long as the degradation threshold remains considerably larger than the lasing threshold. This is the case in the complete investigated temperature range. The degradation threshold is approximately 75 times larger than the lasing threshold at 4K, whereas this ratio drops to about 5 times at room temperature. Thus, the critical upper temperature limit can be determined as the intersection of both thresholds by extrapolation with a value of $T_{Lasing}^{limit} = (470 \pm 70)$ K, as depicted in figure 2.

In order to raise this critical temperature towards high temperature applications beyond 470 K, either TH_{Lasing}^0 must be decreased or one of both temperature parameters T_{Lasing} or T_{deg} need to be increased. Yet, these parameters are not necessarily independent of each other, but strongly depend on the pumping conditions, NW material, and resonator morphology. However, insights into the origins of the UV light induced material degradation are urgently demanded in order to draw routes towards an adjustment of T_{deg} in CdS NW lasers.

References

- [1] P. Yang, *et al.*, Nano Letters **10**, 1529–1536 (2010).
- [2] J.N. Anker *et al.*, Nat Mater **7**, 442–453 (2008)
- [3] T.P.H. Sidiropoulos *et al.*, Nat Phys **10** 870–876 (2014).
- [4] L. Casperson, J. Appl. Phys. **46**, 5194–5201 (1975).
- [5] M. Wille *et al.*, Nanotechnology **27**, 225702 (2016).
- [6] J. Fallert *et al.*, Phys. Status Solidi C **6**, 449–452 (2009).

Inherently flat metasurfaces enabled by spatially selective ion irradiation

Martin Hafermann, Jura Rensberg, Jad Salman¹, Mikhail Kats¹, Carsten Ronning

¹Department of Electrical and Computer Engineering, University of Wisconsin @ Madison

Optical metamaterials and metasurfaces are an emerging frontier, with promising applications including optical modulation, routing, dynamic beam shaping, and adaptive optics. Although conventional metasurfaces are optically flat, they are not truly planar and thus, do not allow for three-dimensional device fabrication.

Using ion irradiation (defect engineering [1]) or ion implantation (impurity doping) through nanometer-scale masks, the optical properties of various material systems including silicon can be modified spatially resolved. [2-4] With this robust and repeatable technique, we demonstrated several optical devices at infrared frequencies including frequency selective surfaces and Fresnel zone plates (FZP).

Here, we first uniformly implanted silicon (Si) substrates with phosphorus (P) to create an n^+ -doped layer embedded within the substrate (P:Si). Box-like doping profiles extending 550 nm into the Si substrates were achieved by sequential implantation with various ion energies ranging from 30 to 380 keV and suitable ion fluences. Subsequently, all samples were annealed at 900°C in high vacuum ($\sim 10^{-4}$ mbar) for 15 minutes to activate the majority of dopants and to reduce the irradiation damage.

Figure 1 compares the refractive index $n + ik$ as determined by spectroscopic ellipsometry of intrinsic Si and our P:Si samples having doping concentrations c_p ranging from 10^{19} to 10^{21} cm^{-3} . The near-normal reflectance measured by Fourier transform infrared spectroscopy (FTIR) as well as the reflectance calculated from the

measured refractive index is shown for each doping concentration. Intrinsic Si is transparent ($k \sim 0$) in the mid-infrared and only $\sim 25\%$ of the incident light is reflected. The optical properties of P:Si are increasingly dominated by the free-carrier contribution and can be described by the frequency dependent Drude model:

$$\epsilon = \epsilon_\infty \left(1 - \frac{\omega_p^2}{\omega^2 + i\gamma} \right), \quad (1)$$

where ϵ_∞ is the high-frequency permittivity, γ a damping factor, related to energy dissipation, and ω_p the screened plasma frequency, which is proportional to the free-carrier concentration.

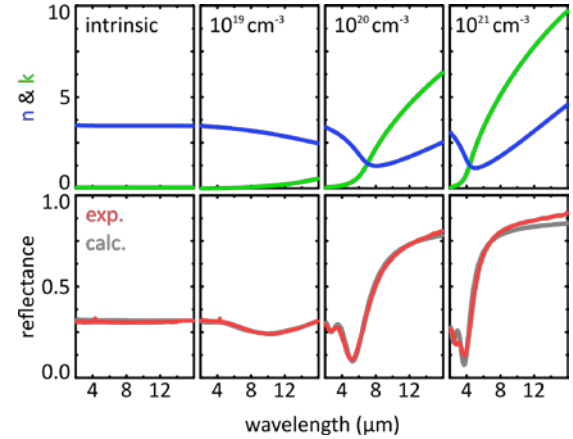


Fig. 1: Refractive index and measured normal reflectance of phosphorous ion implanted silicon for various doping concentrations. The calculated reflectance using the experimental determined refractive index is given for comparison, respectively.

A plasma frequency of $\omega_p \sim 4$ μm , which corresponds to a free-carrier concentration of 2.2×10^{20} cm^{-3} , was found for the sample doped with $c_p = 10^{21}$ cm^{-3} . The reflectance of this sample is as high as 90% for wavelengths larger than ~ 6 μm ,

which indicates “metal-like” (plasmonic) optical properties.

The reflectance contrast of the plasmonic and intrinsic regions is utilized to fabricate diffractive Fresnel zone plates. Unlike a refractive lens, zone plates are flat with alternating rings of transparent and opaque areas spaced in such a manner that a single wavelength of light is focused at a specific focal point (compare figure 2a). The opaque, highly n^+ -doped regions are embedded in the transparent silicon substrate, which are predefined by suitable PMMA masking. Three different FZPs were designed to focus 10.6 μm light at focal lengths of 10, 6, and 2 cm (NA: 0.046, 0.076, and 0.226).

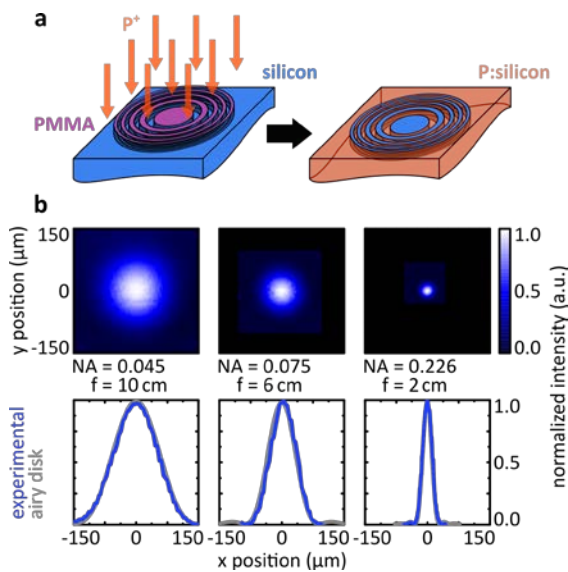


Fig. 2: (a) Area-selective impurity doping using a PMMA mask. Areas, that were covered during implantation remain intrinsic Si, whereas all other regions are highly doped P:Si. (b) Measured intensity distribution of transmitted light through 3 different FZPs (NA: 0.045, 0.075 and 0.226) in the focal plane, respectively. Cross-sections through each intensity distribution are in perfect agreement with airy disk calculation.

Figure 2b shows the normalized intensity plots for the focal point of each FZP. The focal spot size shrinks according to the

increasing NA, which can be also seen in the cross-sectional intensity plots (figure 2b bottom row). Airy function calculations are in perfect agreement with the measured focal spot sizes, indicating diffraction-limited performance of our FZPs. The peak focusing efficiency was found to be 8.5%, determined by integrating the intensity profile of the zone-plate focal spot and normalizing to the integrated intensity through a reference undoped silicon slab with an open aperture of equal size to the zone plates.

By using area-selective ion beam doping and highly n^+ -doped silicon, we were able to fabricate an optical device that is CMOS compatible, completely planar and monolithic, thus stackable, as well as robust against high temperatures and physical erosion. This technique could be also applicable to higher mobility semiconductor materials (III-V semiconductors, germanium, and others) for less loss.[5,6]

References

- [1] J. Rensberg *et al.*, Nano Lett. 16, 1050 (2016).
- [2] G. V. Naik *et al.*, Adv. Mater. 25, 3264 (2013).
- [3] Y. Zhong *et al.*, J. Nanophoton. 9, 093791 (2015).
- [4] M. Shahzad *et al.*, J. Appl. Phys. 110, 123105, (2011).
- [5] S. Law *et al.* Nano Lett. 13, 4569 (2013).
- [6] S. Prucnal *et al.*, Sci. Rep. 6, 27643 (2016).

Discrepancy between integral and local composition in off-stoichiometric $\text{Cu}_2\text{ZnSnSe}_4$ kesterites: A pitfall for classification

Philipp Schöppe, Galina Gurieva¹, Sergio Giraldo², Gema Martínez-Criado^{3,4},
Carsten Ronning, Edgardo Saucedo², Susan Schorr^{1,5}, Claudia S. Schnorr

¹Helmholtz-Zentrum Berlin für Materialien und Energie, Germany

²Catalonia Institute for Energy Research (IREC), Barcelona, Spain

³ESRF – The European Synchrotron, Grenoble, France

⁴Instituto de Ciencia de Materiales de Madrid (CSIC), Spain

⁵Institut für Geologische Wissenschaften, Freie Universität Berlin, Germany

Thin film solar cells based on $\text{Cu}(\text{In,Ga})\text{Se}_2$ have achieved a record efficiency of 22.6 %, thus closing the gap to silicon-based technology [1]. However, their large-scale implementation may be hindered by the availability of the rare element In. So-called kesterites, such as $\text{Cu}_2\text{ZnSnSe}_4$ (CZTSe), present an attractive and promising alternative since all elements are non-toxic, low-cost, and earth-abundant, and efficiencies up to 12.6 % have already been demonstrated [2].

The absorber layers of high-efficiency kesterite-based solar cells are typically grown Cu-poor and Zn-rich, although secondary phases occur easily in non-stoichiometric CZTSe. These secondary phases have detrimental effects on the device performance and are discussed as one of the factors currently limiting the solar cell efficiency. Furthermore, the presence of secondary phases leads to a discrepancy between the integral layer composition and the composition of the actual CZTSe. The latter, however, determines the type and concentration of defects in the material and thus significantly affects its electrical properties. We therefore applied high-resolution X-ray fluorescence (XRF) analysis using a synchrotron nanobeam to study the local composition of a highly non-stoichiometric CZTSe layer on a submicrometer scale [3].

The CZTSe layer was grown by sequential selenization of a metallic precursor deposited on Mo-coated soda lime glass [4]. The integral layer composition was very Zn-rich and extremely Cu-poor with $\text{Zn/Sn} = 1.37$ and $\text{Cu}/(\text{Zn}+\text{Sn}) = 0.55$ compared to the stoichiometric material with $\text{Zn/Sn} = \text{Cu}/(\text{Zn}+\text{Sn}) = 1$. A thin cross section lamella of 270 nm thickness was prepared using a focused ion beam system [5]. Figure 1 presents a scanning electron micrograph (SEM) of the lamella showing the glass substrate, the Mo layer, the CZTSe layer and a Pt protective layer. The scanning transmission electron micrograph (STEM) reveals irregular CZTSe grains of some hundred nanometers in size.

High-resolution XRF studies were performed at ID16B station of the European Synchrotron (ESRF) in Grenoble, France, with a beam energy of 29.34 keV and a spot size of $47 \times 51 \text{ nm}^2$ [6]. The lamella was moved through the beam in 70 nm steps and at each spot a full XRF spectrum was recorded. The resulting XRF intensity maps for Cu, Zn, Sn, and Se are shown in Figure 1. The morphology of the CZTSe layer seen in the SEM image is readily apparent in the XRF maps despite a small drift of the lamella during the measurement.

The Se map displays a homogeneous XRF intensity across the entire CZTSe layer whereas the Cu, Zn, and Sn maps all

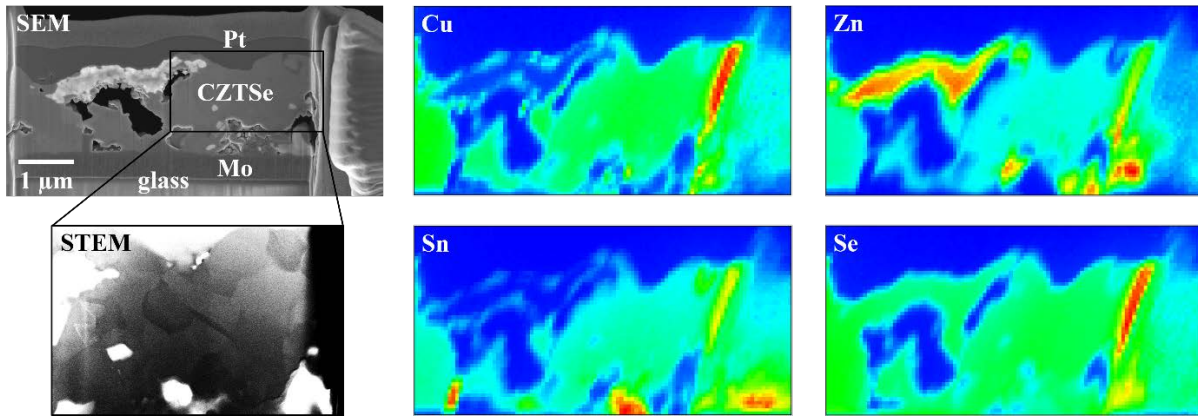


Fig. 1: Scanning electron micrograph (SEM) of the CZTSe cross section lamella together with the X-ray fluorescence maps of Cu, Zn, Sn, and Se. The scanning transmission electron micrograph (STEM) shows the CZTSe grain structure.

exhibit pronounced intensity variations. In some regions, an increased intensity for one of the cations corresponds to an almost complete absence of the other two cations. This clearly indicates the presence of binary secondary phases. In fact, ZnSe-like, SnSe/SnSe₂-like, and even CuSe/Cu₂Se-like secondary phases all coexist within an area of only a few micrometers in size. For this lamella, ZnSe-like phases are found mostly at the top of the layer while the SnSe/SnSe₂-like phases are located close to the CZTSe/Mo interface. This is most likely caused by the initial precursor configuration (glass/Mo/Cu/Sn/Cu/Zn) and reflects the reaction kinetics during the selenization process [4].

The regions in the XRF maps where all four elements are present correspond to the actual CZTSe domains. The local compositions of these domains were determined by fitting the individual XRF spectra using the software PyMCA [3]. The Zn/Sn ratio varies between 1.5 and 2.2 while the Cu/(Zn+Sn) ratio ranges from 0.9 to 1.1. The local CZTSe compositions are thus extremely Zn-rich and Sn-poor but almost Cu-neutral in striking contrast to the integral layer composition. The latter would suggest the presence of Cu vacancies and

Zn_{Cu} antisites, leading to shallow donor and acceptor levels. The local CZTSe compositions, however, suggest the presence of Cu_{Sn} and Zn_{Sn} antisites together with Cu and Zn interstitials, leading to shallow donor and acceptor levels but also to several defect levels deep inside the energy gap [3]. Anticipating the kinds of defects present in the CZTSe based on the integral layer composition can thus lead to false conclusions about the material properties. As a consequence, the integral layer composition is not a reliable measure for the characterization of highly non-stoichiometric CZTSe and care has to be taken when relating it to other material properties including the device performance.

References

- [1] P. Jackson *et al.*, Phys. Stat. Sol. RRL **10**, 583 (2016).
- [2] W. Wang *et al.*, Adv. Energy Mater. **4**, 301465 (2014).
- [3] Ph. Schöppe *et al.*, Appl. Phys. Lett. **110**, 043901 (2017).
- [4] S. Giraldo *et al.*, Adv. Energy Mater. **5**, 1501070 (2015).
- [5] Ph. Schöppe *et al.*, Appl. Phys. Lett. **106**, 013909 (2015).
- [6] G. Martínez-Criado *et al.*, J. Synchrotron Rad. **23**, 344 (2016).

Bond strength inversion in (In,Ga)As

Stefanie Eckner, Konrad Ritter, Philipp Schöppe, Erik Haubold, Erich Eckner,
Mark C. Ridgway*, Claudia S. Schnorr

*Department of Electronic Materials Engineering, The Australian National University,
Canberra ACT 0200, Australia

Random semiconductor alloys like (In,Ga)As offer huge possibilities for application in electronic and optoelectronic devices. Despite their technological importance, there still remain some open questions regarding the fundamental properties of mixed III-V semiconductors. One of those regards the force constants of the different types of bonds present in the material.

In structure simulations of semiconductor alloys it is often assumed that the bond stretching force constants of the binary parent materials are directly transferable to the ternary system [1]. However, a theoretical study of (In,Ga)P predicts a drastic change [2], making the experimental determination of the force constants in III-V semiconductor alloys imperative.

While the force constants of binary zincblende materials are accessible via macroscopic elastic constants, this approach fails for mixed systems. In contrast, temperature dependent x-ray absorption fine structure spectroscopy (EXAFS) offers the opportunity to determine the element-specific bond stretching force constants even in random alloys.

Here we studied (In,Ga)As using temperature dependent EXAFS to gain insight into the vibrational behaviour of semiconductor alloys. (In,Ga)As thin films with three different compositions were grown on InP using metal organic chemical vapour deposition. The substrate was selectively etched and the thin film material was ground, diluted with graphite and pressed

into pellets suitable for EXAFS measurements in fluorescence mode. Temperature dependent EXAFS measurements of the Ga-K- and In-K-edge (10367 eV and 27940 eV, respectively) were carried out at the SuperXAS Beamline at SLS, Villigen, Switzerland in the temperature range from 35 K to 300 K in fluorescence mode. Data analysis was done using the LARCH software package [3] with theoretical scattering amplitudes and phase shifts calculated with the FEFF9 code [4].

The first nearest neighbour distance distribution was modelled with the bond length R (mean), the variance σ^2 (width), and the third cumulant C_3 (skew) and subsequently fitted to the spectra. To account for the temperature dependence of the variance and the third cumulant, the correlated Einstein model [5] was used,

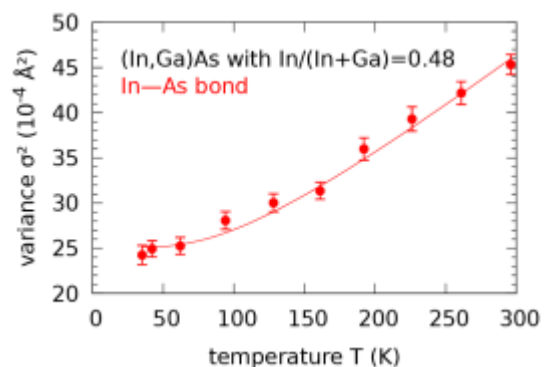


Fig. 1: Variance of the In-As first nearest neighbour distance distribution as a function of temperature for (In,Ga)As with $\text{In}/(\text{In}+\text{Ga})=0.48$. The solid line is a fit of the correlated Einstein model.

correlated Einstein model [5] was used, yielding the bond stretching force constant k . In Fig. 1 the variances σ^2 determined in separate fits for each temperature are shown

for the In-As bonds in (In,Ga)As with composition $\text{In}/(\text{In}+\text{Ga})=0.48$. The values are well described by the correlated Einstein model fitted to the whole dataset.

The resulting element-specific Ga-As and In-As bond stretching force constants k are plotted in Fig. 2 as a function of composition. The binary values are in good agreement with previous EXAFS studies [6] and the empirical law for III-V semiconductors correlating the force constants with the bond lengths [7].

For the ternary materials a striking inversion of the bond strengths respective to the binary materials is visible. The Ga-As bond in GaAs is significantly stiffer than the In-As bond in InAs, as expressed by the larger bond stretching force constant. In the ternary alloys, in contrast, the Ga-As bonds are softer than the In-As bonds. This remarkable behaviour, which was predicted in theoretical calculations for (In,Ga)P [2], was now confirmed experimentally for the very first time.

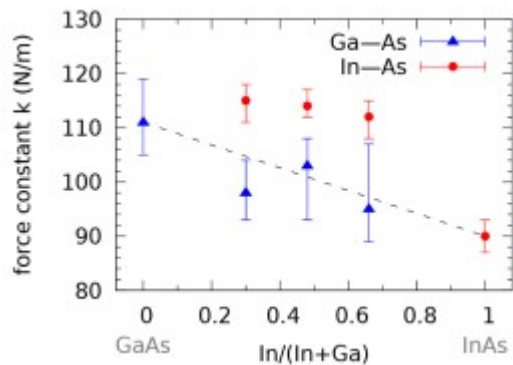


Fig. 2: Element-specific bond stretching force constants of the Ga-As and In-As bonds of (In,Ga)As as a function of composition.

In (In,Ga)As, the element-specific bond lengths show a slight increase with increasing In content [1,8]. Adopting the empirical law valid for binary III-V semiconductors [7], this would give rise to a decrease of the bond stretching force

constants with increasing In content. The resulting change amounts to approximately 2% comparing the binary materials to the $\text{In}/(\text{In}+\text{Ga})=0.48$ compound. The observed drastic inversion thus cannot be explained by this simple model. Therefore, the influence of the surrounding matrix, which changes with varying composition, must be taken into account to properly describe atomic vibrations in III-V semiconductor alloys.

In conclusion, the element-specific bond stretching force constants in (In,Ga)As show a nontrivial composition dependence. Consequently, the force constants used in simulations and modelling of material properties of random semiconductor alloys should not be directly adopted from the binary parent materials.

References

- [1] C.S. Schnohr, Appl. Phys. Rev. **2**, 031304 (2015).
- [2] K. Biswas *et al.*, Phys. Rev. B **78**, 085212 (2008).
- [3] M. Newville, <http://cars.uchicago.edu/xraylarch>.
- [4] J.J. Rehr *et al.*, Phys. Chem. Chem. Phys. **12**, 5503 (2010).
- [5] T. Yokoyama, J. Synchr. Rad. **6**, 323 (1999).
- [6] S.I. Ahmed *et al.*, J. Chem. Phys. **139**, 164512 (2013).
- [7] A.S. Verma, Phys. Lett. A **372**, 7196 (2008).
- [8] J.C. Mikkelsen, Jr. and J.B. Boyce, Phys. Rev. Lett. **49** (1982).

Secondary phases in $\text{Cu}_2\text{ZnSnSe}_4$ studied by X-ray absorption spectroscopy

Konrad Ritter, Laura Elisa Valle Rios¹, Galina Gurieva¹, Sergio Giraldo², Stefanie Eckner, Götz Schuck¹, Daniel Töbrens¹, Edgardo Saucedo², Susan Schorr^{1,3}, Claudia Schnorr

¹Helmholtz-Zentrum Berlin für Materialien und Energie, Germany

²Catalonia Institute for Energy Research (IREC), Barcelona, Spain

³Institut für Geologische Wissenschaften, Freie Universität Berlin, Germany

So-called kesterites, like $\text{Cu}_2\text{ZnSnSe}_4$ and related compounds and alloys, offer a wide range of promising absorber materials for high efficiency thin film solar cells. Although theoretical calculations suggest that the conversion efficiency could reach values well beyond the 20% mark, the record efficiency achieved up to now with these materials is only 12.6% [1]. One of the main factors currently limiting the device performance seems to be the formation of several binary and ternary secondary phases in nonstoichiometric kesterite materials.

The presence of these secondary phases has been studied by X-ray diffraction (XRD) and Raman spectroscopy. However, both techniques can typically detect only certain possible secondary phases and often special experimental conditions are required [2]. Furthermore, the extent to which the amount of secondary phases can be quantified is still being discussed [3]. X-ray absorption near edge structure (XANES) spectroscopy represents a third independent technique for studying the phase content of kesterite materials and offers a high potential for quantification [4,5]. Therefore, we have applied XANES spectroscopy to study the presence of secondary phases in nonstoichiometric $\text{Cu}_2\text{ZnSnSe}_4$.

Powder samples synthesized by solid state reaction [6] and thin films from different stages of a sequential selenization process [7] were investigated at the KMC-2 beamline at BESSY in Berlin. Potential

secondary phases for these nonstoichiometric $\text{Cu}_2\text{ZnSnSe}_4$ samples include Cu_2Se , CuSe , ZnSe , SnSe , SnSe_2 , and Cu_2SnSe_3 . X-ray absorption spectra of all materials were measured from -200 eV to +400 eV around the Cu and Se K-edges (8979 and 12658 eV, respectively) at room temperature in transmission or fluorescence mode. A reference was measured simultaneously for each scan to enable a precise alignment of the energy scales.

Data analysis is based on linear combination fitting (LCF) as implemented in the program ATHENA, which is part of the DEMETER software package [8]. ATHENA can fit a given X-ray absorption spectrum as a linear combination of other spectra measured at the same absorption edge. The XANES region of the spectra is strongly affected by the valence state of the absorbing element, the chemical nature of the neighboring atoms, and the crystal structure. Therefore, the pure kesterite phase and the different secondary phases yield distinctly different XANES spectra. The spectra of stoichiometric $\text{Cu}_2\text{ZnSnSe}_4$, Cu_2Se , and CuSe measured at the Cu K-edge are displayed in Fig. 1. One can clearly see the differences both in edge position and fine structure. The spectrum of the ternary Cu_2SnSe_3 standard is nearly identical to the $\text{Cu}_2\text{ZnSnSe}_4$ spectrum and can therefore not be distinguished from it in the LCF analysis. Since prior XRD measurements suggest that the ternary phase is not present in the given samples [6], we only used the two

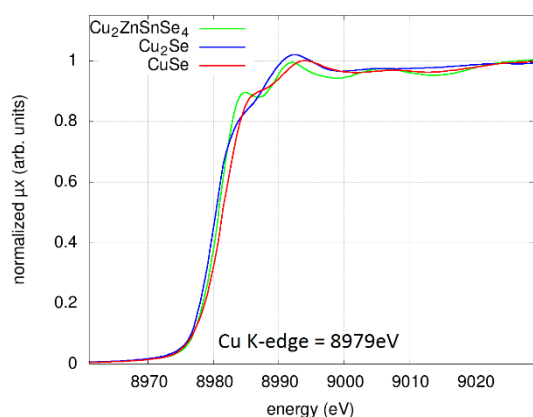


Fig. 1: Normalized XANES spectra of different standards measured at the Cu K-edge.

binary standards and the stoichiometric kesterite for the LCF analysis.

Fitting an unknown sample yields the weight for each of the phases together with a measure for the quality of the fit given by the χ^2 and R values. The region of the fit is chosen from -20 eV to +50 eV around the Cu K-edge. Figure 2 plots the measured spectrum for a nonstoichiometric powder sample (data) together with the weighted spectra of the stoichiometric $\text{Cu}_2\text{ZnSnSe}_4$, Cu_2Se , and CuSe as well as their sum (fit). In this particular case, the sample spectrum is represented by 57% $\text{Cu}_2\text{ZnSnSe}_4$ kesterite, 35% CuSe , and 8% Cu_2Se . The residual (difference between fit and data) is also shown on an enlarged scale (right axis). As one can see in Fig. 2, the residual is well below 0.01 over the entire region of the fit. The same is true for all other nonstoichiometric samples in this study, which shows that we indeed used a complete set of standards.

The LCF analysis of the Cu K-edge XANES reproduced many qualitative findings previously obtained for this sample set. For example, both XRD and XANES indicate that four of the nonstoichiometric powders studied do not contain any Cu

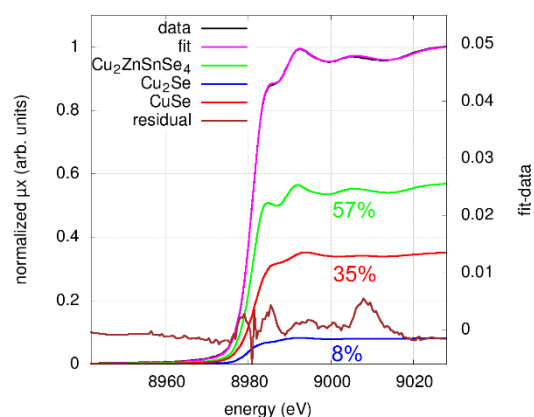


Fig. 2: Normalized XANES spectrum of a nonstoichiometric $\text{Cu}_2\text{ZnSnSe}_4$ sample together with the LCF analysis (left axis). The residual is plotted on the right axis.

secondary phases [6]. For the Cu K-edge, XANES thus provides an alternative way to determine the nature and amount of secondary phases in nonstoichiometric $\text{Cu}_2\text{ZnSnSe}_4$. A similar analysis of the data taken at the Se K-edge will reveal the presence of ZnSe , SnSe , or SnSe_2 and will provide an estimate of the quantification possible with this technique.

References

- [1] W. Wang *et al.*, *Adv. Energy Mater.* **4**, 1301465 (2014).
- [2] D. M. Berg *et al.*, *Thin Solid Films* **569**, 113 (2014).
- [3] A. de Sousa, *Investigation of detection limits of ZnSe and $\text{Cu}_2\text{ZnSnSe}_3$ secondary phases in $\text{Cu}_2\text{ZnSnSe}_4$* , Master thesis, Helmholtz-Zentrum Berlin für Materialien und Energie, <http://hdl.handle.net/10316/31589> (2016).
- [4] J. Just *et al.*, *Phys. Chem. Chem. Phys.* **18**, 15988 (2016).
- [5] J. Just *et al.*, *J. Alloys Compd.* **670**, 289-296 (2016).
- [6] L. E. Valle Rios *et al.*, *J. Alloys Compd.* **657**, 408-413 (2016).
- [7] S. Giraldo *et al.*, *Adv. Energy Mater.* **5**, 1501070 (2015).
- [8] B. Ravel and M. Newville, *J. Synchrotron Rad.* **12**, 537-541 (2005).

Ultra-low temperature chemistry of ($^3\text{C}_0$) atoms

Serge A. Krasnokutski, Cornelia Jäger, Friedrich Huisken, Martin Kuhn,¹ Alexander Kaiser,¹ Andreas Mauracher,¹ Michael Renzler,¹ Diethard K. Bohme,² Paul Scheier,¹ and Thomas Henning³

¹Institut für Ionenphysik und Angewandte Physik, Universität Innsbruck, Technikerstr. 25, A-6020 Innsbruck, Austria

²York University, 4700 Keele Street, Toronto M3J 1P3, Ontario, Canada

³Max-Planck-Institut für Astronomie, Königstuhl 17, 69117 Heidelberg, Germany

We performed laboratory experiments designed to explore encounters of fullerenes and dihydrogen with C atoms produced by a clean source of C atoms. Such encounters occur in astro-physical environments such as the interstellar medium (ISM) where C_{60} and hydrogen are abundant species. There has been a recent breakthrough in C atom production.¹ Low-energy carbon atoms can be produced with a purity >99% from a thin-walled, sealed tantalum tube containing carbon. We have used this source to investigate the reactivity of abundant astrophysical molecules toward C atoms in very low-temperature He droplets. C_{60} or H_2 molecules are added into He droplets (ca. 10^6 He atoms) where they can aggregate and be cooled to the droplet temperature of 0.37 K. Carbon atoms are then added and allowed to react with the molecular aggregates before the droplets are exposed to ionizing or attaching electrons that permit reactants and products to be analyzed with a mass spectrometer. The low-temperature reaction $\text{C} + \text{H}_2 + \text{M} \rightarrow \text{HCH} + \text{M}$ was found to be barrierless. Therefore, the reaction $\text{C} + \text{H}_2 \rightarrow \text{CH} + \text{H}$ and the reverse one $\text{CH} + \text{H} \rightarrow \text{C} + \text{H}_2$ are predicted to have no energy barrier. Practically all hydrocarbon cations C_mH_n^+ with $m = 1-4$ and $n = 1-15$ are produced. The ion intensities on the masses of hydrocarbon products are summarized in Figure 1. The ionization process introduce

large amount of energy to the formed cations. Therefore, the mass spectrometry is nicely suited for testing the stability of

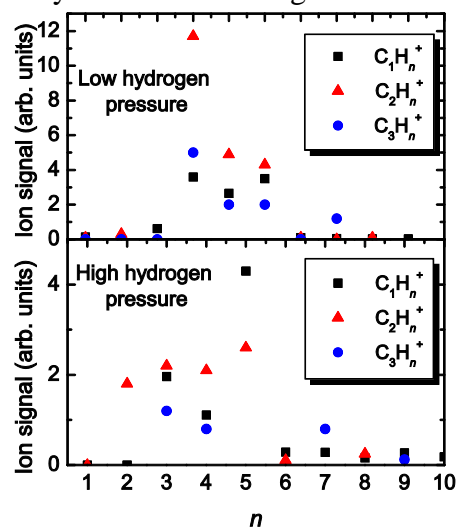


Fig. 1: Ion signals on the masses corresponding to the products of chemical reactions between carbon atoms and dihydrogen molecules.

cations. The “magic” peak in the mass spectra reveal the most stable cations, which are also expected to be abundant in the ISM. At low dihydrogen doping, the most intense “magic” peaks are caused by the C_2H_3 cation. In the case of the low C/H ratio, the ion-molecule reactions followed by electron impact ionization lead to the dominant formation of CH_5^+ . This implies the high abundance of this cation in the ISM.²

For the reaction of C_{60} , addition of up to at least six single C atoms was observed.³ The carbene character of bridge-type $\text{C}_{60}(\text{C})_n$ is clearly manifested by the

performed natural bond orbital analysis. The carbene character can be also inferred for all C adducts $C_{60}(C)_n$ from the observed water impurity adduct $C_{60}C_n(H_2O)_n^\pm$ ion peaks. According to the presence of these peaks, $C_{60}(C)_n$ molecules with $n > 0$ pick-up H_2O , as would be expected from a carbene reaction, presumably by H–OH bond insertion, while C_{60} itself adds H_2O only by physisorption. Furthermore, the results of our separate experiments with added H_2 dopant (Figure 2) indicate H_2 additions for each $C_{60}(C)_n$ with $n = 1, 2, 3, 4, 5$, presumably by H–H bond insertion. These results with H_2O and H_2 indicate sequential surface addition of at least the first five carbon atoms to form carbenes of the type $C_{60}(C)_n$ with $n=1-5$ instead of energetically favorable C chains such as $C_{60}=C=C=C=C$., for which always only one H_2O or H_2 would add chemically.

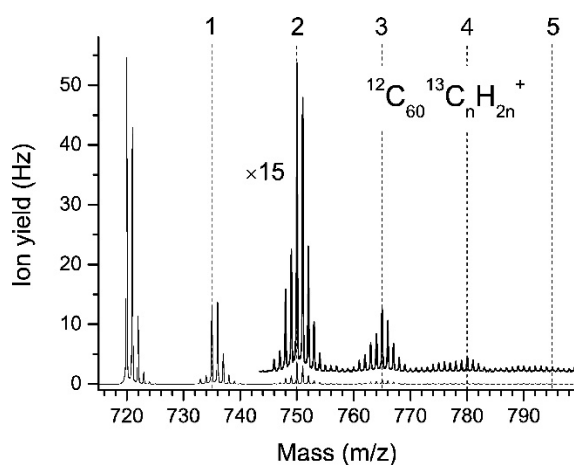


Fig. 2: Mass spectra recorded for $^{12}C_{60}$ $^{13}C_nH_n^+$ ions for droplets containing C_{60} , ^{13}C , and H_2 .

This result shows that C-atom additions can transform the chemically inert C_{60} into reactive carbenes $C_{60}(C)_n$. Carbenes are known from terrestrial chemistry to be among the most versatile and synthetically useful reactive intermediates. Carbenes should also play a role in interstellar chemistry. Our experiments demonstrate

the reactivity of $C_{60}(C)_n$ toward H_2 and H_2O . We expect similar reactivities toward many other molecules as well as other carbenes such as $:CO$, $:CS$, $:C_n$., $:C_nO$, and $:CNH$. Our other recorded mass spectra show evidence of the presence of C adduct ions for clusters of fullerenes of the type $(C_{60})_n(C)_m^\pm$ with $n = 1$ to 9 and $m = 1-5$ including the dumbbell. The extremely high stability of the bridged dumbbell structure $C_{60}=C=C_{60}$ was observed.

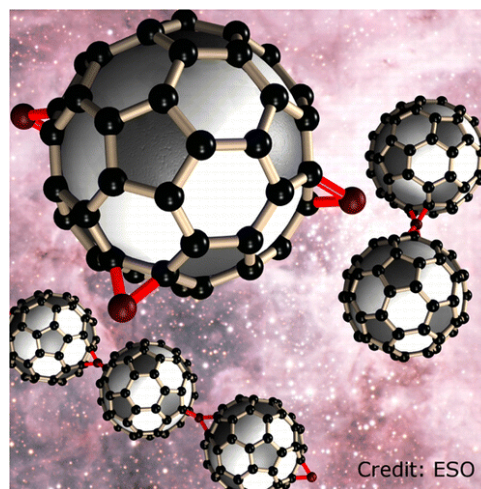


Fig. 3: Possible molecular structures of the products of chemical reactions between C_{60} molecules and C atoms, which are expected to be formed in the ISM.

The observed surface C additions at low temperature enhance the chemical activity of the surface of C_{60} by carbene formation. The latter may pave the way toward a generation of a new class of fullerene derivatives. Reactive C_{60} carbene species is expected to be formed in the ISM, where they could polymerize forming long fullerene chains in the way shown in Figure 3.

References

- [1] S. A. Krasnokutski *et al.*, Appl. Phys. Lett. **105**, 113506 (2014) .
- [2] S. A. Krasnokutski *et al.*, Astrophys. J. Lett. **818**, L31 (2016).
- [3] S. A. Krasnokutski *et al.*, J. Phys. Chem. Lett. **7**, 1440 (2016).

Cosmic dust analogues – Simultaneous formation of silicate and carbon condensates at cryogenic temperatures

Gaël Rouillé, Cornelia Jäger, and Thomas Henning¹

¹ Max-Planck-Institut für Astronomie, Königstuhl 17, 69117 Heidelberg, Germany

Cosmic dust is mainly released by stars at a late stage of their evolution and it is destroyed in the interstellar medium (ISM) by various mechanisms such as sputtering and grain-grain shattering in supernova-induced shock waves. The production rate of dust grains by stars, however, is not as fast as the total rate of their destruction [1]. In order to explain the amount of interstellar dust that is observed, one has proposed that it could also be formed in the ISM through the accretion and chemisorption of gas-phase atoms and molecules onto seed particles. This would take place at the temperatures of the ISM, which range from 10 to 100 K.

Interstellar dust grains are mostly made either of carbon or of silicates. As we had confirmed that silicates could be formed at cryogenic temperatures [2], we started an experimental study of their condensation in the presence of carbon atoms and small molecules. Our motivation arises from the fact that C atoms, and to some extent C_n molecules, are abundant in the ISM and are a priori present as silicate matter grows there. Our goal is to verify that the presence of carbon does not interfere with and does not prevent the formation of silicates.

We have carried out experiments on the condensation at cryogenic temperatures of mixtures of carbon atoms and molecules (C_n) and species related to the composition of silicates (atoms: Mg and Fe; molecules: SiO, SiO₂, FeO, etc.). These atoms and molecules are produced under vacuum by the simultaneous laser vaporization of two

targets, one consisting of graphite and the other of an amorphous material selected among SiO, Mg₂SiO₄, Mg_{0.4}Fe_{0.6}SiO₃, and Mg_{0.6}Fe_{0.4}SiO₃. The gas-phase species produced by laser vaporization are deposited on a substrate of KBr kept at 6.5 K, together with Ne atoms in excess so as to produce doped neon-ice matrices. Depending on the composition of the Si-containing target, the presence in the Ne matrices of isolated Mg and Fe atoms, of isolated C₂, C₃, C₆, and SiO molecules, is verified by UV/vis spectroscopy (Fig. 1). More Ne-matrix-isolated species are detected using Fourier-transform IR (FTIR) spectroscopy, including H₂O from the background gas in the vacuum system (Fig. 2).

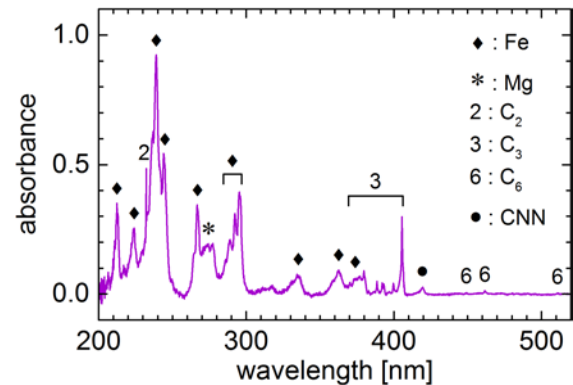


Fig. 1: Absorption spectrum of atoms and molecules isolated in Ne ice at 6.5 K following the laser vaporization of synthetic amorphous Mg_{0.6}Fe_{0.4}SiO₃ and graphite. CNN results from the reaction of C atoms with background N₂.

Once a doped matrix is thick enough to enable spectroscopic measurements, its temperature is increased by steps in order to allow the diffusion of the dopants in the

Ne ice and the slow sublimation of the said ice. During this annealing procedure, FTIR spectra are measured to monitor the composition of the material on the substrate (Fig. 2). By the time the Ne ice has completely disappeared, near 12 K, so have the bands of isolated molecules. On the other hand, broad features signaling solid matter have risen. Indeed, in addition to the bands of H₂O, CO, and CO₂ ices, bands typical of silicates have grown at about 500 and 1000 cm⁻¹. These bands are clearly seen at room temperature after the ices have disappeared. It is interesting to note that the FTIR spectra do not show the presence of solid SiC. On the other hand, the two bands near 1400 and 1600 cm⁻¹ could be attributed to carbonates and the C=C stretching band in aromatic carbon structures. Carbonate bands are also observed in meteorites and interstellar dust particles [3].

The condensates have been examined using high-resolution transmission electron microscopy (HRTEM) to determine their morphology and the structure of the material they are composed of. Their elemental composition has been evaluated by energy dispersive X-ray (EDX) spectroscopy. Briefly, the condensates consist of micrometer-sized fluffy aggregates of partially fused amorphous nanoparticles. Actually it appears that two main amorphous materials coexist side by side, one composed of carbon, sometimes revealed by graphitic structures, the other being a silicate.

We conclude that the presence of carbon in the quantities of our experiments do not prevent the formation of amorphous silicate matter at cryogenic temperatures. The experiments also show the formation of a separate phase of solid, amorphous carbon under the same conditions. These

results represent the first insight into the separation observed between ISM-grown carbon and silicate matters.

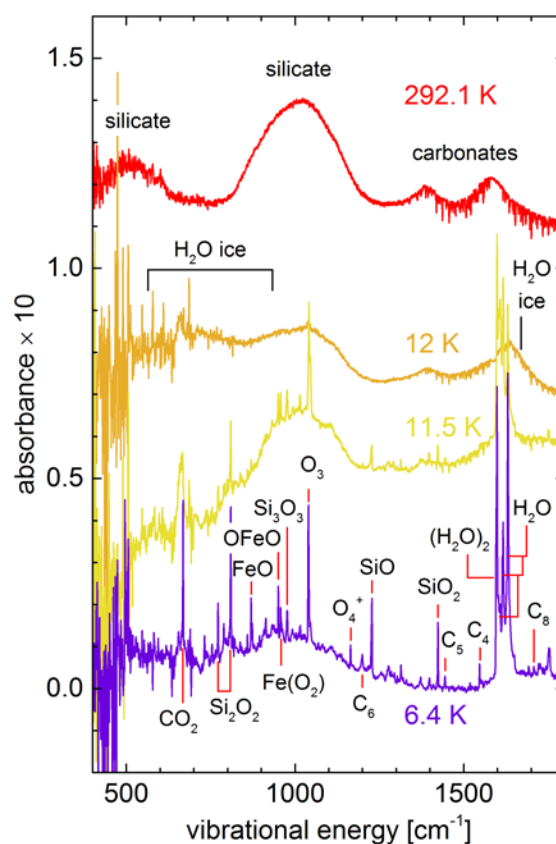


Fig. 2: Absorption spectra showing molecules isolated in Ne ice at 6.4 K following the laser vaporization of synthetic amorphous $Mg_{0.4}Fe_{0.6}SiO_3$ and graphite, and the slow heating of the doped ice that causes the disappearance of the isolated molecules, the sublimation of Ne, and the rise of the silicate features at 500 and 1000 cm⁻¹.

References

- [1] B.T. Draine, in *Cosmic Dust – Near and Far*, ASP Conf. Ser. **414**, 453-472 (2009).
- [2] G. Rouillé *et al.*, *Faraday Discuss.* **168**, 449-460 (2014).
- [3] S.A. Sandford, *Science* **231**, 1540-1541 (1986).

Investigation of LiNbO₃ by combined RBS and NRA in channelling configuration

E. Schmidt, K. Ritter, K. Gärtner, E. Wendler

Defect formation in materials by ion irradiation has found an excellent application in the production of structures in lithium niobate (LiNbO₃) by IBEE. LiNbO₃ has outstanding optical properties, which make it a suitable substrate for optical devices. The exact nature of defect formation is a prerequisite for the successful application of ion beam techniques [1].

A technique that was extensively used in the past for the investigation of ion beam induced defect formation in several materials of different types including LiNbO₃ is Rutherford backscattering spectrometry in channelling configuration RBS/C [2-4].

Several investigations have shown the complex behaviour of investigations of defects in LiNbO₃ by RBS/C. The same amount of ions irradiated to differently oriented LiNbO₃ samples have shown significantly different defect concentrations in RBS/C [2,3]. It could be shown in a recent work that the dependence of RBS/C measurements on the chosen crystallographic axis is attributed to the complex defect structure in LiNbO₃ [4]. To investigate the exact structure of such defects a new approach was applied in this work. Usual RBS/C investigations are limited to the backscattered ions that have interacted with the heaviest element within a compound material such as niobium in LiNbO₃. In this work we have investigated possibilities of using nuclear reaction analysis in channelling configuration (NRA/C) to investigate the defects that are visible by the interaction of ions with lithium and potentially combine this

information with the results of RBS/C investigations that are mainly sensitive to niobium to clarify the atomic structure of ion beam induced defects in LiNbO₃.

Congruent LiNbO₃ samples with the crystallographic X- and Z-axis perpendicular to the surface (denoted as X- and Z-cut) were implanted with 1 MeV iodine ions. The implanted ion fluences were chosen in a range from $2 \times 10^{13} \text{ cm}^{-2}$ to $1 \times 10^{14} \text{ cm}^{-2}$, covering a state of relatively moderate defect concentration for the lowest ion fluence up to the full amorphisation of a 200 nm thick layer on the surface of the material for the highest ion fluence.

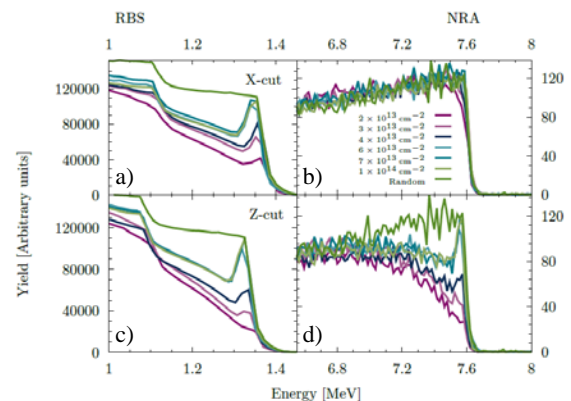


Fig. 1: Backscattering spectra over detector energy measured with 1.4 MeV protons on X- and Z-cut LiNbO₃ in channelling and random configuration for different implanted fluencies of 1 MeV iodine ions. The spectra were separated parts of low detector energies (left side) and high detector energies (right side)

The samples were afterwards investigated with 1.4 MeV protons. The resulting spectra are shown in Fig.1. The spectra were separated in a high energy part (Fig. 1b and 1d) that shows the alpha particles produced by the nuclear reaction $p(^7\text{Li},\alpha)\alpha$. This part of the spectrum

therefore can be attributed purely to the lithium content of LiNbO_3 . The low energy part (Fig. 1a and 1c) of the spectrum is caused by protons backscattered from niobium and oxygen.

It is visible that the NRA/C-signal is four magnitudes lower compared to the RBS/C-signal. This is caused by the significantly lowered reaction cross-section and leads to rather high integration times during the measurements.

The part of the spectrum measured at low detector energies is dominated by the elastic backscattering of protons on Nb. The signal shows a similar distribution as the one measured for similar samples of LiNbO_3 with He ions in channelling configuration[3]. For increasing fluences of iodine ions the yield of protons scattered on the region near the surface increases until it reaches a value comparable to the niveau of randomly oriented material. This indicates an increasing defect concentration until a fully amorphised layer is formed on the surface. A comparable behaviour is visible for the signal of high energetic alpha particles in Z-cut LiNbO_3 (Fig 1d). For the lowest fluences of iodine ions the measured signal is low while it increases in the region near the surface until a niveau of the random orientation is reached. The NRA/C-signal of X-cut LiNbO_3 does not show a significant channelling behaviour in general. Therefore it is rather difficult to see an influence of crystalline defects in this orientation.

To get an insight on the fluence dependence of the measured channelling signal, all spectra were investigated by the DICADA-software to extract defect-concentrations[5]. The mean defect-concentration within the first 200nm was taken as a reference to compare the results of NRA/C and RBS/C measured with

protons in this study to previous results measured with He-ions in RBS/C configuration. The results are shown in Fig. 2.

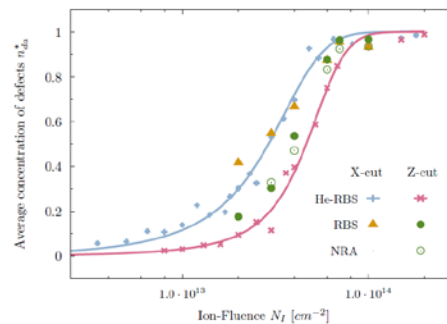


Fig.2: Comparison of the concentration of defects determined by a DICADA-calculation and the average of a 200 nm thick layer on the surface.

It can be seen that the distribution of RBS/C and NRA/C measurements in Z-cut LiNbO_3 are similar to that of previously measured He-RBS/C. Furthermore, regarding the niobium lattice, the same difference between X- and Z-cut LiNbO_3 is observed with RBS/C as in previous investigations with He ions.

Our results suggest that the defects seen in the lithium lattice of LiNbO_3 are comparable in their sensitivity to channelling investigations and their distribution over implanted ion fluence to the defects seen in the niobium lattice with regular RBS/C measurements.

References

- [1] F. Schrempel *et al.*, Nucl. Instrum. Meth. B **250**, 164-168 (2006).
- [2] H. Karge *et al.*, Nucl. Instr. Methods **182**, 777 (1981).
- [3] E. Schmidt *et al.*, J. Phys. D Appl. Phys. **47**, 265302 (2014).
- [4] E. Wendler *et al.*, Nucl. Instrum. Meth. B **379**, 195-199 (2016).
- [5] K. Gärtner, Nucl. Instrum. Meth. B **227**, 522-530 (2005).

Ion beam modification of single crystalline BiVO₄

Elke Wendler, Marie Bischoff, Emanuel Schmidt, F. Schrempel¹,
Klaus Ellmer², Michael Kanis², Roel van de Krol²

¹Institut für Angewandte Physik, Friedrich-Schiller-Universität Jena, Jena, Germany

²Institut Solare Brennstoffe, Helmholtz-Zentrum Berlin, Berlin, Germany

The compound BiVO₄ proved to be a suitable photoanode in devices for solar photo-catalytic water splitting [1]. Using a tandem-water splitting cell with a BiVO₄ photoanode, an efficiency factor of 9% is reached [2]. However, further research is needed for increasing of the efficiency factor. Herein the electrical properties of the electrodes such as resistivity and doping are important because they affect the efficiency of the necessary charge carrier separation [3]. As ion implantation is a common technique for doping but inherently connected with radiation damage, first ion implantation experiments on single crystalline BiVO₄ were carried out.

The single crystal of BiVO₄ used in our experiments was grown by the conventional Czochralski technique with RF induction heating and automatic control of the crystal diameter (for details see [4]).

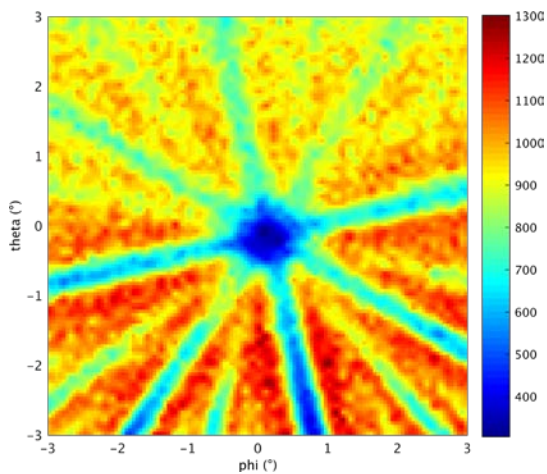


Fig. 1: Angular chart of yield of 2.2 MeV He ions backscattered on Bi atoms, integrated over the first 110 nm.

For studying quality and surface orientation of the BiVO₄ single crystal, angular resolved (ar) RBS (Rutherford backscattering spectrometry) was applied. Spectra were measured for angular ranges of $\pm 3^\circ$ from the axial position for both angles (θ and φ) with step widths of 0.1° . The angular chart depicted in Fig. 1 is obtained by plotting the Bi yield integrated over the first 110 nm as a function of the two tilt angles. Blue areas stand for low yields of backscattered ions due to entrance of ions into the crystal along axis and planes. By comparing the planes and the angles between them with that for the monoclinic scheelite structure of BiVO₄ it can be concluded that the axis perpendicular to the surface is in [001] direction [4].

The loss in contrast in the upper part of the chart (measured last) can be attributed to damage formation in the BiVO₄ crystal by the analysing He ions during the analysis. Because in the corresponding depth the He ions lose their energy mainly by electronic energy loss, this observation indicates that BiVO₄ is rather susceptible to the electronic energy loss of the analysing He ions.

Part of the BiVO₄ crystal was implanted with 200 keV Ar ions to various ion fluences between 6×10^{12} and 2×10^{14} cm⁻² in the two-beam chamber at the Institut für Festkörperphysik in Jena [5] with all experiments being done at room temperature. Each implantation step was followed by subsequent damage analysis with channelling RBS using 1.8 MeV He

ions and a backscattering angle of 170° . The depth distribution of displaced Bi atoms was determined from the channelling spectra and is shown in Fig. 2 (for details see [4]). The depth distribution of damage is compared with that of the primary electronic energy deposition calculated with SRIM (version 2008.04) [6].

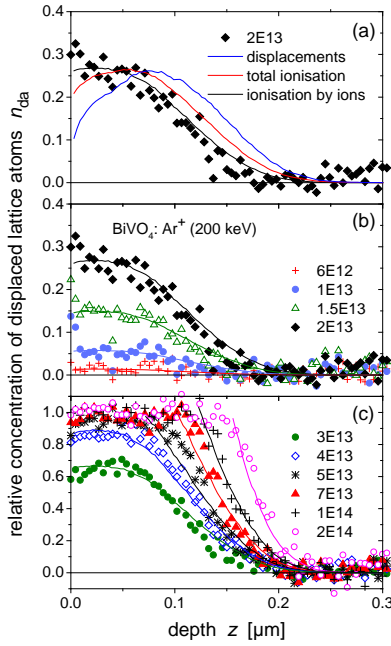


Fig. 2: Relative concentration of displaced lattice atoms, n_{da} , versus depth z (damage profiles) for 200 keV Ar ion implanted BiVO_4 . The ion fluences are given in cm^{-2} . In part (a) the distribution of primary displacements, energy deposited in total ionisations and the energy deposited into ionisations by the implanted ions are plotted in arbitrary units for comparison. The solid lines in parts (b) and (c) are damage distributions calculated with Eq. (1) assuming damage formation by the electronic energy loss of the implanted ions (ionisation by ions, for details see the text).

For the chosen implantation conditions, one would usually expect that damage formation is triggered by the energy deposition in nuclear collision processes. However, from Fig. 2 it is obvious that best agreement with the measured damage profile occurs with the distribution of the electronic energy loss of the implanted ions (see Fig. 2 (a)). The measured damage

profiles are represented by the electronic energy loss of the implanted ions (per ion and unit depth), $S_e^{\text{ions}}(z)$, according to

$$n_{da}(z, N_1) = \frac{S_e^{\text{ions}}(z) N_1}{N_0 E_{da}} \quad (1)$$

with N_1 being the ion fluence and N_0 the atomic density of BiVO_4 . E_{da} is the energy which needs to be deposited for producing one displaced lattice atom as seen by RBS. The curves in Figs. 2 (b) and (c) are calculated using Eq. (1) with E_{da} being adjusted to fit the measured damage distributions. For the lowest ion fluences applied, the value is very high (33 eV/atom) and decreases with increasing ion fluence (Fig. 2 (b)) until it saturates at a value of 3.4 eV/atom for ion fluences $N_1 \geq 3 \times 10^{13} \text{ cm}^{-2}$ (Fig. 3 (c)). Once a critical damage concentration of about 30% is reached, E_{da} remains at a constant value. The here observed damage formation by the electronic energy loss of the ions is in agreement with the findings for the pristine crystal (see above), which also point to strong damage formation by the electronic energy loss of the impinging He ions.

Raman measurements suggest that the implanted layer is not amorphised. Most probably the produced structure consists of slightly misaligned crystalline regions.

References

- [1] F. Osterloh, Chem. Mater. 2008, 20, 35-54.
- [2] Akihiko Kudo *et al.*, J. Am. Chem. Soc. 1999, 121, 11459-11467.
- [3] H. Dai *et al.*, Journal of Environmental Sciences. 25 (2013) 2138-2149.
- [4] E. Wendler *et al.*, presented at IBMM 2016. To be published in Nucl. Instrum. Methods Phys. Res. B.
- [5] B. Breeger *et al.*, Nucl. Instr. and Methods Phys. Res. B. 174 (2001) 199.
- [6] J.P Biersack and J.F. Ziegler, The Stopping and Ranges of Ions in Matter, vol. 1, Pergamon Press, Oxford, 1985; www.srim.org.

The lattice expansion and anisotropic refractive index of KTiOPO_4 waveguides formed by ion implantation

L. L. Wang^{a,b}, X. J. Cui^a, J. Rensberg^b, J. J. Yin^a, S. Creutzburg^b,
K. Ritter^b, W. Wesch^b, E. Wendler^b

^a School of Physics and Technology, University of Jinan, Jinan 250022, P.R. China

^b Institut für Festkörperphysik, Max-Wien-Platz 1, 07743 Jena, Germany

Potassium Titanyl Phosphate (KTiOPO_4 , KTP) with its large optical nonlinearity, high optical damage threshold and outstanding thermal stability, is an important material for waveguide formation and application in integrated optics [1,2].

In this work, we will focus on the implantation damage effect on the properties of the KTP waveguides. The main purposes of this paper are first, to show the effective refractive indices of the KTP waveguides as a function of the ion fluence before and after annealing; second, to present the anisotropy and saturation of refractive index profiles versus fluence; third, to investigate the implantation damage and lattice expansion induced by ion implantation.

z-cut KTP crystals with size of $7 \times 7 \times 1.5 \text{ mm}^3$ and $5 \times 20 \times 1.5 \text{ mm}^3$ were provided by the School of Chemistry and Chemical Engineering, Shandong University. The channel waveguide structures were created by depositing a specially designed photoresist mask ($10 \mu\text{m}$ implanted/ $40 \mu\text{m}$ unimplanted). The masked sample was implanted with 6.0 MeV C^{3+} ions at an ion fluence of $5 \times 10^{13} \text{ ions/cm}^2$. Planar waveguides were fabricated by 6.0 MeV C^{3+} ions implanted with ion fluences ranging from $8 \times 10^{12} \text{ ions/cm}^2$ to $6 \times 10^{14} \text{ ions/cm}^2$. All samples were annealed at 260°C for 30 min.

The refractive indices n_x , n_y and n_z of the first mode of the planar KTP waveguides as a function fluence are

shown in Fig. 1. The waveguides in three directions are always barrier waveguides before annealing. After annealing, the samples implanted with fluences from $2 \times 10^{13} \text{ ions/cm}^2$ to $1 \times 10^{14} \text{ ions/cm}^2$, formed “enhanced-well+barrier” waveguides. This means that the refractive index in the waveguide region is higher than that of the substrate. “Enhanced-well+barrier” waveguides have the advantage that lower ion fluences are needed for fabrication, mono-mode performance is obtained and tunneling effects are prevented.

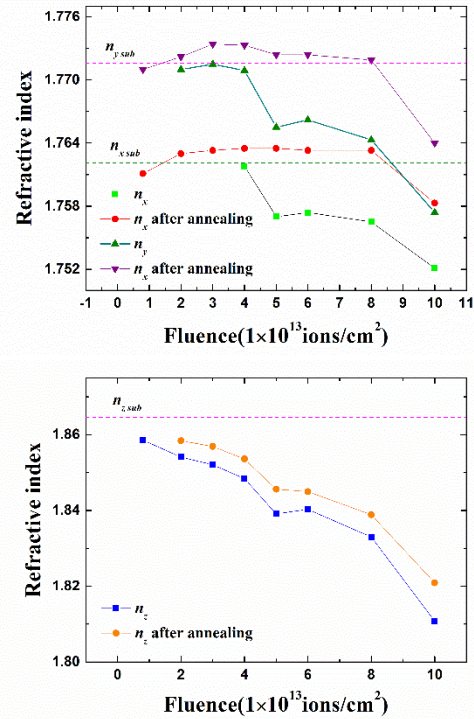


Fig. 1: Evolution of effective refractive indices n_x , n_y and n_z versus ion fluence for planar KTP waveguides formed by 6.0 MeV C^{3+} ion implantation before and after annealing.

For the higher ion fluence of 1.1×10^{14} ions/cm², both n_x and n_y of the KTP waveguides are always lower compared to the substrate value before and after annealing. The refractive indices n_z decrease with increasing ion fluence and they are always well below the refractive index of substrate. All refractive indices n_x , n_y and n_z increase slightly after annealing, which can be mainly attributed to lattice damage recovery.

For estimation of the refractive index change of the implanted and annealed layers, the Lorentz-Lorenz equation [3]:

$$\frac{n^2-1}{n^2+2} = \frac{\alpha_M}{V_M} \quad (1)$$

is used, where n is the average refractive index $n = (n_x n_y n_z)^{1/3}$, α_M is the molar polarizability and V_M is the molar volume. Differentiating Eq. (1) [4, 5], one obtains

$$\Delta n(M) = \frac{(n^2-1)(n^2+2)}{6n} \left(\frac{\Delta \alpha_M}{\alpha_M} - \frac{\Delta V_M}{V_M} \right). \quad (2)$$

This equation indicates that the refractive index change is governed by the balance between the spontaneous polarization decrease and molar volume increase. Considering that the KTP samples do not expand significantly in the two directions parallel to the surface, we can simply assume a linear relation between ΔV and Δh and use

$$\frac{\Delta V_M}{V_M} = \frac{\Delta V}{V} = \frac{\Delta h}{d} \quad (3)$$

where Δh is the lattice expansion height and $d = 5 \mu\text{m}$ the waveguide depth. The lattice expansion Δh was measured by XRD rocking curve and AFM, which is about 17 nm for $5 \times 10^{13} \text{ cm}^{-2}$. The change of the refractive index induced by lattice expansion is about $\Delta n = -0.0032$, which is not sufficient for explaining the positive change of $\Delta n = 0.0054$ observed in the experiment. As a result, additional change of polarizability α_M has to occur.

Fig. 2 depicts the effective refractive indices of $n_{x,eff}$ (green), $n_{y,eff}$ (red) and $n_{z,eff}$ (blue) as a function of the relative defect concentration measured by RBS in the KTP samples. As one can see, when the relative defect concentration is small, $n_{x,eff}$ and $n_{y,eff}$ increased, $n_{z,eff}$ decreased, decreasing the overall refractive index anisotropy. It should be noted that the strong decrease of $n_{z,eff}$ is observed for all ion fluences. The exception of $n_{z,eff}$ seems to related to the crystal structure of KTP.

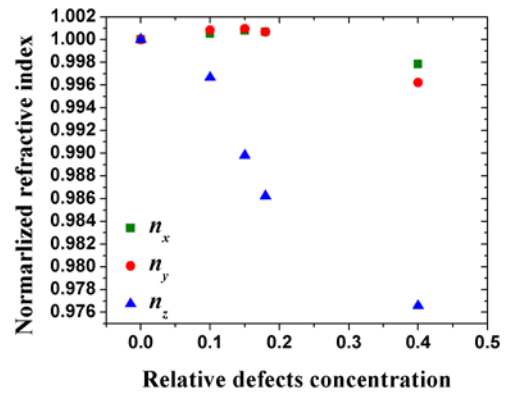


Fig. 2: Evolution of normalized effective refractive indices $n_{x,eff}$, $n_{y,eff}$ and $n_{z,eff}$ versus relative defect concentration of planar KTP waveguides formed by 6.0 MeV C^{3+} ion implantation after annealing.

When the ion fluence is as high as 6×10^{14} ions/cm², the effective refractive indices $n_{x,eff}$, $n_{y,eff}$ and $n_{z,eff}$ are very low and only small recovery occurs after annealing (not shown). Results indicate that anisotropic refractive index disappears due to the high ion fluence.

References

- [1] Y. J. Ma *et al.*, Opt. Mater. 54 (2016) 1-5.
- [2] F. Chen *et al.*, Opt. Mater. 29 (2007) 1523-1542.
- [3] V. V. Atuchin, Nucl. Instrum. Methods Phys. Res. B 168 (2000) 498-502.
- [4] H. Åhlfeldt *et al.*, J. Appl. Phys. 77 (1995) 4467-4476.
- [5] Y. Jiang *et al.*, Phys. Rev. B 75(19) (2007) 195101.

Insight into the unit cell: Structure of picene thin films on Ag(100) revealed with complementary surface science methods

Tobias Huempfer, Martin Hafermann, Christian Udhardt, Felix Otto, Roman Forker, and Torsten Fritz

Picene attracted much attention since Mitsuhashi *et al.* investigated superconducting properties of alkali metal intercalated samples. [1] However, for samples exhibiting the same nominal stoichiometry, a multitude of different phases can be observed. Thus it remains unclear which phase actually exhibits superconducting properties.

In this contribution, we study the thin film structure and molecular arrangement of pristine picene on Ag(100) which is a crucial step toward analyzing intercalated systems. [2]

The samples were prepared at room temperature under UHV conditions (10^{-9} mbar) using organic molecular beam epitaxy.

The growth of picene on Ag(100) was monitored via low-energy electron diffraction (LEED) (not shown here). At a coverage of one monolayer (ML) we determined that the adsorbed molecules arrange in a well-ordered point-on-line structure [3] that could be imaged directly using scanning tunneling microscopy (STM) (Fig. 1). The contrast of neighboring molecules alternates between bright and dark along the a_1 direction. Thus we conclude that there are two differently oriented molecules per unit cell. Yet, from the STM image it is not possible to extract further information about the precise orientation of the two differently arranged molecules in the basis. Therefore we additionally studied the electronic structure and recorded photoelectron momentum maps (PMMs) to achieve further insight into the content of the unit cell.

The UPS spectrum shown in Fig. 2(a) exhibits several features originating from molecular states. The spectrum was taken at

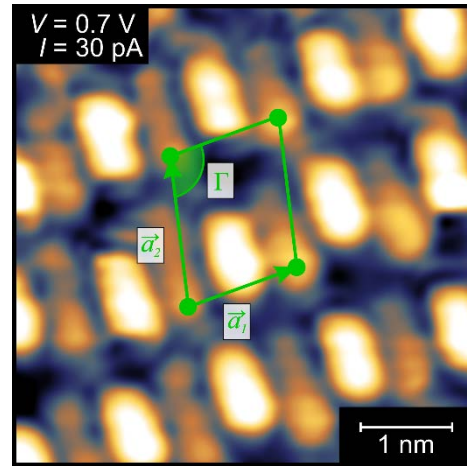


Fig. 1: STM image of 1 ML of picene on Ag(100) ($V = 0.7$ V, $I = 30$ pA, $T = 1.1$ K, 5×5 nm²). Green solid lines depict the unit cell determined from LEED measurements.

the point in k-space highlighted in Fig. 2(b). The highest occupied molecular orbital (HOMO) and HOMO-2 could be identified by comparing the features in the measured spectrum to the DFT calculation of a free picene molecule. From the energy positions of these features, we estimated the position of the HOMO-1 which is not visible in the measurement as a clear peak.

The PMMs taken at the energy positions of the HOMO (2.6 eV), HOMO-1 (2.9 eV), and HOMO-2 (3.5 eV) are shown in Figs. 2(c) and 2(d). Due to the fourfold symmetry and thus the simultaneously probed rotational domains of picene on Ag(100), sectors of 90° contain all non-redundant information. In the case of HOMO and HOMO-1 (sectors A and B), an outer ring-like pattern is observed which shows intensity maxima in approximately the same directions in k-space as in the Fermi surface (Fig. 2(b)). Besides the outer ring, inner intensity features are observed as well for the HOMO and HOMO-1 which are more

intense for the former than for the latter. Having a closer look at the energy dependence of the Γ -point region shown in Fig. 2(e), one can see that in the HOMO-region (2.6 eV–2.2 eV) the filling of the inner circle of the PMMs becomes most prominent. In the case of the HOMO-2 (Fig. 2(d) sector D), an outer ring as well as inner features are observed. The intensity maxima of the outer ring are rotated azimuthally by 45° compared to the ones of the HOMO and HOMO-1.

For a detailed analysis of the measured PMMs, we performed simulations at the given energies for the HOMO, HOMO-1, and HOMO-2 obtained on the basis of calculated DFT orbitals (B3LYP functional with 6-311G++(d) basis set) by using an algorithm introduced by Puschnig *et al.* [4] We simulated the particular PMMs for single free molecules with different tilt angles (ϑ) around the long axis of the molecule and additionally considered the fourfold rotational symmetry of the substrate.

The intensity distributions of the measured PMMs can only be explained when considering a flat-lying and a tilted molecule w.r.t. the substrate surface (especially the intensity in the Γ -point region needs consideration of about 45° tilted molecules). The simulated PMMs shown in sector C and E of Fig. 2(c) and (d) are superimposed from flat-lying and 45° tilted molecules. Due to the limited energy resolution of the electron analyzer we additionally superimposed the simulated PMMs of the HOMO and HOMO-1. These final simulations are in very good agreement with the measured PMMs. Therefore we can conclude that the unit cell is indeed composed of two differently oriented molecules, one flat lying, and the other one tilted about 45° around ϑ .

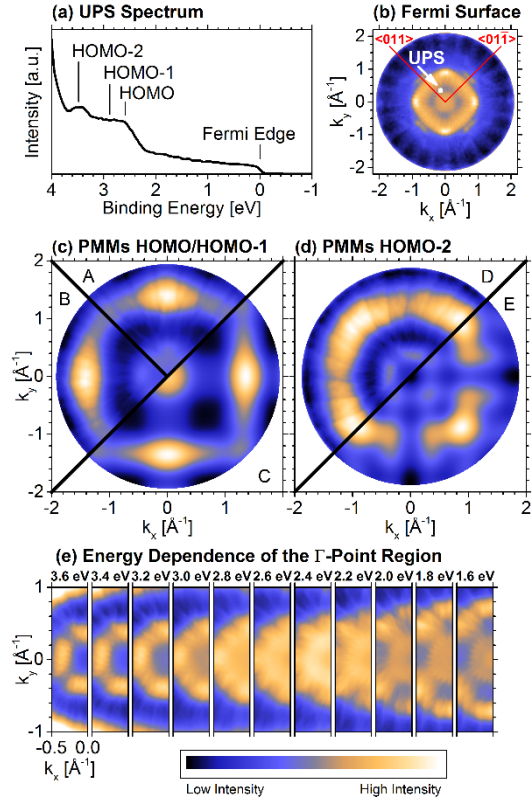


Fig. 2: (a) UPS-spectrum of 1 ML picene on Ag(100) taken at the point in k -space highlighted in (b). (b) PMM taken at the Fermi edge. (c) PMMs taken at the energy position of the HOMO (sector A, 2.6 eV) and HOMO-1 (sector B, 2.9 eV), respectively. Superposition of the PMMs of the HOMO and HOMO-1 for flat-lying and tilted molecules (tilt angle 45°) (sector C). (d) PMM at the energy position of the HOMO-2 (sector D, 3.5 eV) and simulation of the PMM of the HOMO-2 for flat-lying and tilted molecules (tilt angle 45°) (sector E). (e) PMMs that depict the energy dependence of the Γ -point region.

With the use of complementary methods we were able to study not only the structural properties of picene on Ag(100), but also the content of the unit cell composed of a flat-lying and a tilted molecule (by about 45°).

References

- [1] R. Mitsuhashi *et al.*, Nature **464**, 76-79 (2010).
- [2] T. Huempferner *et al.*, J. Chem Phys. **145**, 174706 (2016).
- [3] P. Puschnig *et al.*, Science **326**, 702-706 (2009).
- [4] S. C. B. Mannsfeld *et al.*, Phys. Rev. Lett. **94**, 056104 (2005).

Naphthalene's six shades on graphite: A surprisingly rich polymorphism

Falko Sojka, Matthias Meissner, Takashi Yamada, Toshiaki Munakata,
Roman Forker, and Torsten Fritz

Naphthalene (C₁₀H₈) is the smallest member of the polycyclic aromatic hydrocarbons (PAH). For C₁₀H₈ two commensurate monolayer phases on graphite have been reported so far [1,2]. By using distortion corrected low-energy electron diffraction (LEED) we re-analyze precisely the lattice parameters of this system. Surprisingly, we found a total of six different phases.

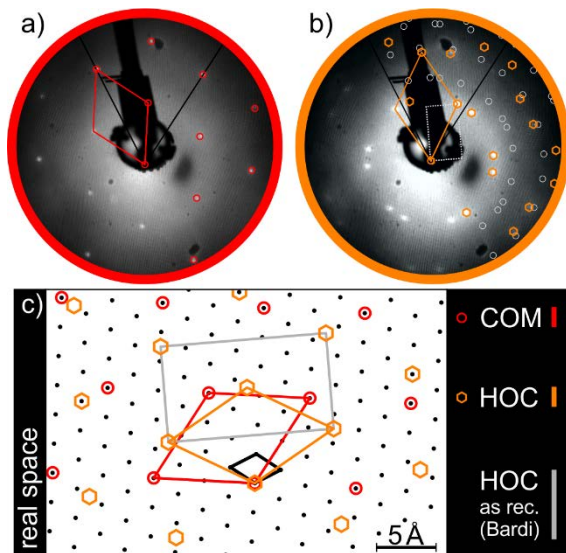


Fig. 1: Representation of the two previously reported phases of C₁₀H₈ on graphite. (a,b) LEED images partially superimposed with simulated LEED patterns; primary electron energies: (a) 50.9 eV, (b) 50.9 eV. (c) Real space lattices; black dots belong to the graphite crystal structure. The gray unit cell in (c) and the gray circles in (b) represent the rectangular structure according to the alternative suggestion of Bardi et al.[1].

Figure 1 shows the two previously reported phases, a commensurate (COM) and a higher-order commensurate (HOC) one. Bardi *et al.* could only observe the first order LEED reflexes and presented

two different suggestions for the epitaxial relation [1]. We find that the hexagonal description is the correct one.

Three new phases are identified as point-on-line structures (see Fig. 2a-c,e). And last but not least one builds an incommensurate adlayer. However, it shows a well-defined epitaxial relation with respect to the substrate. This phase has a bulk-like structure with upright standing molecules and has an enormous temperature stability, once it has formed.

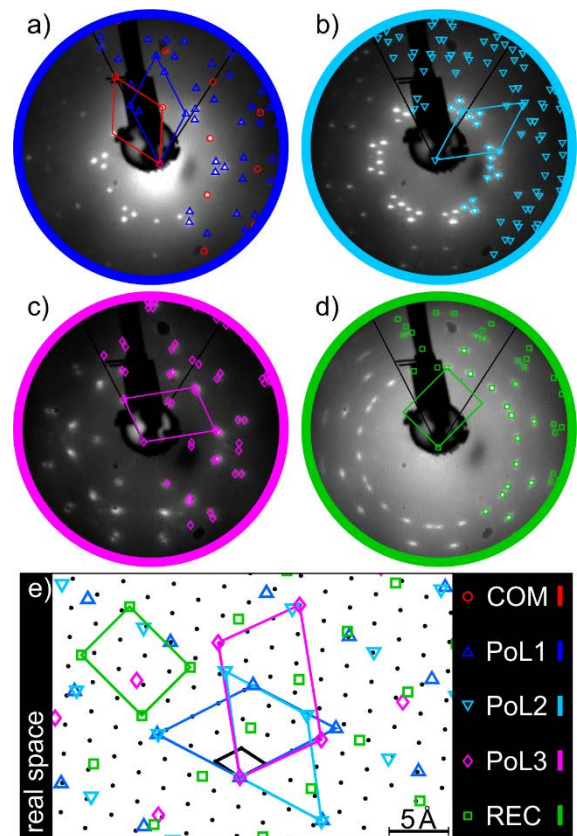


Fig. 2: Representation of the six new phases of C₁₀H₈ on graphite. (a-d) LEED images partially superimposed with simulated LEED patterns; primary electron energies: (a) 60.2 eV, (b) 64.2 eV, (c) 37.9 eV, (d) 76.3 eV. (e) Real space lattices; black dots belong to the graphite crystal structure.

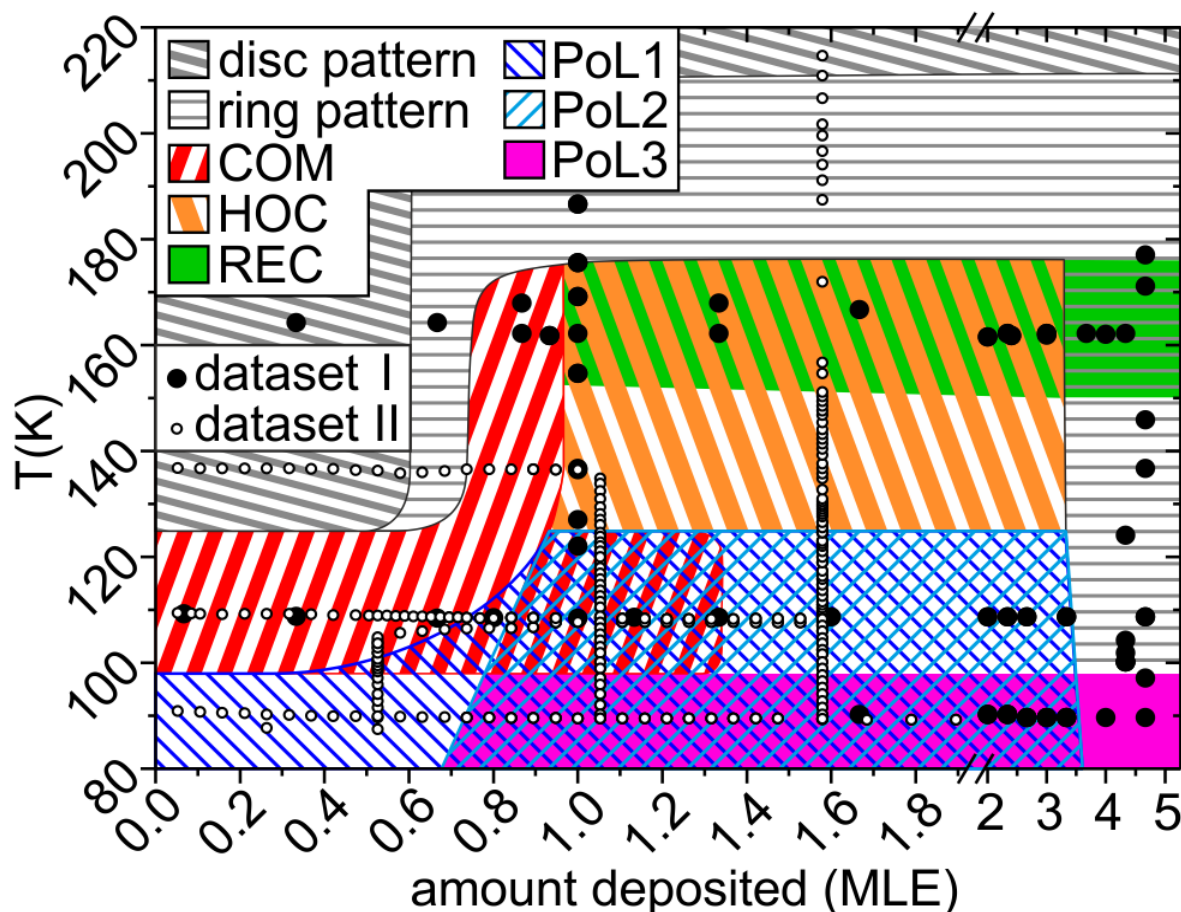


Fig. 3: Phase diagram of $C_{10}H_8$ on graphite. (a) Two analyzed LEED data sets (each data point represents at least one LEED image) are plotted with a different color code to distinguish between them. Different backgrounds represent our interpretation of the coverage- and temperature-dependent occurrence of the phases. REC and PoL3 are only observed when grown in the indicated temperature regimes.

We investigated further the physical conditions (surface coverage, temperature) under which the different phases occur or vanished. Figure 3 represents our findings. Two different datasets (each of them contains several LEED series) were matched in terms of the amount deposited (monolayer-equivalent, MLE).

A significant change in the molecule-molecule interaction occurs at around 125 K. At this Temperature the interaction changes from effectively repulsive to effectively attractive and vice versa. For submonolayer 2D-islands ($T < 125$ K), we can obtain a change in the crystal structure (from PoL1 to COM) when 100 K is exceeded.

In conclusion we found that the growth of this smallest PAH on graphite depends on the physical conditions like coverage and temperature in a remarkably complex manner where in many cases a simple commensurate registry is not the preferred epitaxial relation. We believe that such manifold systems should be taken into consideration for theories which try to predict structures and morphologies of adsorbates on surfaces.

References

- [1] U. Bardi *et al.*, *Langmuir* **3**, 159-163 (1987).
- [2] T. Yamada *et al.*, *Chem. Phys. Lett.* **546**, 136-140 (2012).

Estimation of silicon suspension thermal noise in thermal non-equilibrium

René Glaser, Ronny Nawrodt

In February 2016 the LIGO Scientific Community astonished the public with the release of the first direct proof of the existence of gravitational waves, in this case emitted by two merging black holes [1]. This huge scientific success represents a further proof of Einstein's general relativity and verifies the concept of interferometric gravitational wave detectors. The two LIGO detectors in Hanford and Livingston showed their potential of measuring strains down to the order of 10^{-21} . But luckily the detected signal was quite strong. Additional investigations are needed to enhance the sensitivity of future detectors, allowing the detection even weaker signals.

To achieve better sensitivities, it is necessary to understand the mechanisms of noise within an interferometric gravitational wave detector. Previous sensitivity calculations assume the detector to be in thermodynamic equilibrium. But this is not always the case, since e.g. due to the high laser power used in the detector, even small absorption causes a rise in temperature of the optical components and therefore parts of the detectors are driven out of thermal equilibrium. This work will have a look at the influence of temperature gradients within silicon beams as a material for monolithic suspensions for future detectors.

Thermal noise and mechanical dissipation are strongly correlated and therefore measuring the mechanical loss, allows the calculation of the estimated thermal noise. A setup for measuring the mechanical loss of a silicon beam, driven out of equilibrium by applying a temperature gradient is shown in [2].

Using an effective temperature approach, we are able to compare the expected noise of a system in thermal equilibrium to the non-equilibrium case. Following [3] the effective temperature of mode n is given by

$$T_n^{\text{eff}} = \frac{1}{l} \int_0^l T(x) w_n^{\text{diss}}(x) dx, \quad (1)$$

for a beam with length l . $T(x)$ is the temperature profile within the sample. In this case a linear profile is used where $T(0)$ is the temperature of the upper clamp and $T(l)$ is the temperature of the lower clamp. In (1) $w_n^{\text{diss}}(x)$ represents the so called normalized dissipation rate for the n -th mode. This value is calculated using the FEM software Comsol [4]. Two examples are shown in figure 1. For calculating the dissipation rate, the mechanical loss data at constant temperature has been used.

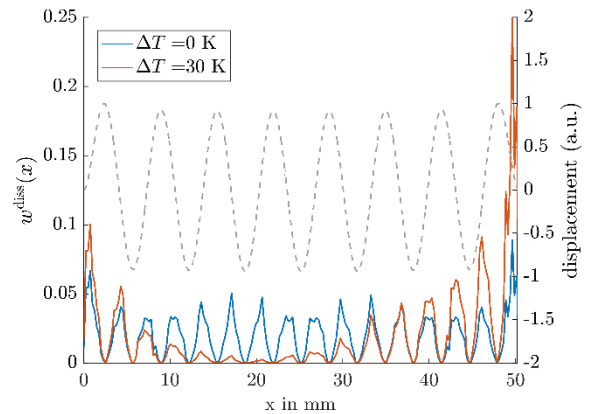


Fig. 1: Two examples of the calculated normalized dissipation rate used in equation (1). The light grey curve shows the mode shape of the 58.5 kHz mode, used here.

Most of the power is dissipated at both ends of the sample, due to strong bending of the beam at the clamped ends. The average temperature of the sample was about $T_{\text{avg}} = 120$ K and $T(0) = T_{\text{avg}} -$

$\Delta T/2$ and $T(l) = T_{\text{avg}} + \Delta T/2$. As can be seen in figure 1, for higher temperature difference the dissipated power of the middle part of the sample becomes less significant.

Using this technique for the 58.5 kHz mode under investigation and for a region around 120 K, the effective temperatures are shown in figure 2.

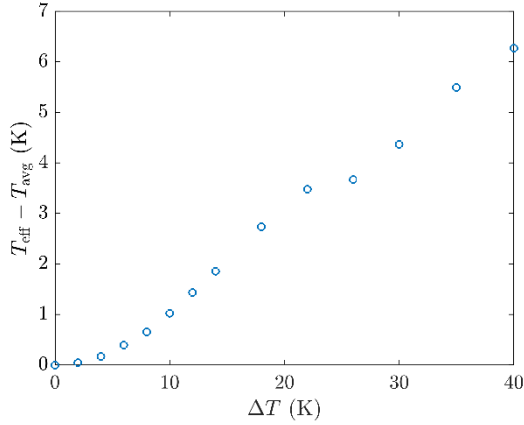


Fig. 2: For higher temperature differences, the effective temperature increases. The exact values depend on the specific temperature of the sample.

Using an extended equipartition relation [3]

$$\frac{1}{2}k_n \langle d_n^2 \rangle = \frac{1}{2}k_B T_n^{\text{eff}}, \quad (2)$$

with the local stiffness k_n of the n -th mode, the Boltzmann constant and the mean square deflection $\langle d_n^2 \rangle$ for the n -th mode as a measure for the thermal noise, it is possible to estimate the influence of the temperature gradient on the thermal noise around the resonance of the mode under investigation, in this case of the 58.5 kHz mode of the sample.

Following the conceptual design study for the Einstein Telescope [5] – a future gravitational wave detector using silicon as material for the optical components and monolithic suspensions – the temperature of the mirror will be at 10 K and the top end of the suspension fiber will be held at

5 K. Therefore we have a temperature difference of 5 K. Since we have no direct data for this low temperatures, let's assume the average temperature to be 120 K. In this case, the thermal noise around the 58.5 kHz mode can be estimated to be about 9% higher, compared to the equilibrium case. Up to about 20 K temperature difference, the increase in thermal noise shows a quadratic dependence of the temperature difference.

Further investigations concerning lower temperatures of about 4 K to 40 K are still in progress. This allows us to estimate the rise in thermal noise for the Einstein Telescope due to the thermal gradient within the suspension material. For a complete noise estimate over the proposed frequency range, the frequency dependence has to be considered, since the normalized dissipation rate depends on the mode shape and therefore on the frequency.

References

- [1] B. P. Abbot *et al.*, Phys. Rev. Lett. **116**, 061102 (2016).
- [2] R. Glaser *et al.*, Annual Report 2013, 71 (2014).
- [3] M. Geitner *et al.*, arXiv preprint, arXiv:1612.04134 (2016).
- [4] <http://www.comsol.com>
- [5] M. Abernathy *et al.*, Einstein gravitational wave Telescope Conceptual Design Study (2011).

Precise optical bulk and surface absorption measurements in high purity silicon

Johannes Dickmann, Rene Glaser, Ronny Nawrodt

Silicon is a promising material for high-precision metrological applications such as gravitational wave detectors and frequency stabilized laser systems for the realization of optical clocks. In order to maximize the performance of such experiments, the optical absorption of all involved elements should be as small as possible. This sets high demands to the purity of the utilized silicon material. For quantitative statements on the optical performance it is essential to measure the surface and bulk absorption separately. Photothermal deflection spectroscopy (henceforth PDS) is a powerful tool for these measurements. In this contribution, theoretical and experimental aspects of such high resolution measurements are discussed.

The PDS is a classical pump-probe experiment (see Fig. 1). The optical absorption of the sample (7) at a particular wavelength λ is studied using a focussed laser beam (1) and (6). The output power of the laser can be changed by rotating the quarter-wave plate (2) combined with a linear polarizing beam splitter (3). The optical chopper (4) modulates the pump signal. A second laser beam (9) propagates obliquely to the pump beam at a certain angle. The concave mirror (10) focusses the probe beam on the split diode (12), which reads out its displacement. Only the probe beam can pass the narrow band filter (11), preventing fault signals due to stray light of the pump beam. (5) and (8) are absorbers.

The experimental setup has some degrees of freedom (e.g. the angle between the laser beams, the beam radii, the powers of the laser beams, the angle of the sample,

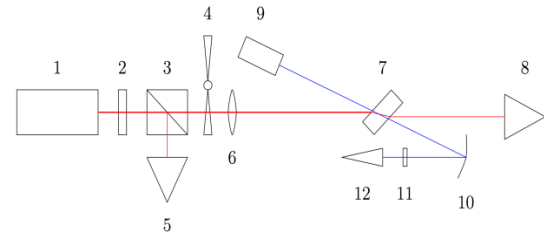


Fig. 1: Simplified PDS setup for measurements of optical absorption coefficients. The red line illustrates the pump- and the blue one the probe beam. The components are explained in the text. [1]

the polarization states, the wavelengths), which are decisive for a successful measurement. The optimal setup parameters depend on the material parameters.

Numerical calculations were programmed which help to estimate the influence of all parameters and thereby to optimize the experimental setup. An example of such a numerical calculation is shown in Fig. 2.

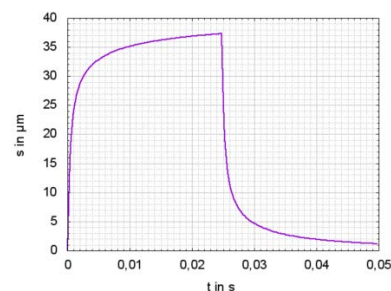


Fig. 2: Example for the numerically calculated displacement s of the probe beam in dependence of time t at a chopper frequency of $f=20$ Hz. The other parameters for this calculation are listed in [1].

We present results of the following measurements: Bulk absorption of silicon samples with variable doping gradients as well as room temperature surface

absorption in dependence of surface roughness.

Fig. 3 shows the measured absorption coefficients in dependence of the depth under the surface.

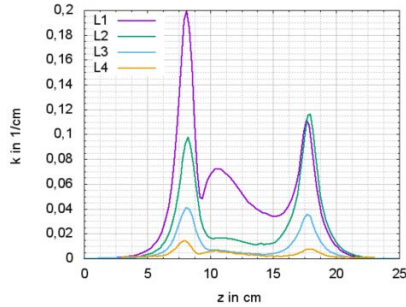


Fig. 3: Measurement of the absorption coefficient κ in dependence of the depth under the surface at approx. $z=7$ mm.

All samples were p-doped in different concentrations (see Tab. 1).

Tab. 1: Sample resistivities and measured bulk absorptions of differently doped Silicon samples.

Sample	Resist. ρ in Ωcm	κ in cm^{-1}
L1	$0,311 \pm 0,017$	$0,081 \pm 0,008$
L2	$0,633 \pm 0,033$	$0,029 \pm 0,006$
L3	$2,5 \pm 1,5$	$0,0080 \pm 0,0005$
L4	$22,5 \pm 2,5$	$0,0011 \pm 0,0002$

The thus obtained relation between optical absorption and electrical resistivity (see Fig. 4) reads

$$\frac{\kappa}{\text{cm}^{-1}} = (0,0237 \pm 0,0014) \frac{\Omega\text{cm}}{\rho} \quad (1)$$

and agrees well with [2].

For the investigation of surface absorption, a silicon wafer was split into four parts. The backsides of these parts were polished identical whereas the front sides were polished for different lengths of time. The roughness of the front sides was determined using an AFM. The resulting plot (see Fig. 5) shows this context.

There are two regimes:

1. For high roughness $R > 1$ nm:

$$\kappa \propto R$$

2. For small roughness $R < 0.5$ nm:

$$\kappa \propto R^{-2,5}$$

This probably results from different stray

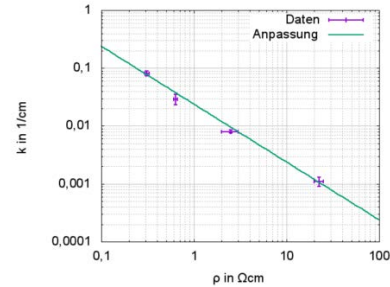


Fig. 4: Measurement of the bulk absorption coefficient κ in dependence of the electrical resistivity ρ .

light regimes on the surface.

The developed experimental setup is very sensitive to material disturbances. Therefore, an application in quality control of 2D (thin films) and 3D (bulk materials) is possible.

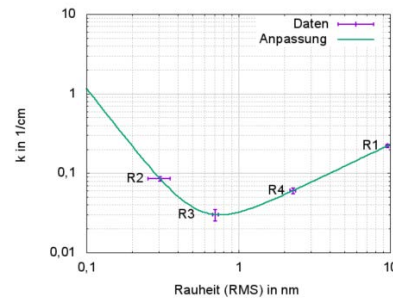


Fig. 5: Measurement of the surface absorption coefficient κ in dependence of the surface roughness.

References

- [1] J. Dickmann: Master thesis, Friedrich-Schiller- Univ. Jena, 2016.
- [2] J. Degallaix, et al. Bulk optical absorption of high resistivity silicon at 1550 nm, Optics Letters **38** 2047 (2013).

Angular dependence of Nd(O,F)FeAs thin film grain boundary junctions

Stefan Schmidt, Sebastian Döring, Frank Schmidl, Naoki Sumiya¹, Hiroshi Ikuta¹, Fritz Kurth², Paul Seidel

¹ Nagoya University, Dept. of Crystalline Materials Science, Chikusa-ku, 464-8603 Nagoya

² IFW Dresden, Institute for Metallic Materials, Helmholtzstraße 20, 01069 Dresden

After their discovery in 2008, iron-based superconductors have been investigated thoroughly. Especially, their electrical properties stand out compared to conventional superconductors and even cuprates. The latter struggle with a strong deterioration in electrical properties when natural or artificial grain boundaries are present. The iron-based superconductors, however, exhibit a shallow decline of the critical current density at larger angles of the grain boundary [1]. Here we present electrical investigations on the oxypnictide superconductor Nd(O,F)FeAs deposited on bicrystalline substrates with different grain boundary angles.

A two-step process was utilized to achieve the difficult fluorine-doping using molecular beam epitaxy. Details on the process can be found in reference [2]. This material is of great interest because of its

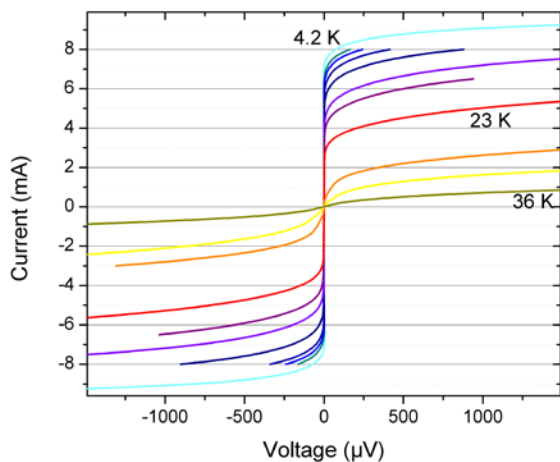


Fig. 1: Current-voltage characteristics of a microbridge ($d = 8 \mu\text{m}$) with a 3° grain boundary angle at different temperatures.

high critical temperature and its interesting flux pinning behavior recently discovered by Tarantini *et al.* in cooperation with our group [3].

Bridges over grain boundaries with very small mismatch angles of 3° develop symmetric, flux-flow dominated I - V characteristics, see fig. 1. The same behavior has been observed in microbridges of Nd(O,F)FeAs thin films without artificial grain boundary. Thus, a small grain boundary angle seems to have little influence on the electrical properties.

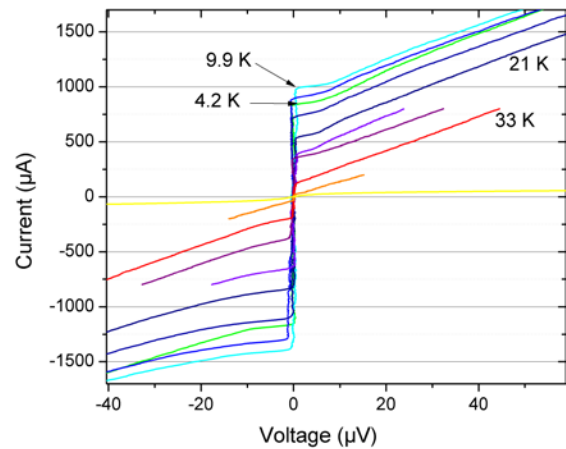


Fig. 2: Current-voltage characteristics of a microbridge ($d = 10 \mu\text{m}$) with a 24° grain boundary angle at different temperatures.

A larger grain boundary angle of 24° leads to a different behavior: A sharper transition from voltage-free to the resistive branch is apparent, which represents Josephson-like behavior. In fig. 2 the current-voltage characteristics at different temperatures are shown for a microbridge with a width of $10 \mu\text{m}$. The critical current

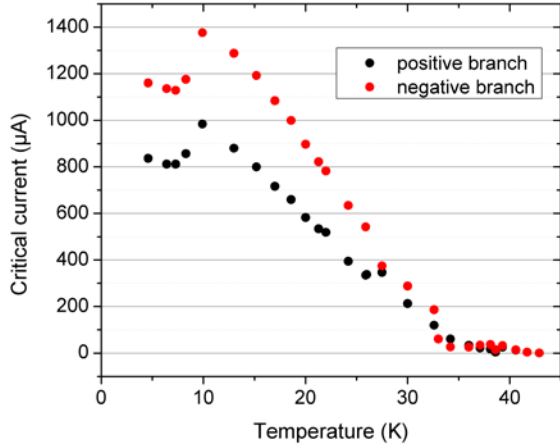


Fig. 3: Temperature dependence of the critical current derived from the I - V characteristics shown in fig. 2.

values in the positive current branch seem to differ from the ones in the negative branch. At 4.2 K the positive I_c is 0.82 mA, whereas the negative value is -1.15 mA. Interestingly, the critical current values at 9.9 K and 13 K exceed those at 4.2 K in both current branches, see fig. 3. This is in contrast to the standard theory that predicts a gradual decline of some sort of the critical current. However, a second series of measurements showed a jump at a similar temperature, but the current branches moved in different directions. The critical current of the positive branch jumped towards higher values. In contrast, the critical current of the negative branch jumped to lower absolute values.

These measurements imply the presence of a disturbance that changes at around 8 to 9 K. One possible explanation would be magnetic flux that is trapped at impurities in the microbridge and relaxes at sufficiently high temperatures.

The critical current density of grain boundary junctions exponentially decays with increasing grain boundary angle once a threshold angle is exceeded, as it was derived for cuprate superconductors [4].

As a measure for the exponential decrease an angle θ_0 can be introduced, so that the decrease can be described as a function of the grain boundary angle θ_{GB} and the starting current density j_{c0} :

$$j_c = j_{c0} e^{-\theta_{GB}/\theta_0}$$

The characteristic angle θ_0 of cuprate superconductors was derived to be 4.3° [4], which refers to a steeper decrease compared to the one found for $\text{Ba}(\text{Fe},\text{Co})_2\text{As}_2$, having a value of 8.5° [1]. The angular dependence of the critical current density of $\text{Nd}(\text{O},\text{F})\text{FeAs}$ grain boundary junctions is shown in fig. 4. A simulation of the exponential curve with a characteristic angle of 8.5° is drawn as a solid line in both the main frame and the inset. Thus, the j_c reduction due to the grain boundary is not as severe as in the cuprate superconductors and similar to the value in $\text{Ba}(\text{Fe},\text{Co})_2\text{As}_2$.

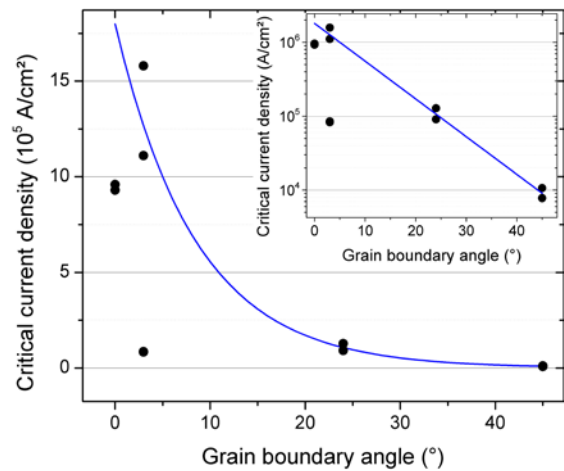


Fig. 4: Critical current densities of different $\text{Nd}(\text{O},\text{F})\text{FeAs}$ microbridges at 4.2 K versus their respective grain boundary angle. Inset: logarithmic depiction of the same data.

References

- [1] T. Katase *et al.*, Nat. Commun. **2**, 409 (2011).
- [2] T. Kawaguchi *et al.*, Appl. Phys. Express **4**, 083102 (2011).
- [3] C. Tarantini *et al.*, Sci. Rep. **6**, 36047 (2016).
- [4] H. Hilgenkamp *et al.*, Appl. Phys. Lett. **73**, 265-267 (1998)

Modes of collective excitations in two inductively coupled long Josephson junctions

Alexander Grib¹ and Paul Seidel

¹Physics Department, Kharkiv V. N. Karazin National University, 61022, Kharkiv, Ukraine

It is well known [1] that oscillations of coupled oscillators are described by means of a set of modes of collective excitations which are produced by all oscillators of the system. Modes of collective excitations of two coupled oscillators are so-called in-phase and anti-phase modes [2]. Such modes were found for the movement of fluxons under the influence of magnetic field in stacks of Josephson junctions made of low-temperature superconductors [3]. Here we study modes of collective excitations appeared *without applied magnetic field* in the stack of two intrinsic Josephson junctions made of high-temperature superconductors. Additional excitations are introduced through normal (non-superconducting) edges of the stack. Normal edges can appear in high-temperature superconductors due to diffusion of the oxygen out of the sample. In the solitary long junction, mentioned excitations reflect from edges and form standing waves at some frequencies [4]. Standing waves interact with Josephson generation and produce so-called zero-field steps in the IV-characteristic [4]. Resonant voltages of these steps correspond to even Fiske steps [5]:

$$V_m = \frac{\Phi_0 \bar{c} m}{D}, \quad m=1,2,3,\dots, \quad (1)$$

where \bar{c} is velocity of light in the junction and D is the length of the junction. In a stack of two inductively coupled junctions (Fig. 1), resonant voltages of normal modes are determined as follows [6]:

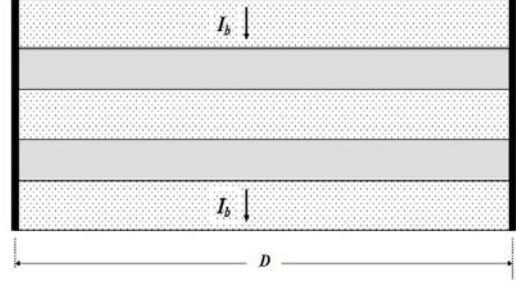


Fig. 1. The stack of two long junctions. Black lines at edges symbolize normal edges.

$$V_{m,a} = \frac{V_m}{\sqrt{1+\alpha}}, \quad V_{m,i} = \frac{V_m}{\sqrt{1-\alpha}}, \quad (2)$$

where α is the coefficient of coupling. These resonant voltages are seen in the IV-curves as two zero-field steps. To model these steps, we described each of the long junctions in a stack as a set of elementary junctions [6]. Normal edges were modeled as RLC - contours at edges of each junction. We calculated IV-characteristics of the stack $v \equiv V/V_c = f(I_b/I_c)$ (here V_c is the critical voltage, I_b is the bias current and I_c is the critical current), and the power of ac emission S of the stack. The IV-characteristic of the solitary long junction is shown in Fig. 2a. The zero-field step is formed at $v_1 \approx 0.35$. Because the value of v_1 is in the region of the jump of the voltage in the IV-curve, for the comparison of results of our model with the theory we use positions of tops of steps v'_1 (see Fig. 2a). In the stack of two inductively coupled junctions, the zero-field step is split into two steps (Fig. 2b),

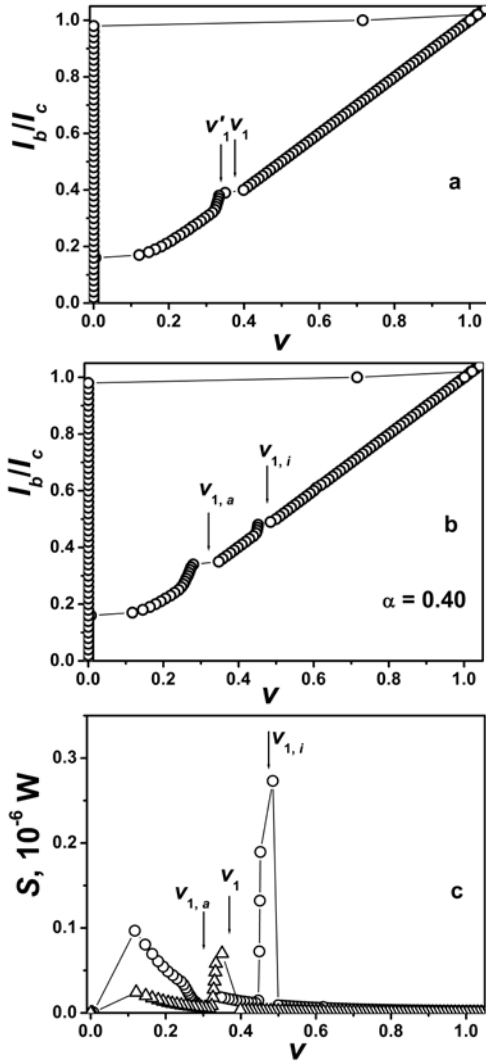


Fig. 2: (a)-the IV-characteristic of a junction with the length $D=120 \cdot 10^{-6}$ m. (b) - the IV-curve of two coupled junctions. (c) - the dependence of $S(v)$ for a solitary junction (triangles) and for two junctions with $\alpha = 0.4$ (circles). Parameters of the junction: $I_c=36$ mA, $V_c=3.12$ mV, $\bar{c}=7.1 \cdot 10^7$ m/s.

which correspond to frequencies of modes of collective oscillations (see Eqs. (2)). The maximum of power of ac emission is found at $v_{1,i}$, whereas at $v_{1,a}$ there is the minimum of S (Fig. 2c). The maximum of emission power is as much as four times larger than the maximum for the solitary junction (Fig. 2c). Coherent emission appears at this voltage. Dependences of voltages at tops of steps $v'_{1,a}$ and $v'_{1,i}$ on the

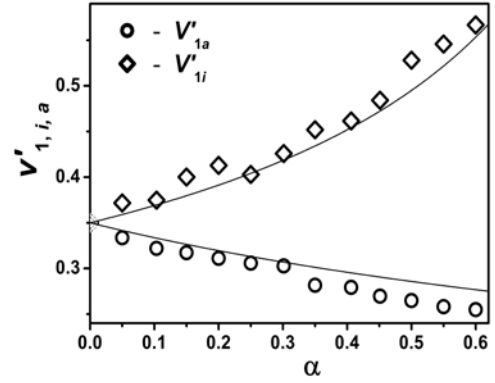


Fig. 3: Dependences of $v'_{1,a}$ and $v'_{1,i}$ on the parameter α . Lines are approximations by Eqs. (2).

parameter α can be approximated by means of Eq. (2) (Fig. 3).

In conclusion, we calculated IV-characteristics and power of ac emission from a stack of two inductively coupled intrinsic Josephson junctions with normal edges. We proved the presence of two modes of collective excitations in the stack. We showed that there is coherent emission at the zero-field step which corresponds to the mode of in-phase collective excitations. We believe that coherent emission from stacks of intrinsic Josephson junctions in high-temperature superconductors appears at voltages which correspond to modes of in-phase oscillations [7].

References

- [1] L.D. Landau & E.M. Lifshitz, "Mechanics", Oxford, Pergamon Press, 1969, p. 68.
- [2] S. Sakai, P. Bodin, N. F. Pedersen, J. Appl. Phys., **75**, 2411-2418 (1993).
- [3] S. Sakai *et al.*, Phys. Rev. B, **50**, 905-914 (1994).
- [4] T. A. Fulton and R. C. Dynes, Solid State Commun., **12**, 57-61 (1973).
- [5] A. Barone, G. Paternò, "Physics and Application of the Josephson Effect", NY, John Wiley & Sons, 1982, pp.235-290.
- [6] Alexander Grib and Paul Seidel, IEEE Trans. Appl. Supercond., **26**, 1801004 (2016).
- [7] L. Ozyuzer *et al.*, Science **318**, 1291-1293 (2007).

LC-shunted HTS Josephson junctions

Yu. M. Shukrinov^{a,b}, I. R. Rahmonov^{a,c}, K. V. Kulikov^{a,b}, A. E. Botha^d, A. Plecenik^e,
W. Nawrocki^f, P. Seidel

^a*BLTP, Joint Institute for Nuclear Research, Dubna, Moscow Region, 141980, Russia*

^b*Dep. of Theoretical Physics, International University of Dubna, Dubna, 141980, Russia*

^c*Umarov Physical Technical Institute, TAS, Dushanbe, 734063 Tajikistan*

^d*Department of Physics, University of South Africa, Florida 1710, South Africa*

^e*Department of Experimental Physics, Comenius University, Bratislava, Slovakia*

^f*Poznan University of Technology, Poznan, Poland*

Shunting of Josephson junctions (JJs) by inductive and capacitive circuit elements (so-called LC-shunting), forms a multiple resonance circuit. Such shunting allows effective control and manipulation of the resonance features, which are potentially useful in superconducting electronics. When the Josephson frequency ω_j is equal to the resonance frequency of the circuit ω_{rc} , the oscillations in the Josephson junction are tuned to this frequency. This resonance could manifested itself in the current-voltage characteristic (IV-characteristic) in a variety of ways; such as, steps [1, 2], or humps and dips [3, 4]. LC-shunting leads to a step in the one loop IV-characteristics, when the value of Josephson frequency approaches that of the resonance circuit. As we have discussed previously, the location of this step depends on parameters of the LC-circuit [5]. The existence of steps in the IV-characteristic of various shunted systems of Josephson junctions has also been reported in a number of experimental and theoretical works. (See, for example, [6, 7].) In Ref. [8] we have described the novel features that appear in shunted system of coupled JJs, which is a model for intrinsic JJs (IJJs) in high- T_c superconductors. We have discussed the properties of parallel resonance realized at the conditions when the Josephson frequency approaches the frequency of the resonance circuit formed by the IJJs with LC-shunting. We have demonstrated the

parametric resonance and excitation of a longitudinal plasma wave over a current interval corresponding to the resonance circuit branch (rc-branch). We have shown that the temporal dependence of the total voltage across the stack (or the shunt capacitor), can reveal whether or not the superconducting layers become charged, which might be a useful criterion for observing such charging. To describe the properties of our system, we use the usual resistively and capacitively shunted junction (RCSJ) model which captures its main features. We consider our system under external electromagnetic radiation. Figure 1 shows the IV-characteristic and charge-time dependence for the first S-layer of ten JJs at frequency of radiation $\omega_R=3.2596$, equal to the frequency of the resonance circuit, and amplitude $A=0.2$. The IV-characteristic (Fig.1(a)) has the Shapiro step at the end of the rc-branch (at $V=32.596$ and its harmonic at $V=65.110$), so the charging interval does not touch it. Charging of superconducting layers (shown in Fig.1(b)) appears in the current interval corresponding to the central part of rc-branch which is lower than the position of the Shapiro step on voltage scale. Below we will discuss the features in the case when charging happens in the current interval, overlapped with a Shapiro step. In the present case, as we have seen in this figure, we have observed a splitting of charge oscillations in the superconducting layers for some time regions.

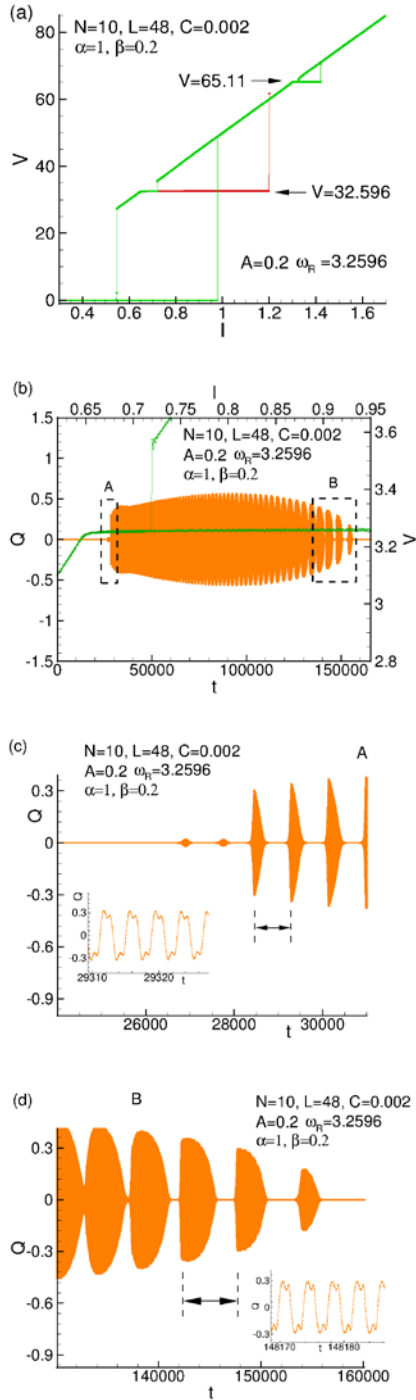


Fig. 1: (a) IV-characteristic of the system of ten JJs at $\beta=0.2$, $\alpha=1$, $L=48$ and $C=0.002$ under external electromagnetic radiation with frequency $\omega_R=3.2596$ and amplitude $A=0.2$. (b) Charge-time dependence for the first superconducting layer in the stack at the same parameters as in (a). (c) and (d). Enlarged parts of charge-time dependence in the beginning and at the end of the charging interval, respectively. Insets demonstrate character of charge oscillations in the corresponding regions. From [8] with permission of IOP Publishing.

Figures 1 (c,d) enlarge the dependence at the onset and at the end of the charging interval, demonstrating the splitting character of the charge oscillations. We see that the time interval (period) of splitting increases as the resonance point is approached, but the character of oscillations, shown in the inset to the figures, does not change. The observed splitting is a manifestation of a beating branch of the Josephson junction. So, we expect that temporal splitting of charge oscillations would disappear in the bias current interval corresponded to the overlapping of charging interval in current and the Shapiro step.

References

- [1] Jensen H. D., Larsen A., Mygind J., Physica B, 165, 1661 (1990)
- [2] Larsen A., Jensen H. D., Mygind J., Phys. Rev. B, 43, 10179 (1991)
- [3] Tachiki M., Ivanovic K., Kadowaki K. and Koyama T., Phys. Rev. B, 83, 014508 (2011)
- [4] Zhou T., Mao J., Cui H., Zhao X., Fang L. and Yan S., Physica C, 469, 785 (2009)
- [5] Shukrinov Yu. M., Rahmonov I. R., Kulikov K. V., JETP Letters, 96, 657 (2012)
- [6] Likharev K. K., Dynamics of Josephson Junctions and Circuits (Gordon and Breach, New York) 1986
- [7] Almaas E. and Stroud D., Phys. Rev. B, 65, 134502 (2002)
- [8] Yu. M. Shukrinov, I. R. Rahmonov, K. V. Kulikov, A. E. Botha, A. Plecenik, W. Nawrocki, P. Seidel, Supercond. Sci. Technol. 30, 024006 (2017).

Investigation of flux-trapping in superconducting thin-film structures during cool-down

Thomas Schönau^{1,2}

M. Schmelz², V. Zakosarenko³, R. Stolz², M. Meyer³, S. Anders², S. Linzen² and H.-G. Meyer²

¹Friedrich-Schiller-University Jena, Institut für Festkörperphysik, Helmholtzweg 5, D-07743 Jena, Germany

²Leibniz Institute of Photonic Technology, PO Box 100239, D-07702 Jena, Germany

³Supracon AG, An der Lehmgrube 11, D-07751 Jena, Germany

The trapping of magnetic flux in superconducting thin films during cool-down is generally problematic, since it can affect the operation and performance of superconducting electronics and sensors.

This especially holds true for SQUID-based absolute vector magnetometers, as proposed by [1–3] and [4,5], because trapped flux will influence the magnetometer offset, which therefore may change after each thermocycle.

Several publications address the theory of flux-trapping in narrow superconducting strips and conclude that magnetic flux is only trapped if the magnetic field during cool-down exceeds a critical value of $B_c = c \Phi_0 / w^2$ [6]. Here, w is the width of the strip line and c is a constant between $\pi/4$ and 1.65, depending on the theory taken into account. Throughout this work, $c=1.65$ is chosen since this value is best reasoned and experimentally verified. Furthermore, it should be addressed that the magnetic moment of vortices trapped in thin films also increases with the linewidth w [7].

Thus, all wide superconducting structures on the chip are presumable sources for far-ranging magnetic stray fields.

Based on these deliberations, the linewidths in our SQUID-designs were restricted to less than $6 \mu\text{m}$ across the whole chip, including also several wide superconducting structures at the chip boundary, which were slit to a comb-like shape, as exemplarily depicted in Fig. 1 (b). The corresponding critical field of $B_c \approx 90 \mu\text{T}$, resulting from theory, is far beyond the Earth's magnetic field of about $50 \mu\text{T}$. Thus, flux trapping should be avoided in the case of cool-down even in unshielded magnetic environment.

In order to experimentally verify the expectations, we performed the required measurements as following: A homogeneous background field B_E is applied to the SQUID, which is immersed in liquid helium and shortly heated over its transition temperature (bias and feedback currents are disabled). After reaching

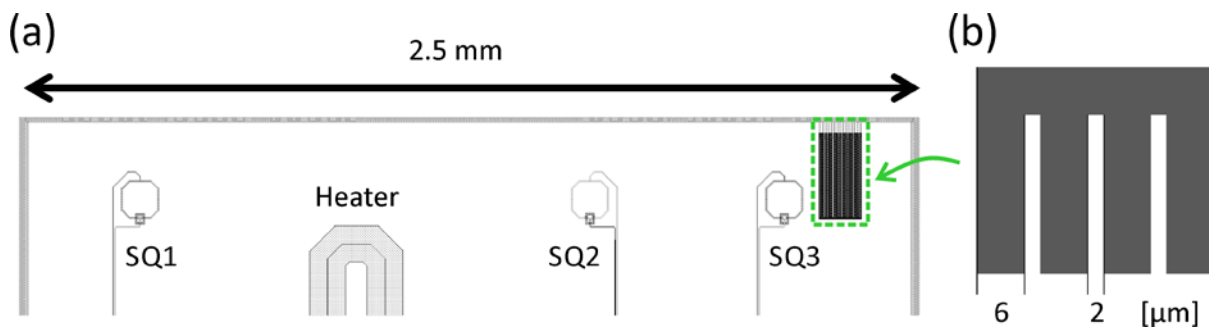


Fig. 1: The test chip (a) is composed of three identical SQUIDs with significantly different distance to the comb-like superconducting structure, depicted in detail in (b).

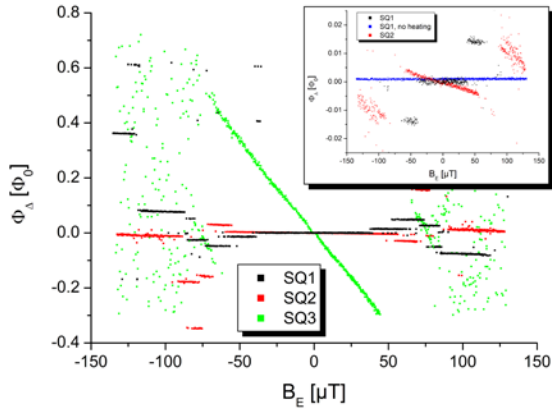


Fig. 2: Results of the flux trapping measurements performed with the test chip. The inset provides a detailed view of the interval $-0.03 < \Phi_{\Delta}/\Phi_0 < 0.03$.

equilibrium temperature, B_E is slowly ramped down to zero and afterwards the shift $V(\Phi) \rightarrow V(\Phi + \Phi_{\Delta})$ of the SQUID's flux-voltage characteristic is read out.

In contrast to theory, a quasi-continuous linear dependency $\Phi_{\Delta} \propto B_E$ could be measured even for arbitrarily low B_E . The origin of this slope, however, must be related to the superconducting phase transition, since it appears only if the chip is heated. It is therefore reasonable to assume a large amount of flux quanta to be trapped at a large distance to the SQUID. To examine this hypothesis, three equal SQUIDs (SQ1 to SQ3) were combined on a test chip, as depicted in Fig. 1 (a). One of the comb-like superconducting structures was placed next to SQ3 so that potentially trapped flux is expected to couple strongly to this SQUID.

The results of the flux trapping measurements performed with this test chip are shown in Fig. 2. As expected, the slope of $\Phi_{\Delta}(B_E)$ systematically increases from SQ1 to SQ3, confirming the thesis of flux trapped in this structure.

The reason for the observed suppression of B_c is not completely understood. Since the comb-like structure significantly differs

from the strip line geometry assumed by theory, we expect the discrepancy to the theoretical prediction to be related to the concentration of magnetic flux into the slits, caused by Meissner shielding currents flowing most notably at the outer edge of the superconducting structure. The associated local enhancement of the magnetic field strength might significantly decrease the energy barrier for flux entry.

The author likes to thank his supervisor Prof. Paul Seidel.

References

- [1] Schönau T, Schmelz M, Zakosarenko V, Stolz R, Meyer M, Anders S, Fritsch L and Meyer H-G 2013 SQUID-based setup for the absolute measurement of the Earth's magnetic field *Supercond. Sci. Technol.* **26** 35013.
- [2] Schönau T, Zakosarenko V, Schmelz M, Stolz R, Anders S, Linzen S, Meyer M and Meyer H-G 2015 A three-axis SQUID-based absolute vector magnetometer *Rev. Sci. Instrum.* **86** 105002.
- [3] Schönau T, Schmelz M, Zakosarenko V, Stolz R, Meyer M, Anders S, Linzen S, Fassbinder J W E and Meyer H-G 2016 Absolute calibration of a three-axis SQUID-cascade vector magnetometer *Meas. Sci. Technol.*
- [4] Caputo P, Oppenländer J, Häussler C, Tomes J, Friesch A, Träuble T and Schopohl N 2004 High-performance magnetic field sensor based on superconducting quantum interference filters *Appl. Phys. Lett.* **85** 1389.
- [5] Caputo P, Tomes J, Oppenlander J, Haussler C, Friesch A, Trauble T and Schopohl N 2005 Superconducting Quantum Interference Filters as Absolute Magnetic Field Sensors *IEEE Trans. Applied Supercond.* **15** 1044–7.
- [6] Kuit K, Kirtley J, van der Veur W, Molenaar C, Roesthuis F, Troeman A, Clem J, Hilgenkamp H, Rogalla H and Flokstra J 2008 Vortex trapping and expulsion in thin-film YBCO strips *Phys. Rev. B* **77** 134504.
- [7] Pearl J 1966 Structure of Superconductive Vortices near a Metal-Air Interface *J. Appl. Phys.* **37** 4139.

Single artificial atom lasing by a dressed flux qubit

G. Oelsner¹, U. Hübner¹, E. Il'ichev¹, and P. Seidel

¹Leibniz Institute of Photonic Technology, Jena, Germany

Since the first demonstration of lasing in the optical domain in 1960 [1], laser physics has become an important direction in science. Today lasers are widely used for applications. Still, it was not before 2003 that lasing was demonstrated with only a single atom [2]. The reason is that many technical achievements were necessary to achieve the strong atom-photon interaction. This includes trapping of single atoms, their laser cooling, and the development of the field of quantum electrodynamics.

On the other hand, in rather new studies of macroscopic solid state quantum systems arbitrary coupling strengths can be realized [3] and high quality cavities are available [4]. Thus, lasing with a single artificial atom has been demonstrated on such a superconducting system, namely a three level charge qubit [5].

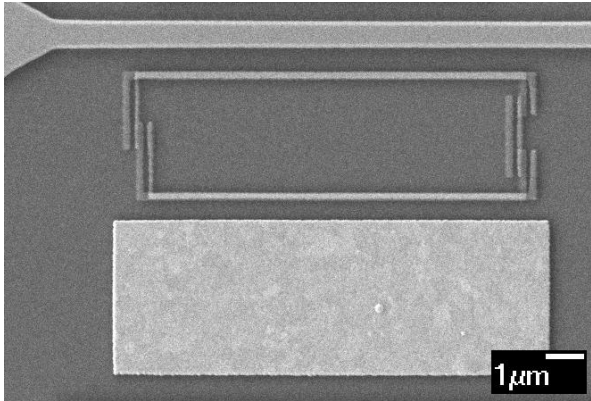


Fig.1: SEM picture of the artificial atom. It consists of a $10 \times 3.5 \mu\text{m}^2$ qubit loop interrupted by three Josephson junctions. The qubit is fabricated by shadow evaporation technique. A gold film plate is evaporated next to the qubit (lower light area) to enhance the relaxation rate of the two-level system. The whole structure is placed at the current antinode of a coplanar waveguide resonator. Its central conduction line is visible at the top of the picture.

Here we report on a new lasing scheme that requires only two levels of a superconducting flux qubit placed inside of a coplanar waveguide resonator. An SEM picture of the central part of the used sample is shown in Fig.1.

First we carried out an experimental characterization of the device by transmission measurements as in [3]. We found a resonator fundamental mode frequency $\omega_0/2\pi$ of about 2.5 GHz and a quality factor of 50000. The qubit has a minimal level splitting of 3.5 GHz and a persistent current of 12 nA. With the geometry the latter results in a qubit-resonator coupling of $g = 1.6$ MHz.

To achieve lasing a strong microwave signal is applied at the resonators third harmonic. Therewith the qubit states get dressed as sketched in Fig. 2.

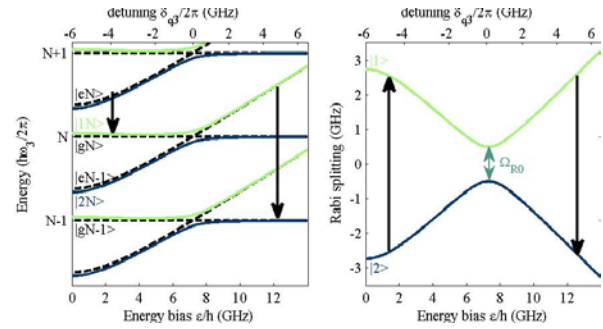


Fig.2: Dressed level structure over externally control parameter ε of the qubit energy. On the left picture the dressed levels around the mean photon number N are shown. The relaxation indicated by the black arrows always brings the qubit from the excited to the ground state, without changing the photon number. An additional splitting, with frequency of the on resonant Rabi frequency is observed at the interaction point (here around $\varepsilon = 7$ GHz). For a high mean number of photons this degree of freedom can be traced out and an effective two-level system (right), where the relaxation or excitation can be controlled externally, is achieved.

The effect of the driving signal can then be included in a change of the basis to the dressed frame. The states on one step of the dressed ladder (always one pair of green and blue states in Fig. 2) are formed by a superposition of the states $|gN\rangle$ and $|eN-1\rangle$ and their splitting is given by the Rabi frequency

$$\Omega_R = \sqrt{\delta^2 + \Omega^2},$$

were δ is the detuning between qubit and driving signal and Ω the on resonance splitting. The latter depends on the driving photon number.

Note, the relaxation from the excited to the ground state of the qubit, indicated by the black arrows in Fig. 2, points from the blue to the green state if the qubit splitting is smaller than the resonator frequency and vice versa in the other case. The latter corresponds to excitation in a dressed state pair. Directly in resonance the superposition is formed equally by ground and excited state, and the population is equalized on the dressed states.

For high photon numbers N the Rabi frequency only slightly depends on N , and this degree of freedom can be traced out. Then an effective two level system as sketched on the right in Fig. 2 is found. A working area is found where the relaxation of the qubit transfers the population to the higher energetic state. That is why a gold resistor is placed next to the qubit (see Fig. 1) to enlarge the relaxation of the qubit. In this way we achieve population inversion.

Still it needs to be clarified if this effective system couples to the photon field of another, e.g. the fundamental, mode. This indeed is not the case for an optical system because the dipole moment of an atom has no transition element between these dressed states.

On the other hand, a flux qubit additional has a longitudinal coupling that allows an interaction between resonator and dressed states. Details of the calculation for effective dissipative rates and the transition elements is presented in [6,7]. The effective coupling scales proportional to Ω/Ω_R , and thus is maximal at resonance and decreases with increasing detuning δ . Note, this also means that the on resonance splitting $\Omega \sim g\sqrt{N}$ and thus the coupling constant g has to be large for reasonable coupling to the dressed states.

For the experimental demonstration of the lasing effect the emission from the resonator is measured with a spectrum analyzer. The measurement is carried out as follows. A trace of data points is always taken in consequence with driving signal on and off to avoid effects of very low frequency drifts and heating. The measurement bandwidth and

number of data points is chosen such that one trace takes less than one second. The data is then collected over 40000 averages which correspond to a 12 h measurement. The results at one working point are shown in Fig. 3.

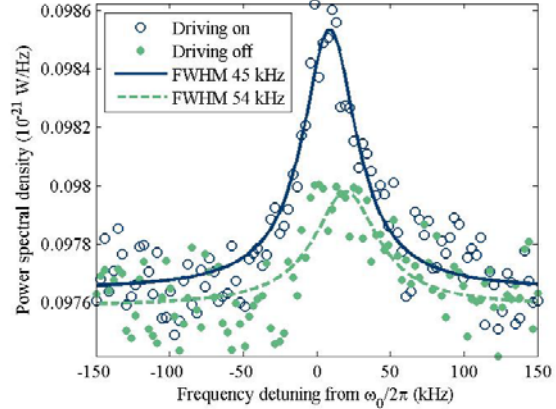


Fig.3: Emission from the qubit-resonator system. The green dots show the power spectral density of the thermally excited resonator at 30 mK. After the lasing process is switched on (blue circles) the emission is increased and the linewidth narrowed. For extracting the linewidths Lorentzian fit (solid lines) are used. Note, the noise background corresponds to the one of the cold amplifier placed at 4 K plate and can be calculated to a noise temperature of about 7 K.

The results without the lasing process turned on reveal the thermal response of the resonator – a Lorentzian line shape with the width of the resonators lossrate and a power spectral density corresponding to a thermally excited resonator at 30 mK. With the driving turned on the output is increased to more than twice and the linewidth narrows about 20 %. This demonstrates the stimulated emission of the dressed qubit into the resonator.

In conclusion, a new lasing concept that involves only two levels of an artificial atom was developed and experimentally investigated. A full characterization and theoretical discussion of the dynamics of the dressed qubit-resonator system can be found in Ref. [7].

References

- [1] T. H. Maiman Nature **187**, 493 (1960)
- [2] J. McKeever, et al. Nature **425**, 268 (2003)
- [3] G. Oelsner, et al. Phys. Rev. B **81**, 172505 (R) (2010)
- [4] P. Macha, et al. Appl. Phys. Lett. **96**, 062503 (2010)
- [5] O. Astafiev, et al. Nature, **449**, 588 (2007)
- [6] G. Oelsner, et al. Phys. Rev. Lett. **110**, 053602 (2013)
- [7] G. Oelsner, Doctoral thesis, FSU Jena, 2016.

Verifiable quantum superpositions in superconducting interconnects

Elena Zhitlukhina¹, Mikhail Belogolovskii², and Paul Seidel

¹ *Donetsk Institute for Physics and Engineering, 03028, Kyiv, Ukraine*

² *Institute for Metal Physics, 03142, Kyiv, Ukraine*

In a large quantum system, spatially separated nodes storing quantum information in qubits and processing it locally using quantum gates may interact and communicate across a network [1]. For the network, it would be beneficial to support transmissions of entangled qubits. Indeed, quantum connectivity allows to increase a state space of dimension $k2^n$ for k nodes, each with n qubits, linked by classical channels to an exponentially larger state space, 2^{kn} in the case of a fully quantum network. Moreover, it also provides a potentially powerful means to overcome size-scaling and error-correlation problems that would limit the size of quantum processing engines [1] and enhance the information transportation [2]. The first protocol able to realize ideal quantum transmission [3] was tailored to a potential network implementation in which trapped atoms or ions constitute the storage and processing nodes whereas photon transmission lines provide communication channels. Optical networks have the advantage of being able to use existing telecommunication fibers or even to transmit quantum information through the atmosphere or a vacuum. While at the moment photons seem to represent the best qubit carrier for fast and reliable communication over long distances, solid-state technologies have better prospects for scalability and could provide more ingenious ways to link a lot of qubits and quantum gates needed for almost all significant applications [4].

Electron quantum optics is a novel paradigm aimed to realize the charge transport in solid-state ballistic conductors by implementing ideas and methods of quantum optics [5]. It has inspired a search of novel, innovative means for transmitting electrons as information carriers across quantum networks. From the materials viewpoint, the best solution would be superconductors (S) where quantum effects are macroscopic. Further progress in this field is intimately linked to the development of new roads to characterize the quantum-system capacity for information processing. In quantum optics, it can be done with interferometers which split and recombine wave packets and thus provide a way to probe the superposition principle. In this contribution, we discuss a similar solid-state test of the coherent maintenance in S interconnects using a simplest device, a hybrid fork with two S terminals and a normal (N) counter-electrode coupled to them (see the inset in Fig. 1).

When the distance between the two NS connections d is less than the phase decoherence length L_Φ , charge states in the three leads are entangled. The fully quantum treatment requires the continuity of the wave function and the probability flux conservation at the contact point. In the normal state, we find transmission and reflection probability amplitudes $t_{12(13)} = 2\sqrt{k_1 k_{2(3)}} / (k_1 + k_2 + k_3 + iK)$ and $r_{11} = (k_1 - k_2 - k_3 - iK) / (k_1 + k_2 + k_3 + iK)$ for three free-electron states with wave

numbers k_i ($i=1,2,3$) and the effective scattering characteristic K at the node (in a two-terminal case, it is an interface potential-barrier strength). The most important conclusion is that the backscattering in the three-arm structure takes place even without any scattering at the node ($K=0$) and for identical leads ($k_1=k_2=k_3$) and thus the current through the system can be strongly modified comparing to the ‘trivial’ case of d exceeding L_ϕ when the total transmission probability is a sum of partial contributions. To reveal this difference, two terminals should be transferred into the S state and the Andreev transformation of an electron (hole) approaching the NS interface into a hole (electron) going back to the node should be taking into account. These backscattering processes create a superposition of quantum states from the two S leads exhibiting itself in a non-trivial conductance spectra $G(V) = dI(V)/dV$ that depends also on the measurement configuration. The main panel in Fig. 1 illustrates the difference between fully quantum and ‘trivial’ approaches when the voltage biasing is applied to N and both S leads.

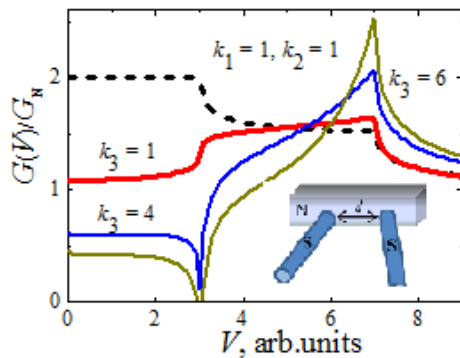


Fig. 1: Normalized conductance spectra (solid lines) of a contact shown in the inset. Energy gaps of the S leads are 3 and 7 arb. units, the wave numbers k_i are shown in the figure, $K = 0$. The dashed line demonstrates a ‘trivial’ $G(V)/G_N$ curve for $k_1=k_2=k_3=1$ and $K = 0$.

Let us mention some other results. The effect shown in Fig. 1 for $K=0$ is more pronounced when the difference between the two gaps is smaller. If the scattering effect at the node is nonzero ($K \neq 0$) the conductance spectra is more like a ‘trivial’ result for two parallel tunneling junctions with the only but significant difference, namely, in the first case we have independent weighting factors while in the consistent quantum theory the only fitting parameter K determines the shape of the $G(V)$ dependence. Introduction of a decoherence amount at the device node restores the ‘trivial’ results.

Resuming, our results pave the way towards experiments establishing the presence and amount of quantum entanglement in superconducting interconnects as well as an estimation of the phase decoherence length in quantum networks. The existing theoretical interpretation of the charge transport across hybrid N-S structures has been merely based on the diffusive limit relevant to most experimental samples. Recent progress in the fabrication of ultra-thin metallic lines with favorable characteristics permits to focus the analysis on the ballistic limit employing the notion of semiclassical electron trajectories and treating thus the problem exactly and comprehensibly.

References

- [1] H.J. Kimble, Nature **453**, 1023-1030 (2008).
- [2] P. Arrighi *et al.*, Phys. Rev. A **95**, 012331 (2017).
- [3] J.I. Cirac *et al.*, Phys. Rev. Lett. **78**, 3221-3224 (1997).
- [4] M. Stoneham, Physics **2**, 34 (2009).
- [5] B. Roussel *et al.*, to be published, DOI: 10.1002/pssb.201600621, and related papers in the upcoming Special issue of Phys. Status Solidi B on Single-Electron Control in Solid-State Devices (2017).

Induction measurements at the Lambda point

Ralf Neubert, Jessica Golm, Volker Tympel

The current versions of *cryogenic current comparators (CCC)* as non-destructive, highly-sensitive charged particle beam monitoring devices are using flux concentrator rings to capture the magnetic field of the particles at an operating temperature of 4 K [1]. In some facilities beam line and storage ring will be cooled down to 2 K, so the CCC should operate at this temperature, too. This fact requires the determination of the core material down to the Helium Lambda point and below [Fig. 1].

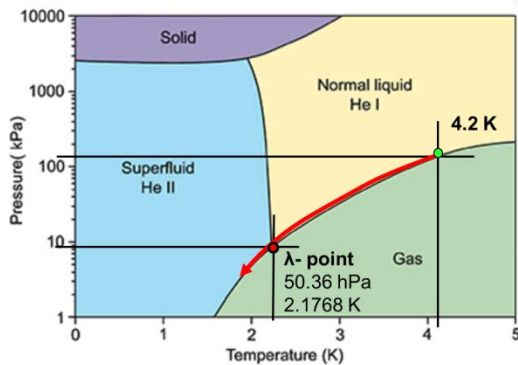
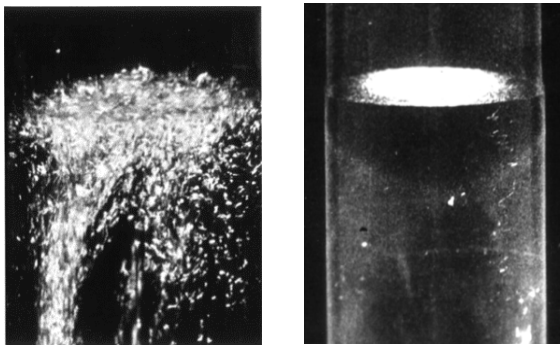


Fig. 1: Phase diagram of ^4He , after [2].

At this point (~ 2.17 K) normal fluid helium makes the transition to superfluid helium II, bulk boiling [Fig. 2a] ends caused by extremely high thermal conduction [Fig. 2b].



a
b
Fig. 2a: bowling of ^4He I at > 2.17 K,
Fig. 2b: superfluid ^4He II at < 2.17 K [3].

The specific heat capacity of helium goes to infinity as the temperature approaches the λ -point [Fig. 3].

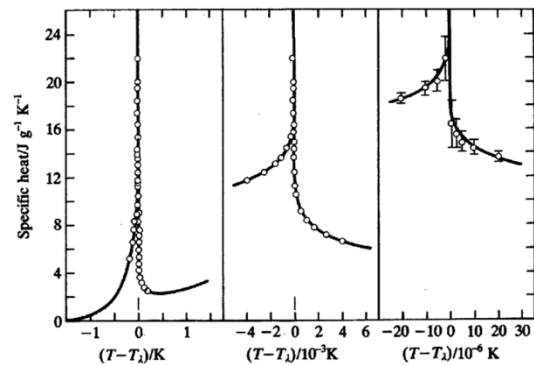


Fig. 3: Specific heat at the Lambda point [4].

To achieve this temperature we used a stainless steel wide neck cryostat, a gas flow control unit and two scroll pumps SC15D with a suction of $15 \text{ m}^3 / \text{h}$ each. The complete system is shown in Fig. 4.

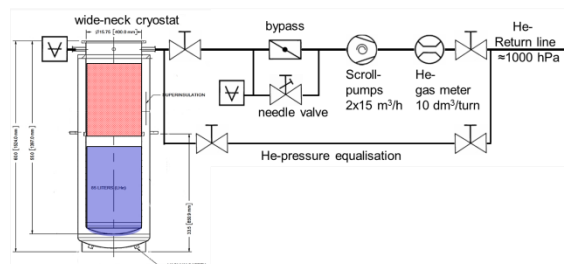


Fig. 4: Experimental setup

The temperature down to 1.4 K was measured by a calibrated Lakeshore CX-1050-SD-1.4L sensor and a Lakeshore 336 temperature controller, the pressure by a gas type independent vacuum meter (Ilmvac PIZA 110) and the gas flow rate by a gas meter. The gas flow rate was adjusted manually to a constant value of 50 l / min.

After a pumping time of 5 hours 35 minutes we reached the λ -point [Fig. 5].

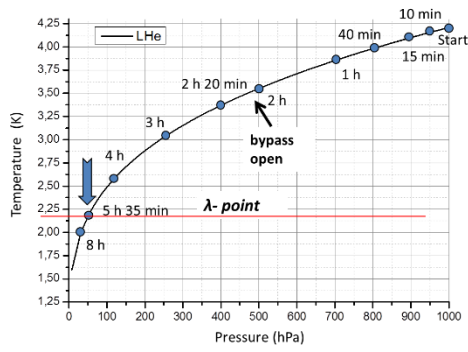


Fig. 5: Temperature-pressure diagram as a function of pump time, basing on data from MacCarty [5].

Caused by the sharp rising thermal capacity of helium at the λ -point the helium bath temperature is roughly constant for a longer time, see the flat area in Fig. 6.

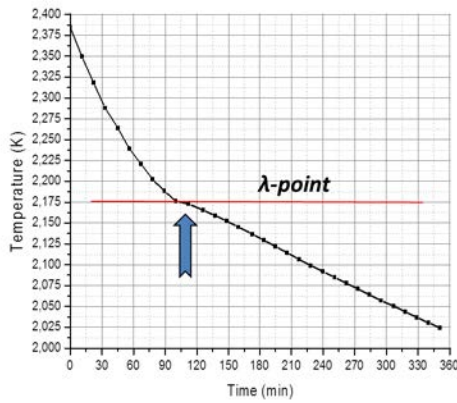


Fig. 6: relative pump time (just one scroll pump used) within the range of the λ -point.

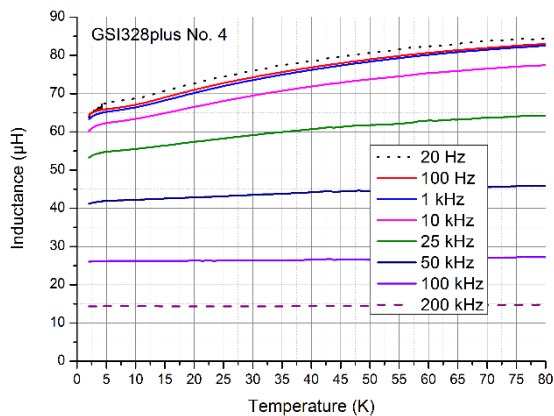


Fig. 7: Measurement of the one-turn inductance between 2 K and 80 K.

The core permeability is frequency- and temperature-dependent, the permeability loss increases slightly at temperatures below

5 K and frequencies below approximate 50 kHz compared to higher temperatures [Fig. 7].

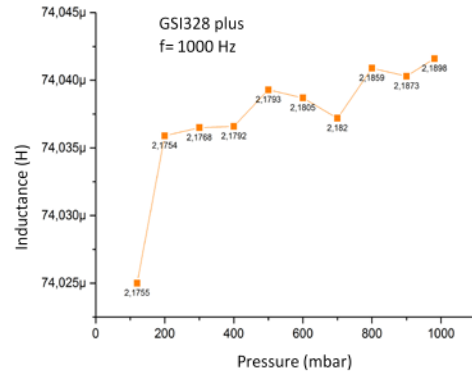


Fig. 8: Pressure independence of the inductance at 2.175 K and for $f = 1000$ Hz

Former measurements showed a pressure sensitivity of the CCC signal. To investigate this, the inductance of the core at a fixed temperature for different pressures (100 - 1000 mbar) was measured. The measurements showed that the core inductance is pressure independent [Fig. 8].

Now we are able to characterise large flux concentrators at and below the λ -point.

This research is supported by the BMBF (project# 05P15JRBA) and the CERN project collaboration agreement number KE2915/BE.

References

- [1] M. Fernandez *et al*, Non-perturbative measurement of low-intensity charged particle beams, Superconductor Science and Technology (2016)
- [2] www.superfluid.cz/?lang=en&page=intro
- [3] A. Leitner - Liquid Helium II the Superfluid, movie 1963, www.youtube.com/watch?v=sKOlFR5OcB4
- [4] M. J. Buckingham, W. M. Fairbank, The nature of the λ -transition in liquid helium, Progress in Low Temperature Physics, Vol. 3, pp. 80–112 (1961)
- [5] R. D. McCarty, Thermodynamic Properties of Helium-4 from 2 to 1500 K at Pressures to 10^8 Pa, J. Phys. Chem. Ref. Data, Vol. 2, No. 4 (1973)

Precision induction measurements of flux concentrators

Volker Tympel, Ralf Neubert, Jessica Golm

The current versions of *cryogenic current comparators (CCC)* as non-destructive, highly-sensitive charge particle properties beam monitoring devices are using flux concentrator rings to capture the magnetic field of the moving particles [Fig. 1]. The new FAIR accelerator facility at GSI Darmstadt requires extended versions of CCCs with larger diameters called CCC-XD [1].

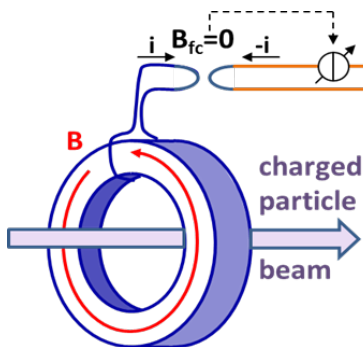


Fig. 1: The general principle of a CCC with a flux concentrator and a closed loop current measurement system [2].

The required new flux concentrator is a specially designed highly-permeable core made of nano-crystalline material with an inner core diameter greater than 270 mm. Figure 2 shows the complete core package consisting of three single ribbon cores [Fig. 3a]. As shown in Fig. 3b the single cores are made of approximately 1500 thin layers of special tempered NANOPERM®.



Fig. 2: Core package GSI328plus with an outer diameter of 300 mm and a depth of 100 mm.

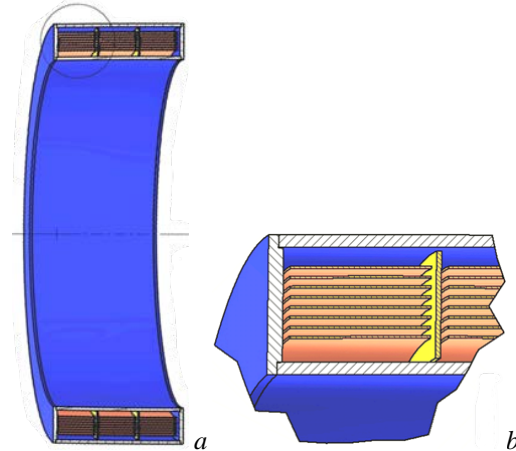


Fig. 3a: Virtual cut through the core package.

Fig. 3b: Enlarged cut through a NANOPERM® ribbon core (only schematic: real ribbon thickness $\approx 15 \mu\text{m}$) [2].

For the core package characterisation a high-precision L_S - R_S -measurement setup based on an Agilent E4980A LCR-meter for the measurement of the series inductance L_S and the series resistance R_S , a LabVIEW script to control the hardware, a C++ programme for the data analysis and a wide-neck cryostat were developed. Two scroll pumps (SC 15D) allow a temperature range from 300 K down to below 2 K. Due to thermomagnetic annealing process of the amorphous basic material (recipe) a variation of the electrical parameter is possible.

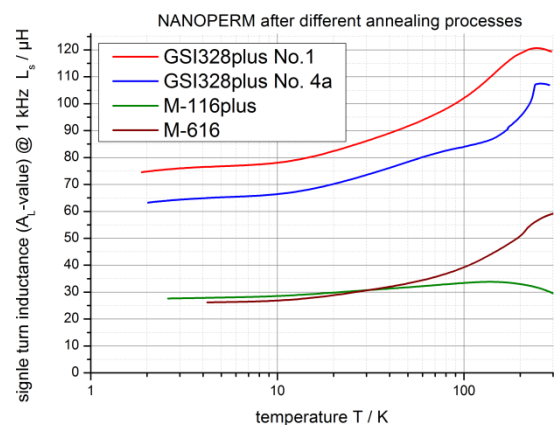


Fig. 4: Different recipes of the thermo-magnetic annealing process lead to changed characteristics [2].

Figure 4 shows that different recipes lead to different electro-magnetic properties. Also the same shape but different batches (samples GSI328plus No.1 / No.4a) can lead to different characteristics. As shown in Fig. 5 the variation between samples of the same batch is very small.

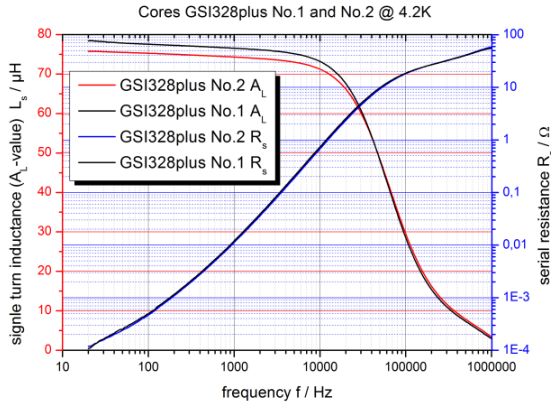


Fig. 5: Two core package of GSI328plus from the same core batch [2].

The temperature dependence of the inductance of the GSI328plus cores is about 0.35 $\mu\text{T/K}$ or 0.46 %/K at 4.2 K [Fig. 6].

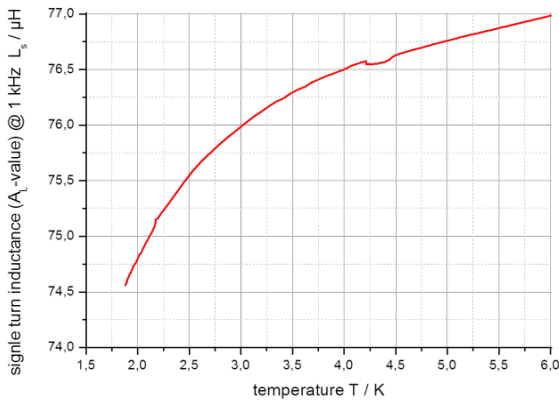


Fig. 6: Inductance of GSI328plus No.1 between 2 K and 6 K.

The ferromagnetic core material can be described by a complex permeability $\mu = \mu' - i\mu''$. The real μ' [Fig. 7] is proportional to L_s and the imaginary part μ'' [Fig. 8] is proportional to R_s/f with f as the measured frequency. The complex permeability μ is in fact a function $\mu(f, T)$ with the frequency f and the temperature T .

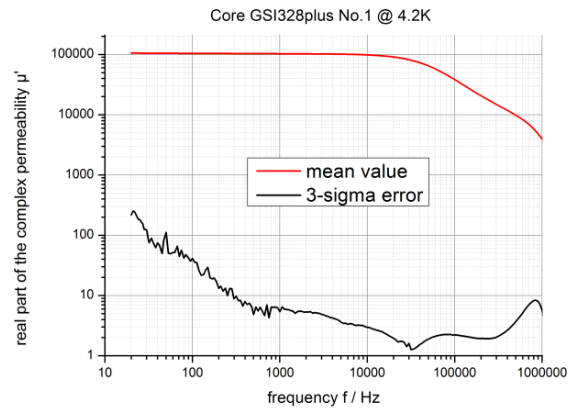


Fig. 7: Precision measurement of the real part μ' [2].

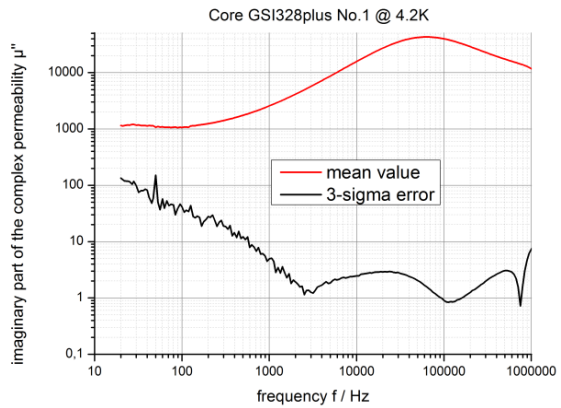


Fig. 8: Precision measurement of the imaginary μ'' [2].

Now we are able to characterise large flux concentrators down to 2 K. This research is supported by the BMBF (project# 05P15SJRBA) and the CERN project collaboration agreement number KE2915/BE.

References

- [1] M. Schwickert et al., Status of beam current transformer developments for FAIR. Proceedings of IBIC2016, Barcelona, Spain - Pre-Release Snapshot 06-Oct-2016 08:00 TUPG50
- [2] V. Tympel et al., The next generation of cryogenic current comparators for beam monitoring. Proceedings of IBIC2016, Barcelona, Spain - Pre-Release Snapshot 06-Oct-2016 08:00 TUPG43

Development of an applicable test facility for lowest permeation values and investigation of samples, which are suitable for the non-magnetic cryostats

Matthias Thürk, Stefan Bräuer*, Hannes Nowak*, and Paul Seidel

* Supracon AG, An der Lehmgrube 11, 07751 Jena

This research and development project was carried out in cooperation with Supracon AG (Jena) and with the Institut für Konstruktion und Verbundbauweisen (KVB) gemeinnützige GmbH (Döbeln). The aim is to achieve novel composite materials and manufacturing technologies for cryostats applicable in seaborne and airborne resource research as well as environmental research.

Nowadays resource exploration is proving to be difficult. Therefore, sensitive magnetometer devices as SQUID-based magnetometers, could make a substantial contribution in this field, provided that the device can be used airborne or submarine. It means the helium cryostat required for the SQUIDs has a sufficient long operation time. In this matter, the weakest point in the dewar is the material for the neck, i.e. the connection between 4.2K and 300K. To reduce the helium penetration rate of the neck material, the co-operation partner (company KVB) developed different strategies to manufacture fiberglass materials with extremely low helium permeation rate, i.e. with lower helium permeation rate instead of commercial ones.

The permeation of gas through glass depends on the porosity of the microstructure and the properties of the gas molecule. The helium atom, with its small diameter, has the highest permeation rate through glass of any of the gases [1]. The rate of gas permeation through glass with a wall thickness d and area A is given by

$$Q_i = K \times (A/d) \times (P_2 - P_1)$$

where P_1 and P_2 are the gas pressure on each side of the wall and K is the permeation constant of the material of question, with units of m^2/s . For thin-walled fiberglass tubes, the diffusion constant should be roughly $10^{-15} m^2/s$ at 300K [1]. Unfortunately such a quality is by far not available on the open market, which we found instead as the best quality with a Korean product shown in Fig. 4 No.1, which diffusion constant of $9 \times 10^{-14} m^2/s$ corresponds to a much lower diffusion-tightness than necessary.

We investigated the mechanism of the permeation in detail. Based on this study, we developed and built up a test set-up (figure 1 and 2) for measuring the standard helium leak rate which provides the permeation rate.

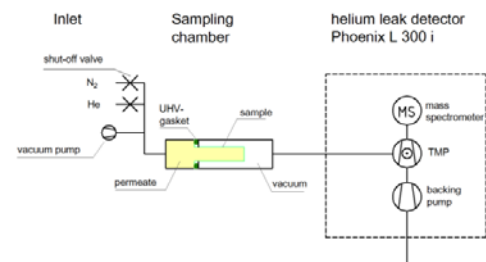


Fig. 1: Schematic of the set-up.

Two adapted sampling chambers (figure 3), which were fitting with the setup described above, were developed and manufactured.



Fig. 2: Measurement equipment

- 1 – helium gas, pressure cylinder
- 2 – turbo-pumping station
- 3–sampling chamber1, $\varnothing= 30\text{mm}$
- 4- helium leak detector (connected to LabVIEW)
- 5 – sampling chamber 2, $\varnothing= 45\text{mm}$

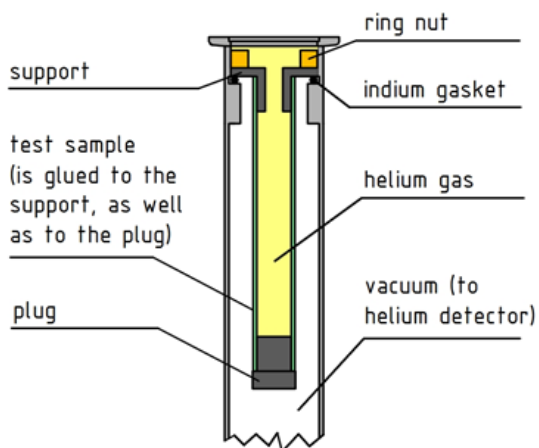


Fig. 3: Scheme of the sample chamber.

101 samples have been measured with a measurement time of 8540 hours. With calibration-measurements and occasional testing of alternative materials about 9700 hours total measurement time were performed with this experimental set up. Due to a strong interaction between IFK and the co-operation partner KVB the permeation measurement data were exchanged on a day-to-day basis. Therefore, KVB got the feedback whether

the applied technology was going in the right direction or if it had failed.

Additionally, in respect to a usable product, permeation rate measurements were performed before and after

- a typical thermal cycling between 300K and 77K up to 5 times as well as
- applying alternating stress within the stiffness range.

Figure 4 shows the permeation versus time of 4 different samples, in which sample 1 is the best available on the open market, sample 2 the best achieved within this project, and sample 3 best quality from No. 2 with mechanical stabilization.

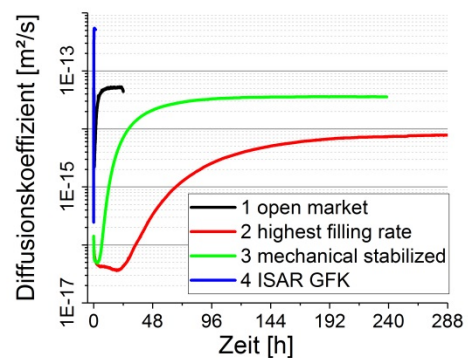


Fig. 4: Q_i versus time characteristics measured for different samples with the described setup (figures 1 to 3).

We achieved the best value with a diffusion constant of $6.6 \times 10^{-15} \text{ m}^2/\text{s}$ with sample 2. With this material we were able to demonstrate a helium cryostat with a lifetime of 370 days which meets the aim of the referred project.

This work was supported by the ZIM / BMWi grant No. KF2311616DF4.

References

- [1] J. W. Ekin “Experimental Techniques for Low-Temperature Measurements” Oxford University Press (2011).

Developing processes and devices for abrasive blasting with cryogenic water ice

S. Oehler, L. Föllmer, H. Nowak*, M. Thürk

* Jenpneumatik & Schlauchtechnik GmbH, 07745 Jena, Germany

This research and development project is a cooperation with *RS Korrosionsschutz GmbH* and *Jenpneumatik & Schlauchtechnik GmbH*. The aim of the project is to develop an ecological substitute for abrasive sandblasting and needle scaling using cryogenic water ice particles.



Fig. 1: Cryogenic water ice particles with different diameters (left: 1.3 mm; right: 3.5 mm)

Our part is to develop the process parameters of the blasting abrasives and the blowing agent. The abrasiveness of the particles primary depends on their hardness and toughness. According to hints from literature the stiffness of water ice can be increased by lowering the temperature down to cryogenic values [1]. On the other hand, we try to reduce the necessary force to remove the thin coating layer. With a cryogenic blowing agent (e.g. LN2) we can take advantage of the embrittlement of the coating and the different thermal expansion coefficient between the coating and the material to be blast.

Therefore, we generate and test water ice particles with different diameter around 0.5 to 4.0 mm. Examples are shown in Fig. 1. First investigations with the

crushing test (as shown in Fig. 2) were carried out at different particle diameters at LN2 temperature (77° K). The results in Fig 3 with breaking force F_b per volume V at different particle diameter d shows an increasing of the breaking force per particle volume with smaller particles.

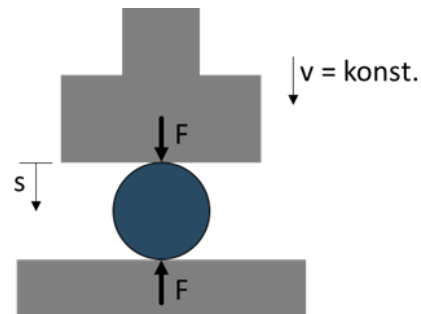


Fig. 2: Schematic setup of the crushing test.

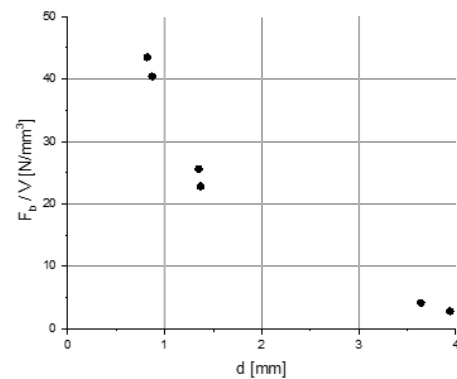


Fig. 3: Breaking force per volume at different particle diameters d

The reason could be a lower defect rate of the ice particles with smaller diameters. This means the smaller particles have a lower density of crystallographic defects which can perform as crack starting points in the ice. The lack of defects in the water crystal is a great issue for a high stiffness.

We'll create the ice not just from normal water. Therefore, we intend to investigate different types of refined water (i.e. deionized water) to study the influence on the breaking force at same particle diameters. The installation of a relevant experimental set up is under way.

To decrease the necessary force to remove the thin coating layer we benefit from thermal stress between the coating layer and the base material. This results from a different thermal expansion coefficient of both materials. To determine the amount of this effect we will investigate the thermal expansion coefficient of these materials with the following interferometer measurement setup shown in Fig. 4, which is a part of the setup from a master thesis [2]. The probe has two mirrors on both sides of the cavity to serve as an optical resonator.

This project is supported by AiF/BMWi ZIM under No. ZF4210702DF6

References

- [1] M. Petzel, Tieftemperatur-Wassereis-Strahlen, Shaker Verlag Aachen (2014).
- [2] F. Rietschel, Temperaturabhängigkeit der Brechzahl von Silizium, Masterthesis, (2017) in preparation.

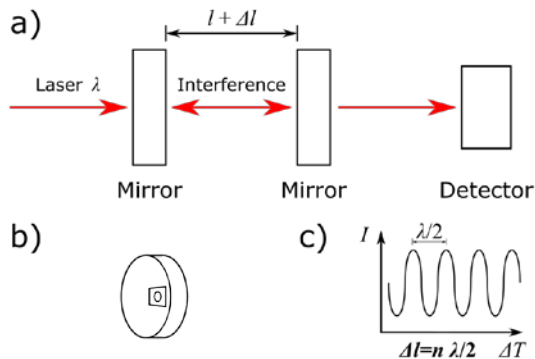


Fig. 4: a) Schematic measurement setup for expansion coefficient b) sample with mirrors on both sides of the cavity c) schematic measurement signal at the detector

This self-made dilatometer set-up is embedded in a helium-gas flow cryostat that provides variable measurement-temperatures down to 10 K. Temperature control is accomplished by an automatic temperature controller using silicon diodes as temperature sensors.

Comparative analysis of current transport on small angle grain boundaries on thin YBCO films using x-ray microscopy and magneto-optical imaging

Stephen Ruoff^{1,2}, Claudia Stahl¹, Gisela Schütz¹, Joachim Albrecht³

¹ Max-Planck-Institute for Intelligent Systems, Heisenbergstr.1, D-70569 Stuttgart;

² Friedrich-Schiller-University Jena, Institut für Festkörperphysik, Helmholtzweg 5, D-07743 Jena;

³ Research Institute for Innovative Surfaces FINO, Aalen University, Beethovenstr.1, D-73430 Aalen;

Current transport in high-temperature superconductors is strongly affected by the presence of grain boundaries [1]. Thin superconducting $\text{YBa}_2\text{Cu}_3\text{O}_{7-\delta}$ films are prepared on bicrystalline substrates containing a symmetric small-angle tilt grain boundary with a misorientation angle of 5° . The suppression of the supercurrent at these grain boundaries has to be avoided for the application of superconducting materials in current transport applications [2]. Therefore a detailed understanding of the current flow across such grain boundaries is very important. The current carrying capabilities across a small-angle grain boundary can be imaged using Magneto-optical imaging as well as the novel method of x-ray microscopy using the XMCD (X-ray Magnetic Circular Dichroism) effect. More details about XMCD-microscopy on high temperature superconductors can be found in [3-7]. The used YBCO sample has a film thickness of 275 nm and is epitaxially grown on bicrystalline SrTiO_3 substrates by pulsed laser deposition. Chemical etching has been used to create square-shaped films of 1 mm width that are oriented under different angles to the grain boundary, respectively. In a first step magneto-optical imaging has been used to image the trapping of magnetic flux penetration inside the grain boundary. Figure 1 shows on the left side a sketch of the sample

square and on the right side the corresponding magneto-optical image. This image was taken while the sample was in the remanent state at 12K.

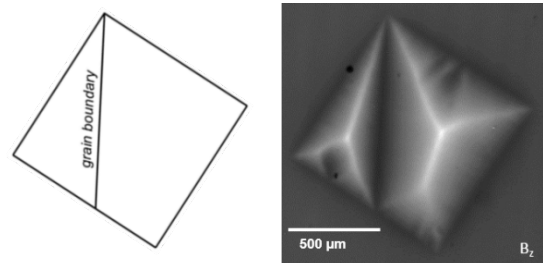


Fig. 1: Left: Sketch of the sample square with the grain boundary. Right: Magneto-optical image of the remanent state of this square.

A numerical analysis of the image in Fig. 1 allows the determination of the spatially resolved current density pattern and the in-plane components of the magnetic flux density [8]. The left part of fig. 2 shows the in-plane component of the magnetic flux distribution along the x-direction. The right image in fig. 2 shows the corresponding

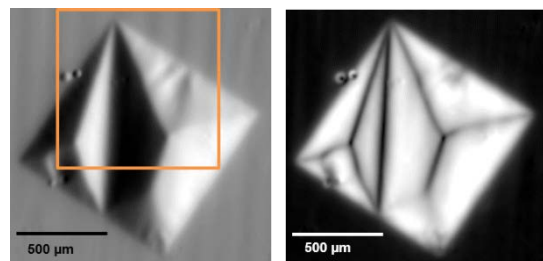


Fig. 2: Left: Numerically calculated in-plane component of the flux distribution. Right: Calculated critical current density distribution. The orange square marks the section depicted in Fig.3.

critical current distribution of the sample in the remanent state.

A transfer of the magneto-optical technique to the soft x-ray regime promises measurements with higher spatial resolution. However, in this case a sensor layer is needed which exhibits a strong XMCD effect. Therefore we use an amorphous CoFeB layer which is deposited on top of the YBCO using ion beam sputtering at room temperature. The XMCD signal of either iron or cobalt is quantitatively related to the in-plane flux density component of the superconductor [3]. The sample has been prepared in the same way as the sample for the magneto-optical measurements. The films are now measured in the x-ray microscope MAXYMUS at the synchrotron BESSY II at HZB, Berlin at room temperature. Fig. 3 shows the magnetic contrast obtained using x-ray microscopy.

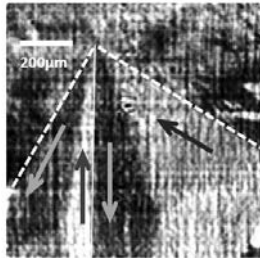


Fig. 3: X-ray microscopy image of the marked area of Fig.2. The white dotted line marks the edge of the film. Arrows mark the local current pathway. The gray scale represent the local magnetization. A solid white line marks the grain boundary.

For clarification the current pathway has been marked with arrows in the image of Fig. 3. This image can be directly compared to the left image of Fig. 2 which represents the in-plane magnetization of the superconducting sample. This shows the capabilities of this novel method of imaging the magnetic flux distribution using x-ray microscopy. In this first image

of a current limiting grain boundary within an YBCO sample is imaged successfully. This opens up the opportunity to image superconducting micro- and nanostructures with high spatial resolution using x-rays. This work is published in IEEE Transactions on Applied Superconductivity [9].

Acknowledgment

The author appreciates helpful discussions with his supervisor Prof. Paul Seidel.

References

- [1] H. Hilgenkamp *et al.*, *Rev. Mod. Phys.* **74**, 485-549, (2002).
- [2] D. Larbalestier *et al.*, *Nat.* **6861**, 368-377, (2001).
- [3] S. Ruoß *et al.*, *Appl. Phys. Lett.* **106**, 022601 (2015).
- [4] C. Stahl *et al.*, *Phys. Rev. B.* **90**, 104515 (2014).
- [5] C. Stahl *et al.*, *AIP Proceedings* **1696**, 020031 (2016).
- [6] C. Stahl *et al.*, *J. Appl. Phys.* **117**, 17D109 (2015).
- [7] S. Ruoß *et al.*, *New J. Phys.* **18**, 103044 (2016).
- [8] C. Jooss *et al.*, *Reports Prog. Phys.* **65**, 651-788 (2002).
- [9] S. Ruoß *et al.*, *IEEE Trans. Appl. Supercond.* **26**, 1-6 (2016).